Continuous and Reversible Modulation of Interfacial Electrochemical Phenomena on Back-Gated Two Dimensional Semiconductors

A Dissertation
SUBMITTED TO THE FACULTY OF
UNIVERSITY OF MINNESOTA
BY

Chang-Hyun Kim

IN PARTIAL FULFILLMENT OF THE REQUIREMENTS
FOR THE DEGREE OF
DOCTOR OF PHILOSOPHY

C. Daniel Frisbie, Advisor

August, 2017

Acknowledgements

This dissertation could not have been completed without support and help of many people. First and foremost, I would like to thank my advisor, Professor C. Daniel Frisbie, for giving me the opportunity to study this excellent research topic in his group. I still remember the moment that I first met him and decided to join his group, impressed by his intelligence, insight, and passion about his research field. He is the greatest mentor in my life, who helped me overcome all obstacles and challenges that I faced during the degree program. Whenever I lost direction and motivation to pursue the research due to disappointing results, he encouraged me to take a step forward with invaluable advice and waited with patience until I overcame the difficulties. What I have learned from him about delivering ideas in effective and clear way in scientific manuscripts and presentations would be one of the most valuable assets in my life.

Also, I should thank all the people from the Frisbie and other research groups who directly or indirectly contributed to this dissertation. Prof. Bryan Paulson provided an initial idea about experimental setup and reviewed my dossier when I was preparing for the preliminary oral exam. Dr. Yoska Anugra, a former graduate student of the Koester group, taught me an essential experimental skill handling graphene. Prof. Keun Hyung Lee and Prof. Hongchul Moon gladly shared materials that they synthesized for my experiments. Dr. Seung Wook Shin, a former postdoc in the Aydil group, gave me a really valuable advice that helped me prepare and handle ultrathin ZnO films. I acknowledge Scott White's effort to set up the ambient probe station and his valuable advice about

microfluidic device fabrication and experiments. Last but not least, I really appreciate the help and support of Yan Wang. Since she joined our group and was assigned to this project, we have had invaluable scientific exchanges and interactions to develop our ideas into reality.

I would also like to thank the current and the past members of the Frisbie group: Dr. Wei Xie, Prof. Se Hyun Kim, Dr. Kihyun Hong, Dr. Zuoti Xie, Prof. Yonghyun Kim, Dr. Stuart Oram, Dr. Jaehong Choi, Dr. Yanfei Wu, Dr. Geoffrey Rojas, Dr. Christopher Smith, Dr. Abel Demissie, Dr. Davood Taherinia, Dr. Woo Jin Hyun, Dr. Ankit Mahajan, Dr. Tao He, Dr. Donghoon Song, Elliot Schmidt, Boxin Tang, Xinglong Ren, Motao Cao, Fazel Zare Bidoky, Krystopher Jochem, Jingjing Qin, and others, for their help and valuable discussions in the lab and the office. I acknowledge the kind and helpful staffs of the Minnesota Nanofabrication Center and the Characterization Facility at University of Minnesota for equipment training and their help with device fabrication and characterization. I also acknowledge the Amundson Professorship, the Doctoral Dissertation Fellowship, and the Industrial Partnership for Research in Interfacial Materials and Engineering (IPRIME) for financial assistance.

Dedication

This dissertation is dedicated first and foremost to my beloved wife, Yoon Jung Ko, for always being there for me and for making me feel happy. Her love, encouragement, and wholehearted support made this achievement possible. I also dedicate this to my parents, Ki Gwang Kim and Young Ae Lee, for their love, patience, and for helping me believe in myself.

And finally, I dedicate this dissertation to my grandmother, Ye Sook Lee, with my greatest respect. She was the one who devoted her whole life to my family and taught me what true love is. She is the greatest inspiration in my life.

Abstract

The continuous increases in global population and energy consumption have raised major concerns about the security of our energy future. Limited amount of fossil fuels and increasing concerns over their combustion product, carbon dioxide, on climate change make renewable energy sources, such as sun light and wind, attractive options. Accordingly, energy conversion and storage devices based on (photo)electrochemical processes (e.g., batteries, fuel cells, water splitting, solar-to-fuel conversion, etc.) have received great attention as promising solutions to overcome the challenges in the intermittent renewable energy sources. To develop highly efficient and economically viable energy devices, fundamental understanding of electrochemical phenomena occurring at the electrode/electrolyte interfaces is essential. In this dissertation, we introduce a new approach, inspired by the operating mechanism of *field-effect transistors* (FETs), to modify and study such electrochemical interfaces.

The devices studied in this dissertation project have a "gate-insulator-electrode" stack structure, which is essentially similar to that of a FET but the (typically) thick semiconductor layer in regular FETs is replaced with an ultrathin or two-dimensional (2D) active electrode for electrochemical processes in our devices. In such a device, due to the extreme thinness of the active electrode, electronic properties at the electrode surface can be dramatically altered by extra charge carriers induced with a voltage bias to the *gate*. This, in turn, makes thermodynamics and kinetics of electrochemical processes at the

electrode/electrolyte interface be determined by the *gate bias* as well as by the electrode potential (with respect to the solution or reference electrode potential).

In this project, three interfacial electrochemical phenomena are of our main interest: (1) electric double layer charging, (2) electron transfer across interface, and (3) surface binding of reaction species on electrode surface. First, responses of electric double layer structure to the gate bias is investigated using graphene devices, and a method to experimentally separate the *band filling potential* and the *double layer charging potential* has been developed. Second, continuous and reversible modulation of outer-sphere electron transfer kinetics by a gate bias was demonstrated on ZnO devices for the first time using cyclic voltammetry. Third, quantitative analysis of the electron transfer kinetics has been conducted using *microchannel flow cells*, in which continuous supply of fresh electrolyte through the microfluidic channel generates time-invariant diffusion layers near the active electrode surface, allowing electrochemical measurements in steady states. To collectively explain our observations, a simple but very useful physical model is proposed; the model indicates that the observed changes in the interfacial electrochemical phenomena essentially result from the gate-induced band alignment shift at the electrode/electrolyte interfaces. Lastly, based upon the results and the insight gained from the previous experiments, possibilities and challenges in field-effect control of surface binding energies in electrocatalytic systems are explored, and rational strategies to overcome the difficulties are proposed.

Table of Contents

List of Tables

List of Figures

1. Introduction

In a metal-insulator-semiconductor (MIS) structure, electronic occupation of charge carriers (i.e., electrons and holes in conduction and valence bands, respectively) and electronic conductivity in the semiconductor layer can be modulated by a voltage applied between the semiconductor and the metallic gate.[1] This phenomenon, i.e., the local change of electronic properties in the semiconductor due to applied electric field, is called the *field effect*. Since the field effect can make even an n-type semiconductor near the insulator act like a p-type semiconductor and vice versa, the MIS structure has been widely applied in semiconductor industry to fabricate electronic switching devices such as metal-oxide-semiconductor field-effect transistors (MOSFETs).

If the semiconductor layer in a MIS structure is thin enough (specifically, comparable to or thinner than the accumulation or the inversion layer formed near the semiconductor/insulator interface), the field effect dramatically changes the electronic properties even at the surface of semiconductor. This implies that kinetics of heterogeneous

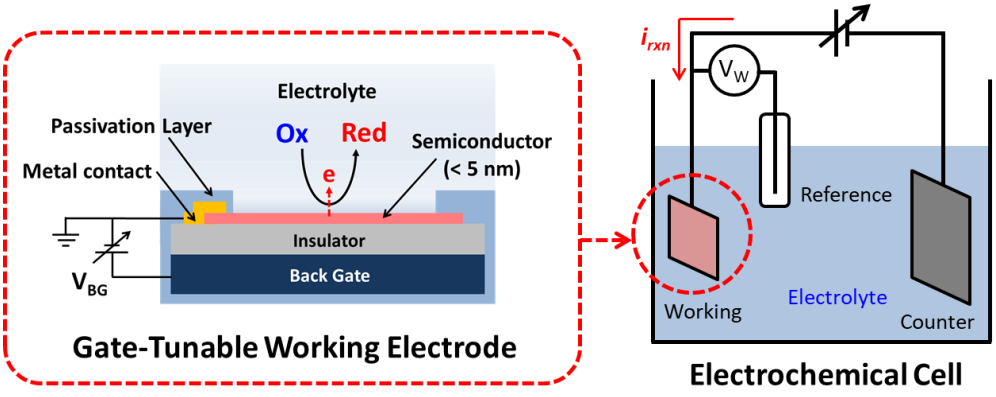

Figure 1.1. General concept of this dissertation project: that is, applying the field effect to modulate electrochemical reactions at 2D electrode surfaces.

(electro)chemical processes on an ultrathin or two-dimensional (2D) semiconductor can be controlled by the field effect. Indeed, the modulation of surface catalytic activities (typically in gas phase) by an external voltage bias, in which no net electron transfer occurs between the heterogeneous catalysts and the reactants, have been reported previously,[2–4] though the influences of the field effect on electrochemical phenomena have been rarely investigated.

The objective of this dissertation project is to apply the field effect for continuous and reversible modulation of interfacial electrochemical phenomena, which can potentially determine the overall reaction rate, on ultrathin or 2D electrodes as schematically shown in Figure 1.1. Although electrical work should be done to modify electronic structure of the 2D electrode surface, once the MIS capacitor is charged, in principle, no extra work is needed to maintain the modified surface properties. Furthermore, the energy used to charge a MIS capacitor can be fully retrieved while discharging it. Therefore, field effect modulation can be a potential means to improve energy efficiencies of electrochemical processes on 2D electrode surfaces. I believe that fundamental understanding of the field-effect-controlled interfacial electrochemical phenomena would ultimately pave the way to improved energy efficiencies of practically important (photo)electrocatalytic processes such as hydrogen evolution reaction (HER) and oxygen reduction reaction (ORR). As the first step for the ultimate goal, this dissertation focuses on demonstrating and elucidating the influence of the field effect to electric double layer (EDL) structures and charge transfer processes at 2D semiconductor/electrolyte interfaces.

1.1. Thesis Overview

The following chapters are organized as follows. Chapter 2 provides the basic concepts and theoretical background required to understand field effect modulation of interfacial electrochemical phenomena demonstrated in this dissertation. Chapter 3 outlines general ideas and some details about device structure, device fabrication, and experimental techniques commonly used in the dissertation project.

Chapter 4 through Chapter 6 present my experimental results and associated discussions, some parts of which are published or to be published in scientific journals. Chapter 4 discusses the charge transport characteristics and electrochemical behaviors of graphene field-effect transistors with the graphene channel in contact with both SiO_2 back gate and ion gel electrolyte gate, which gave the initial insight to understand the physical nature of 2D electrode/electrolyte interfaces under the field effect. In this work, from the responses of graphene channel to the two different gating mechanisms—i.e., back- and electrolyte-gating—the potentials associated with (i) energy band filling in graphene and (ii) electric double layer charging could be experimentally separated. The results presented in this chapter have been published as Chang-Hyun Kim and C. Daniel Frisbie, "Determination of Quantum Capacitance and Band Filling Potential in Graphene Transistors with Dual Electrochemical and Field-Effect Gates", *The Journal of Physical Chemistry C* **2014**, 118, 21160.

Chapter 5 discusses the field effect modulation of electrochemistry between outer-sphere redox species and 5 nm thick ZnO working electrodes prepared on SiO_2 back gates. It has been observed that back-gate-induced charge in the ZnO electrode leads to shift in

energy band alignment at the electrode/electrolyte interface, and this, in turn, changes charge transfer kinetics at a given electrode potential. To explain the observed behaviors of 2D electrode/electrolyte interfaces, a simple but very useful physical model is proposed in this chapter. This work has been published as Chang-Hyun Kim and C. Daniel Frisbie, "Field Effect Modulation of Outer-Sphere Electrochemistry at Back-Gated, Ultrathin ZnO Electrodes", *The Journal of American Chemical Society* **2016**, 138, 7220.

Chapter 6 discusses the results of steady-state kinetic analysis of the outer-sphere electrochemistry studied in Chapter 5. In this work, microfluidic channel is introduced to the devices to provide continuous supply of fresh electrolyte to the ZnO electrode surface. This generates time-invariant concentration profiles of the reactant and the product near the electrode, allowing steady-state analysis of the electrochemical reaction kinetics. It has been found that the electron density on the electrode surface increases with the voltage bias to the back gate, while the rate constant for electron transfer decreases at the same time. This behavior is explained with the model developed in Chapter 5 and an electron transfer theory. The results presented in this chapter have been prepared for submission as "Continuous and Reversible Tuning of Electrochemical Reaction Kinetics on Back-Gated 2D Semiconductor Electrodes: Steady-State Analysis using a Hydrodynamic Method" by Chang-Hyun Kim and C. Daniel Frisbie.

Chapter 7 discusses the future direction of this project, application of a back-gated 2D electrode to modulate electrocatalytic reactions, based on the results presented in Chapter 4, 5, and 6. We will explore possibilities and challenges expected in such systems, and propose rational strategies to overcome the difficulties. Lastly, specific experimental

systems for initial investigation are proposed and other candidate electrocatalytic systems that our devices are potentially applicable to are presented.

2. Motivation and Research Objectives

This chapter discusses basic concepts and previous studies that motivated this dissertation project. This chapter begins with essentials of a field-effect transistor because of its similarities in structure and operation mechanisms to the *gate-tunable* electrode employed in this project. The second and the third parts review previous reports on ultrathin or 2D semiconductors for FETs and on electrical control of heterogeneous catalytic reaction kinetics using similar device structures. Then, fundamentals and general aspects of electrochemical systems, which provide theoretical background to correctly interpret the physical phenomena demonstrated in the following chapters and insight for rational experimental design, are discussed. Lastly, specific project goals are proposed considering expected possibilities and limitations of the system.

2.1. Field-Effect Transistors (FETs): Basic Operating Mechanisms

A field-effect transistor (FET) is an electronic switch in which the electrical resistance of the semiconductor between the *source* and the *drain* electrodes is modulated with the voltage bias V_G on the *gate* electrode (Figure 2.1). Current flow through a FET is

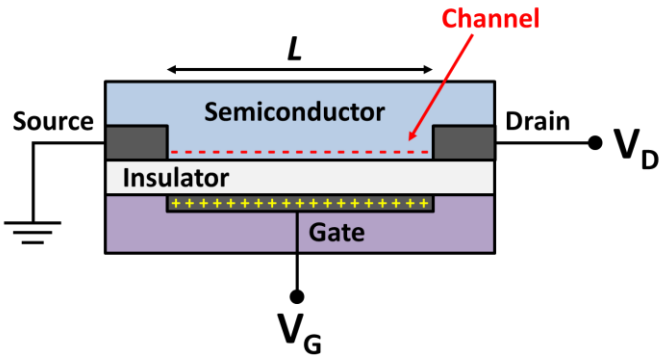

Figure 2.1. Cross-sectional schematic of a field-effect transistor and applied voltages.

analogous to water flow through a physical valve; applying a voltage bias to the gate terminal (also referred to as *gating*) can be thought as opening and closing the valve in that it creates or eliminates an electronically conductive *channel* which permits or blocks current flow between the source and the drain. The gate-dielectric-semiconductor stack is basically a parallel plate capacitor, in which V_G larger than the threshold voltage V_{T} induces mobile charge carriers (i.e., electrons or holes, depending on the type of the semiconductor and the gating condition) near the dielectric-semiconductor interface to form the essentially two dimensional *channel*. The drain voltage V_D applied between the source and the drain provides a driving force for carrier conduction in the channel. Therefore, the drain current I_D in a *linear regime* (i.e., $V_G > V_{\mathrm{T}}$ and $V_G - V_{\mathrm{T}} \gg V_D$) is given by:

$$I_D = \frac{W}{L}\mu C(V_{\mathrm{G}} - V_{\mathrm{T}})V_D \tag{2.1}$$

where μ is the carrier mobility, C is the capacitance of the dielectric layer, W and L are the width and the length of the channel, respectively. In this regime, I_D depends linearly on V_{G} in the $I_D - V_{\mathrm{G}}$ plot (transfer curve) as expected. However, as V_D increases, I_D start to saturate because the *pinched-off* region is formed near the drain. Accordingly, I_D in a *saturation regime* (i.e., $V_G > V_{\mathrm{T}}$ and $V_G - V_{\mathrm{T}} < V_D$) is given by:

$$I_D = \frac{W}{2L}\mu C(V_{\mathrm{G}} - V_{\mathrm{T}})^2 \tag{2.2}$$

The saturation of I_D is more obvious in an $I_D - V_D$ plot (output curve). The respective current-voltage characteristics of a FET in the two regimes can be seen in the output and the transfer curves shown in Figure 2.2.

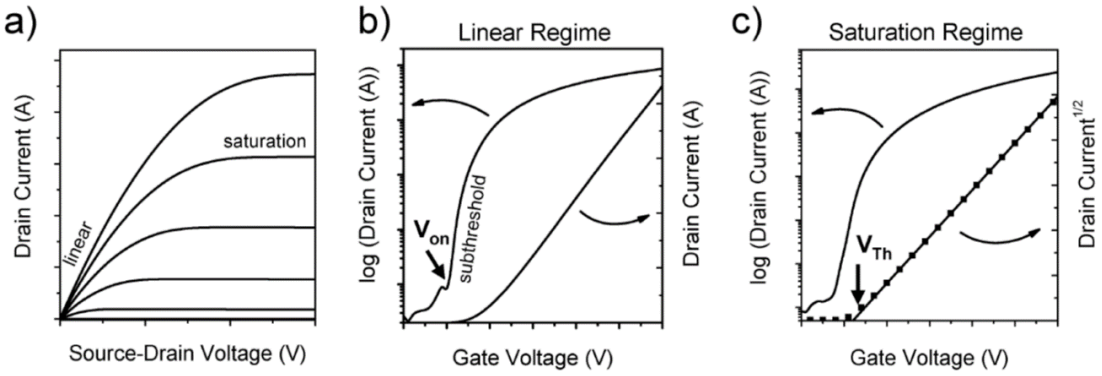

Figure 2.2. Representative current-voltage characteristics of an n-channel field-effect transistor: (a) $I_D - V_D$ characteristics (output curve); (b) $I_D - V_G$ characteristics (transfer curve) in the linear regime ($V_D \ll V_G - V_T$); (c) $I_D - V_G$ characteristics in the saturation regime ($V_D > V_G - V_T$) [Reprinted with permission from ref. 5; Copyright 2007 by the American Chemical Society]

It is noteworthy that not only traditional insulating materials like SiO_2 and Al_2O_3 but electrolyte like ionic liquid,[6] which generally have a wide electrochemical stability window (~4−7 V), can serve as the gate dielectric of a FET because the electric double layer (EDL) formed at the semiconductor/electrolyte interface is essentially a nanometer-thick dielectric capacitor (note: more details about the EDL structure is discussed in Section 2.4). Thanks to its huge capacitance on the order of 1-10 μF/cm^2, the *electrolyte gating* has been employed in a wide variety of research projects, spanning fundamental charge transport in the high carrier density regime[7–10] to practical applications including flexible electronics[11–16] and biosensors[17,18] that require low voltage operation (< 2 V).

2.2. Ultrathin or 2D Semiconductors for FETs

Due to the demand for higher performance of computer chips, the dimensions of FETs have been continuously decreased. Accordingly, devices with shorter channel lengths have begun to experience high off-state currents. The resulting challenges of increased

static power consumption and associated heat dissipation are collectively termed short-channel effects.[19,20] As one of the potential solutions to address the short-channel effects, ultrathin or 2D semiconductors have been received great attention because the characteristic channel 'scaling length' is given by $\lambda = \sqrt{t_s t_b (\varepsilon_s/\varepsilon_b)}$, where t_s is the semiconductor thickness, t_d is the gate dielectric thickness, and ε_s and ε_b are dielectric constants of the semiconductor and the gate dielectric, respectively.[19–21] Most actively investigated 2D semiconductors include graphene and transition metal dichalcogenides (TMDs) such as MoS_2 and WSe_2. The 2D semiconductors are usually prepared either by top-down approach such as mechanical[22–24] or chemical[25,26] exfoliation of bulk layered materials or by bottom-up approach preparing atomically thin films using, for example, chemical vapor deposition (CVD).[27,28]

Graphene. Graphene is the most widely studied 2D material because of its relatively long history, an extraordinary carrier mobility as high as ~25,000 $cm^2V^{-1}s^{-1}$ at room temperature,[29] and lack of dangling bonds. Graphene comprises atomically thin (~4 Å) sheet of carbon atoms with the sp^2-hybridized honeycomb crystal structure. The electrons in the p-orbitals are delocalized among the atoms, giving rise to the unique linear dispersion in graphene.[30] Since graphene is a zero-bandgap semiconductor (i.e., semimetal), on/off ratios smaller than 10 are typically observed in graphene FETs.[31] A small bandgap of ~0.1 eV can be generated in ~10 nm wide graphene nanoribbons,[32,33] but this usually requires challenging nanofabrication techniques such as electron beam lithography.

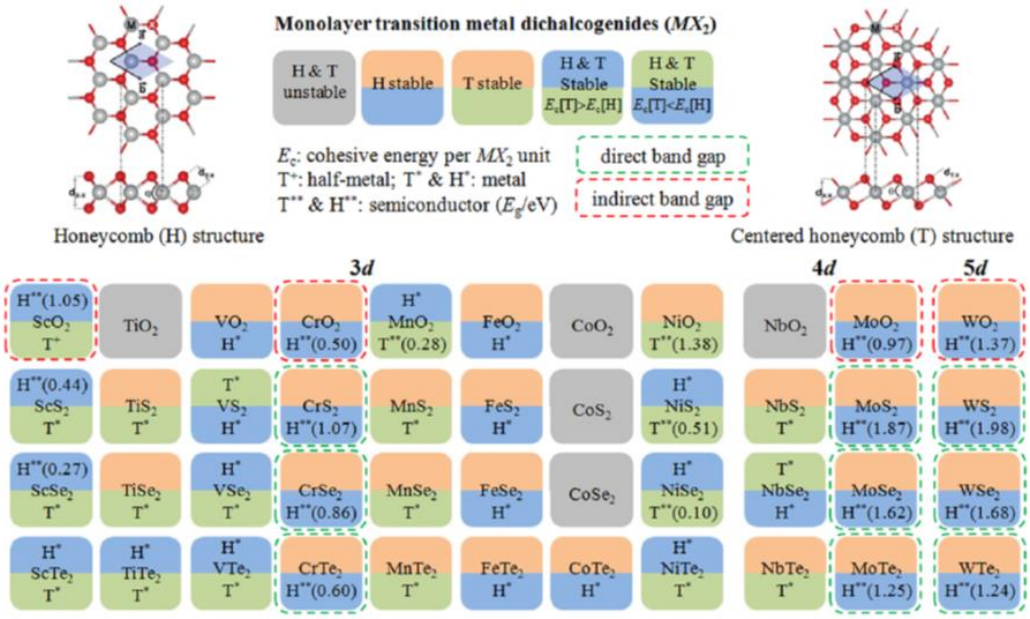

Figure 2.3. Summary of stability analysis and semiconducting properties of 44 different transition metal dichalcogenides (MX_2). Transition metal atoms indicated by M are divided into 3d, 4d, and 5d groups. MX_2 compounds shaded light gray form neither stable H (2H-MX_2) nor T (1T-MX_2) structure. In each box, the lower-lying structure (H or T) is the ground state. The resulting structures (T or H) can be half-metallic (+), metallic (*), or semiconducting (**) with direct or indirect band gaps. [Reprinted with permission from ref. 34; Copyright 2013 by the American Chemical Society]

Transition Metal Dichalcogenides. TMDs have general formula of MX_2, where M is a transition metal from group 4, 5, or 6, and X is a chalcogen atom (i.e., S, Se, and Te). A single layer of these materials consists of three atomic layers in the form of X-M-X.[35] Depending on its atomic composition, TMD can be a semiconductor (e.g., MoS_2, WS_2, and $MoSe_2$), a semimetal (e.g., WTe_2 and $TiSe_2$), a metal (e.g., NbS_2 and VSe_2), or an insulator (e.g., HfS_2). The structures and the electronic properties of different TMDs are summarized in Figure 2.3. Most FET research has focused on MoS_2, although WS_2, WSe_2, and other TMDs have also been investigated.[21,36,37] The great interest in MoS_2 is due to the higher availability of high quality 2D crystals, and its mechanical and chemical robustness.

Electron mobility up to ~200 $cm^2V^{-1}s^{-1}$ and on/off ratios exceeding 10^8 have been observed in monolayer MoS_2 FETs.[38]

Ultrathin 3D Semiconductors. An alternative option to prepare a 2D semiconductor is growing an ultrathin semiconductor film with thin film growth techniques such as molecular beam epitaxy (MBE), chemical vapor deposition (CVD), atomic layer depositions (ALD), sputtering, and pulsed laser deposition (PLD). MBE and ALD, the most suitable film growth techniques for this project, and semiconductor films grown by the respective methods are briefly reviewed here.

Despite its slow film growth rates and very complicated setup, MBE can produce the best quality single crystalline epitaxial films with extremely low extended defect density. At its core, MBE is simply an ultra-high vacuum (UHV) evaporation technique, in which beams of atomic and molecular species are thermally evaporated and are incorporated into a heated substrate placed in the line of sight of the emerging beams. The chemical composition of the growing film is controlled by mechanical shutters placed in front of the thermal beams. Major advantages of MBE[39] are: (i) unintentional impurity incorporation can be extremely low on the order of $10^{13}/cm^3$ in the best GaAs MBE systems; (ii) with typical growth rates between 0.1 and 2 monolayers per second, atomically abrupt interfaces of dissimilar materials can be produced; (iii) UHV conditions allow numerous *in situ* diagnostic techniques that allows realtime feedback on the state of the growing film. Ko et al.[40] reported high-performance nanoscale FETs showing field-effect mobility of 5,500 $cm^2\ V^{-1}\ s^{-1}$, which were made of a single crystal InAs film grown by MBE.

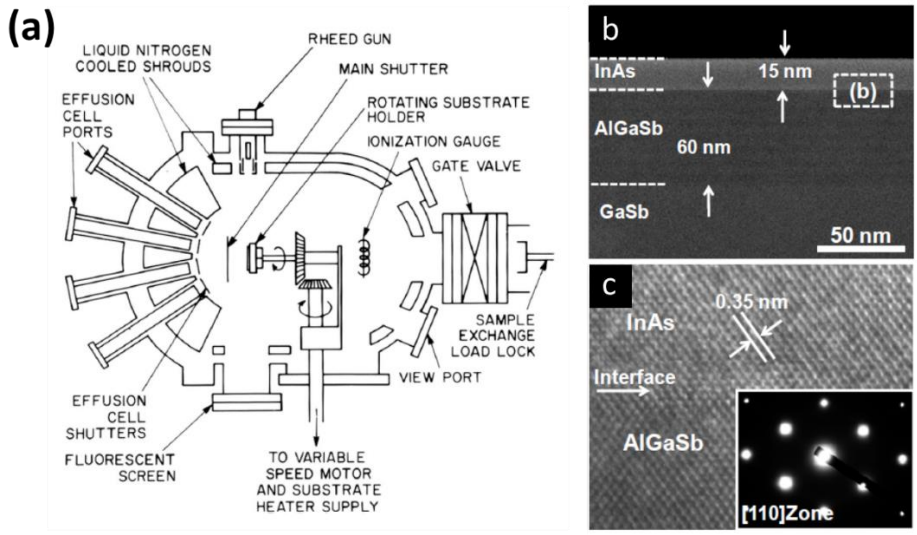

Figure 2.4. (a) Cross-sectional schematic of an MBE system. (b) Cross-sectional TEM image of the InAs thin film (15 nm thick) grown epitaxially on a ~60 nm thick $Al_{0.2}Ga_{0.8}Sb$ layer on a bulk GaSb wafer. (c) High-resolution TEM image and corresponding electron diffraction pattern of the single-crystalline structure of the InAs thin film in (b). [(a) is adapted from ref. 41 with permission; Copyright 2013 by the American Institute of Physics. (b) and (c) are adapted from ref. 40 with permission; Copyright 2010 by the Nature Publishing Group]

By using ALD, which differs from CVD by keeping the precursors strictly separated from each other in the gas phase, very uniform films can be grown in layer-by-layer manner thanks to the self-limiting surface chemistry of the precursors.[42] The advantages of ALD include[43] (i) accurate and simple thickness control (growth per cycle), (ii) no need to control the reactant flux homogeneity, and (iii) large area uniformity and excellent conformality. ALD, however, also has several limitations including (i) low deposition rates, (ii) limited availability of precursors for some elements such as Ba and Si, and (iii) low crystallinity in some cases, due to the low deposition temperature. Plasma-enhanced ALD (PEALD) instruments are equipped with plasma sources, which generate more reactive precursors, to grow films with a higher degree of stoichiometry at lower

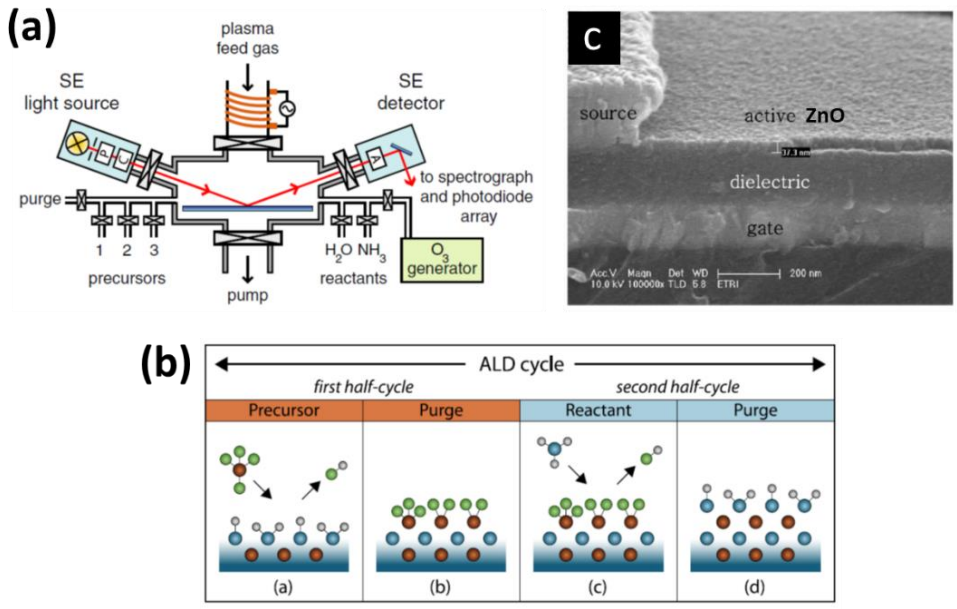

Figure 2.5. (a) Cross-sectional schematic of a single-wafer PEALD reactor equipped with spectroscopic ellipsometer (SE) for *in-situ* film thickness measurements. (b) Typical ALD process illustrated for the two half-cycles of the deposition process. (c) Cross-sectional SEM image of the ZnO-TFT between the source and the drain. [(a) and (b) are adapted from ref. 44 with permission; Copyright 2009 by IOP Publishing Ltd. (c) is adapted from ref. 45 with permission; Copyright 2008 by the Electrochemical Society]

temperature. Although ALD has been mostly applied to deposit high-k dielectric materials in the semiconductor industries, several semiconductor films including ZnO and SnO_2 for electronic applications have been grown by ALD as well.[46] FETs made of ALD-grown ZnO films[45,47] generally show relatively low mobilities on the order of ~0.1−1 $cm^2\ V^{-1}\ s^{-1}$.

2.3. Electrical Control of Heterogeneous Chemical Reactions

In light of strong relationship between the electronic structure of a solid and the reaction kinetics on it,[49–51] electrical control of heterogeneous reactions on solid surface is an intriguing concept that has been demonstrated to some degree in previous works. For instance, it has been reported that activities of several metal and oxide catalysts (e.g., Pt, Pd, Rh, Ag, IrO_2, and Ni) are greatly increased in stacked catalyst/solid-electrolyte/metal(counter) structures when a voltage is applied between the catalyst and the metallic counter electrode. This phenomenon, referred to as non-Faradaic electrochemical modification (NEMCA),[48] has been demonstrated for about 100 catalytic reaction systems with many solid-electrolytes, including O^{2-}, F^{-}, Na^{+}, and H^{+} conductors. The increases in the catalytic rate up to a factor of 200 were reported with the Λ-factor (NEMCA factor), which describes the ratio of non-Faradaic to Faradaic portions of the increased reaction rate, ranging up to 3×10^5. A series of experimental studies[52–55] (e.g., TPD, XPS, SERS, work function, and CV) suggest that the NEMCA effect occurs due to the

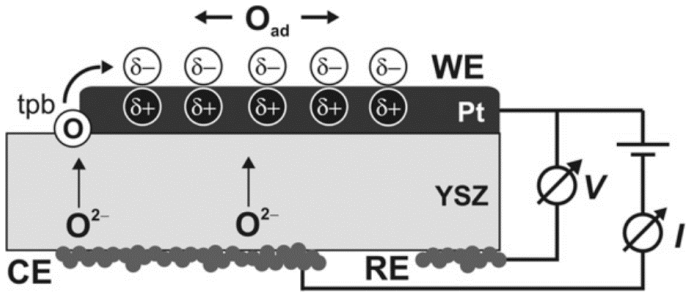

Figure 2.6. Schematic showing the electrochemically induced spillover of oxygen ions onto the surface of the metal electrode in a NEMCA system. The oxygen ions which are transported through the yttrium-stabilized zirconia (YSZ) solid electrolyte are discharged at the three-phase boundary (tpd) and the discharged oxygen species then migrate onto the surface of the Pt electrode. [Adapted from ref. 48 with permission; Copyright 2010 by Elsevier Ltd.]

electrochemically controlled back-spillover (migration) of promoting ionic species (e.g., $O^{\delta-}$, $Na^{\delta+}$) from the solid-electrolyte to the gas-exposed catalyst surface.[48] The back-spillover occurs at the three-phase boundary (i.e., catalyst/gas/solid-electrolyte) to establish an 'effective electric double layer' on the catalyst surface, altering its work function and thus its chemisorptive and catalytic properties. Although nearly all NEMCA studies were conducted for gas-phase reactions (in 10^{-2} mbar to atmospheric pressure) at high temperature, NEMCA effect in solution phase at room temperature have been reported in a few systems including oxidation of H_2 on Pt/graphite catalyst in weak alkali solutions.[56,57]

Recently, Zhang *et al.*[3] reported the field-effect-controlled catalytic oxidation of CO on a SnO_2 nanowire placed on degenerately doped Si covered with 300 nm SiO_2. By monitoring conductivity change in the SnO_2 nanowire, they found the extent and the rate of O_2 adsorption are influenced by the gate bias. The rate constant of O_2 adsorption at zero gate bias is 3 times larger than those with -4 V gate bias. Baker *et al.*[4] reported that CO oxidation on 4 nm Pt film deposited on doped n-type Si substrate, which forms a Schottky barrier, can be controlled by external bias and light. The CO oxidation can be turned on and off with applying 1 V reverse bias and zero bias, respectively. The authors attribute the enhanced CO oxidation on the negatively biased Pt surface to the facilitated transition of CO into a negatively charged CO_2^- transition state which is predicted in a density functional theory (DFT) study.[58]

These publications suggest that electrical control of the electronic structure can be an effective way to tune heterogeneous reaction kinetics on solid surfaces. Despite the prior work on controlling non-Faradaic reactions, however, there have been only a few

reports[59,60] on field effect modulation of Faradaic (i.e., electrochemical) reactions at solid/liquid interfaces.

2.4. General Aspects of Electrochemical Systems

Reactions in Electrochemical Systems. An electrochemical reaction refers to a chemical transformation caused or accompanied by the electron transfer across the interface between different chemical phases; for example, between an electronic conductor (an *electrode*) and an ionic conductor (an *electrolyte*). Typical electrode materials include solid metals (e.g., Pt, Au), liquid metals (e.g., Hg, amalgams), carbon, and semiconductors (e.g., Si, ZnO). The most frequently used electrolyte are liquid solutions containing ionic species in either water or non-aqueous solvent. Less conventional electrolytes include fused salts, room temperature ionic liquids, and solid-state ionic conductor (e.g., sodium β-alumina). For an electrochemical reaction to occur continuously, an appropriate *electrochemical cell*, which typically consists of two electrodes (i.e., an *anode* and a *cathode*, at which oxidation and reduction occur, respectively) separated by at least one electrolyte phase as schematically shown in Figure 2.7, should be established. The overall reaction taking place in the cell is made up of two independent *half reactions* at the two electrodes as follows:

$$\text{Cathode:} \qquad \nu_{\mathrm{O}}\mathrm{O} + ne \rightarrow \nu_{\mathrm{R}}\mathrm{R} \tag{2.3}$$

$$\text{Anode:} \qquad \nu_{\mathrm{R}'}\mathrm{R}' \rightarrow \nu_{\mathrm{O}'}\mathrm{O}' + me \tag{2.4}$$

where *e* indicates the electron; *n*, *m*, and ν's are the stoichiometric coefficients; O and R indicate oxidized and reduced species, respectively. When one is interested in only one of

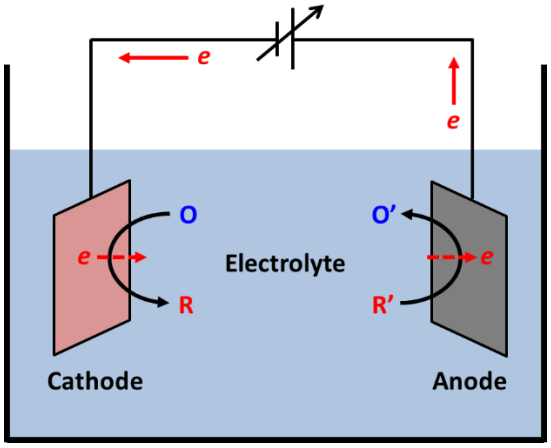

Figure 2.7. A schematic of an electrochemical cell consisting of a cathode, an anode, and an electrolyte phase in which reactants O, R, O', and R' are dissolved.

these reactions, the electrode at which the reaction of interest occurs is called the *working* electrode and the other electrode is called the *counter* electrode. For the charge neutrality of each chemical phase to be maintained, the current flowing at the working and the counter electrodes should be the same. An electrochemical cell is often configured with an additional *reference* electrode, which is designed to indicate a fixed solution potential, connected to a high impedance voltmeter to measure the working electrode potential on a standardized scale.

An important characteristic of electrochemical reactions, which is distinguished from non-Faradaic chemical reactions, is that one can freely (but not independently) control the potential (i.e., energy of electrons) or the current (i.e., the direction and the rate of the corresponding reaction) at the working electrode. In other words, the thermodynamics and the kinetics of an electrochemical reaction can be controlled by changing the potential or the current applied at the working electrode. The equilibrium potential U_{eq} of the half reaction in equation 2.3 is determined by the Nernst equation:

$$U_{\mathrm{eq}} = U^0 + \frac{RT}{nF} \ln \frac{{a_{\mathrm{O}}}^{\nu_{\mathrm{O}}}}{{a_{\mathrm{R}}}^{\nu_{\mathrm{R}}}} \tag{2.5}$$

where U^0 is the standard reduction potential of the reaction, R is the gas constant, T is the temperature, F is the Faraday constant, and a_{i} is the activity of species i. When a potential $U < U_{\mathrm{eq}}$ is applied to the working electrode, the forward (i.e., cathodic) reaction occurs, while the reverse (i.e., anodic) reaction occurs when a potential $U > U_{\mathrm{eq}}$ is applied. The additional potential applied to the cell (i.e., $\eta = U - U_{\mathrm{eq}}$), also referred to as *overpotential*, represents the driving force to induce a certain level of the reaction rate (i.e., reaction current). Figure 2.8 schematically shows how the free energies associated with thermodynamics and kinetics change at two different electrode potentials: one at $U = U_{\mathrm{eq}}$ and the other at $U < U_{\mathrm{eq}}$. Simply speaking, improving the kinetics and the energy efficiency of an electrochemical reaction is achieved by reducing the overpotential to attain the desired reaction rate. Alternatively, the reaction kinetics can be expressed in terms of activation energies (i.e., $\Delta G_f^{\ddagger}$ and $\Delta G_b^{\ddagger}$ in Figure 2.8) as discussed later in this section.

When one considers the kinetics of an electrochemical reaction, it is important to note that many steps other than the interfacial charge transfer step may involve in the overall reaction. Figure 2.9 shows an example of electrochemical reaction pathway, in which an overall reaction, $\mathrm{O} + ne \rightarrow \mathrm{R}$, composed of a series of steps that the dissolved oxidized species, O, is converted to a reduced form, R, also in solution. The overall reaction rate is determined by the rates of processes including:[61]

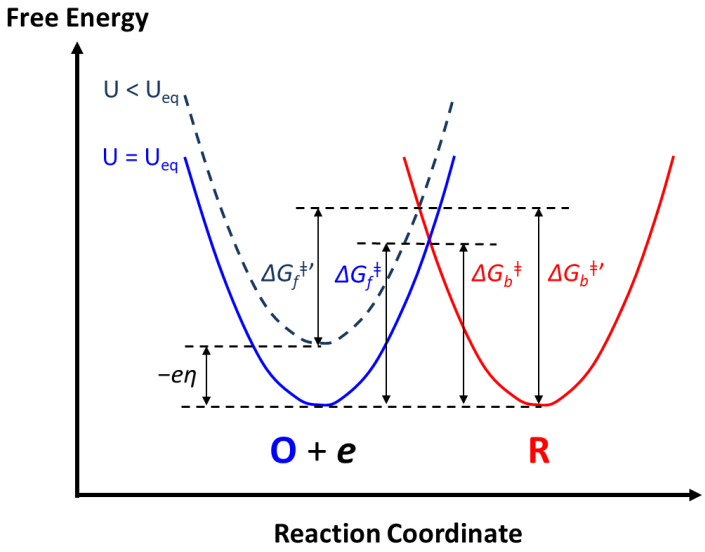

Figure 2.8. A representation of the energy change during the reaction ($O + e \rightarrow R$) at equilibrium ($U = U_{eq}$) and a negative bias ($U < U_{eq}$). In this example, the potential surface of O is assumed to be simply shifted up and down, while the shape does not change, by the bias U applied to the working electrode.

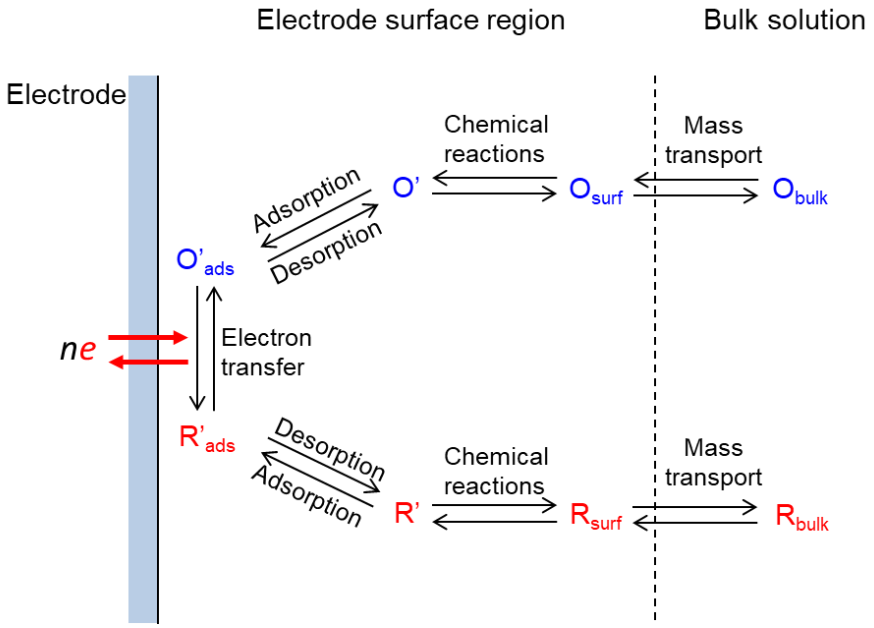

Figure 2.9. An example of multi-step electrochemical reaction pathway. [Reproduced from ref. 61 with permission; Copyright 2000 by John Wiley & Sons, Inc]

1. Mass transport of reaction species between the bulk solution and the electrode surface.
2. Electron transfer at the electrode/solution interface.
3. Chemical reactions preceding or following the electron transfer, which might be homogeneous processes (e.g., protonation or dimerization) or heterogeneous ones (e.g., catalytic decomposition) on the electrode surface.
4. Other surface interactions of reaction species, such as adsorption, desorption, or crystallization.

The rate constants for some interfacial processes (e.g., electron transfer and surface binding) depend on the electrode potential. While the simplest reactions consisting of only a series of mass transport of the reactant, interfacial electron transfer, and mass transport of the product have been commonly found in fundamental studies, more complex reaction pathways involving branching mechanisms, parallel paths, or modifications of the electrode surface are also quite common. In many cases, overall reaction rate is limited by one or more particularly slow *rate-determining steps* (RDS).

The reaction route and the activation energies of each reaction step strongly depend on catalytic action of electrode surface or mediator (i.e., homogeneous electrocatalyst) species in solution. An important example of catalytic action lowering the activation energy thereby increasing the reaction rate is hydrogen evolution reaction (HER) on platinum.[62,63] Protons in solution can be reduced at a platinum surface with much less energy because the resulting hydrogen atoms form strong covalent bond to the surface (Volmer reaction) rather than become free radicals in solution. The two adsorbed hydrogen atoms can then recombine on the platinum surface (Tafel reaction), or a proton neighbor of the adsorbed hydrogen atom can be reduced (Heyrovsky reaction), to generate a free hydrogen molecule

with very low activation energy. Similarly, many other heterogeneous reactions on electrocatalysts (e.g., oxygen reduction reaction, ORR) involve with specific adsorption and desorption of reaction species on electrode surfaces before and after electron transfer,[61,64,65] and the surface biding energies of some important reaction species have been found to be key descriptors determining the electrocatalytic activity.[66,67] It is important to recognize that surface binding energy of a reaction species is a direct and strong function of electronic structure of electrocatalyst surface. The correlation between electronic structure and electrocatalytic activity will be discussed later in Chapter 7.

Conceptually, activation energy of each reaction step can be represented as a resistance in the equivalent circuit; an inherently facile reaction step has a smaller resistance than a relatively sluggish step. Accordingly, in a given reaction pathway composed of a series of reaction steps, the total overpotential η to attain a certain level of steady-state current i can be considered as a sum of terms associated with each reaction step (i.e., voltage drop on each resistance). In most electrochemical cells, the overpotential η can be expressed as a sum of the contributions from (i) ohmic resistance, (ii) charge transfer and other interfacial interactions, and (iii) mass transport in solution as follows:

$$\eta = U - U_{eq} = iR + \eta_{\text{act}} + \eta_{\text{conc}} \tag{2.6}$$

where i is the current, R is the total ohmic resistance of the cell, and η_{act} and η_{conc} are referred to as *activation overpotential* and *concentration overpotential*, respectively. In fundamental investigations of electrochemical reaction kinetics, the activation overpotential η_{act} is of main interest because it represents the intrinsic kinetics on the

electrode materials. Therefore, it is preferred to minimize or correct the ohmic and the mass transport contributions in such measurements. In a typical electrochemical cell, electronic conductivity of the electrode (e.g., >10 S/cm for carbon) and ionic conductivity of the electrolyte (e.g., ~8 mS/cm for 0.1 M NaCl aqueous solution) are high enough such that the ohmic polarization becomes negligible. When the ohmic polarization is not negligible, it can be corrected by *IR compensation*,[68,69] which denotes the techniques basically identifying the ohmic resistance *R* and eliminating the ohmic contribution iR in the total overpotential. The concentration overpotential at low to medium current level can be mitigated and corrected by inducing a forced convection near the electrode surface using hydrodynamic methods. For example, on a rotating disk electrode (RDE), mass transport effects of reaction species can be corrected using the Koutecky-Levich equation[61] which is given by:

$$\frac{1}{i} = \frac{1}{i_k} + \frac{1}{i_{l,c}} = \frac{1}{i_k} + \frac{1}{0.62nFA{D_O}^{2/3}\varpi^{1/2}\nu^{-1/6}{c_O}^*} \tag{2.7}$$

where i_k represents the current in the absence of any mass transport effects, $i_{l,c}$ is the mass-transport-limiting current, A is the active electrode area, D_O is the diffusion coefficient of the oxidized species, ϖ is the angular velocity of the rotating electrode, ν is the kinematic viscosity of the electrolyte, and ${c_O}^*$ is the bulk electrolyte concentration of the oxidized species.

Charge Transfer Theories. The general description of charge transfer across an electrode/electrolyte interface is based on the transition state theory. The interfacial charge

transfer rate is proportional to (i) the density of the appropriate reaction species at the electrode/electrolyte interface; (ii) the density of charge carriers at the electrode surface (this factor is usually omitted in metal electrodes because it hardly varies); and (iii) a Boltzmann factor describing the "activated state" that the system must reach before the charge transfer can occur. Therefore, considering an electron transfer reaction, $\mathrm{O} + e \rightarrow \mathrm{R}$, and the associated energy diagram in Figure 2.8, the reduction current j_{c} is given by:

$$j_{\mathrm{c}} = -ek_{\mathrm{c}}n_s c_{\mathrm{O}} \exp\left(-\frac{\Delta G_f^{\ddagger}}{k_B T}\right) \tag{2.8}$$

where e is the absolute charge of an electron, k_{c} is the rate constant, n_s is the electron density at the surface, c_{O} is the concentration of O at the electrode surface, k_B is the Boltzmann constant, and T is the temperature. Similarly, the anodic current j_{a} is given by:

$$j_{\mathrm{a}} = ek_{\mathrm{a}}p_s c_{\mathrm{R}} \exp(-\frac{\Delta G_b^{\ddagger}}{k_B T}) \tag{2.9}$$

where k_{a} is the rate constant, p_s is the hole density at the surface, c_{R} is the concentration of R at the electrode surface. These equations can be further reduced by assuming linearity between the activation energies and the electrode potential, giving the Butler-Volmer equations as follows:

$$j_{\mathrm{c}} = -ek_0 c_{\mathrm{O}} \exp\left(\frac{-\alpha F\left(U - U^{0'}\right)}{RT}\right) \tag{2.10}$$

$$j_{\mathrm{a}} = ek_0 c_{\mathrm{R}} \exp\left(\frac{(1-\alpha) F\left(U - U^{0'}\right)}{RT}\right) \tag{2.11}$$

where k_0 is the *standard rate constant*, R is the gas constant, $U^{0'}$ is the formal potential of the reaction, and α is the transfer coefficient, which can range from zero to unity depending on the shape of intersection region in Figure 2.8.

Although the general model is in most cases correct and accurate, the origin of the activation energy is not well defined. For charge transfer at semiconductor/electrolyte interfaces, it is usually more convenient to use the specific model, incomplete though it is, of charge transfer between energy levels. The Gerischer model[70,71] is a convenient generalization of such energy level based descriptions. The simplest model assumes negligible phonon emission during electron transfer, and negligible electronic coupling between initial and final states.[64] This simplest energy level description gives one very specific origin for the activation energies: fluctuation of the energy levels of reaction species in the solution. The rate of charge exchange between an electrode and a solution is proportional to (i) the probability that appropriate reactant in solution is within tunneling distance (~30 Å) from the surface, and (ii) the probability that its energy level is thermally fluctuated to be at an "activated state" where electrons can tunnel to or from the electrode without change in energy.[64] This simple tunneling-based mechanism is referred to as the *outer-sphere* electron transfer. More complex mechanisms, including cases where a ligand or other ion in solution acts as a "bridge" for electron transfer or equivalently as a resonance energy level to aid tunneling, are collectively referred to as the *inner-sphere* electron transfer.

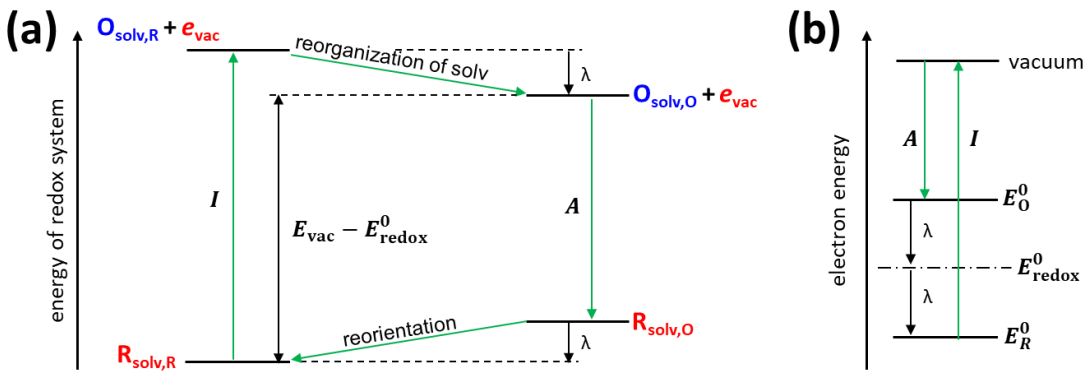

Figure 2.10. (a) A thermodynamic cycle associated with the reaction ($O + e \rightleftarrows R$) and solvent reorganization energy λ. (b) Representation of the energy relationships in (a) in terms of electronic energy levels of O and R (E^0_O and E^0_R, respectively). *I* and *A* denote the energy changes associated with the step that R is ionized generating an electron in vacuum level (E_{vac}), and the reverse step that the electron in vacuum level falls back to LUMO of O to form R, respectively. E^0_{redox} indicates the standard potential of the reaction. Note that the subscript (solv,O) and (solv,R) indicate the solvent orientations in energetically favorable states for O and R, respectively. [Reproduced from ref. 72 with permission; Copyright 1983 by Springer International Publishing]

The Gerischer model explains that the energy difference between the redox species O and R in the solution is caused by *solvent reorganization*. Figure 2.10a shows the thermodynamic cycle associated with the solvent reorganization processes after charge transfer. Before charge transfer occurs, redox species are surrounded by solvation shells with different solvent orientations which make them in energetically more favorable states, $O_{(solv,O)}$ and $R_{(solv,R)}$, respectively; the subscript (solv,O) and (solv,R) indicate the respective solvation orientations typical at equilibrium. When an electron is extracted from $Red_{(solv,R)}$ to the vacuum level, it ends up at first with $O_{(solv,R)}$ because the electron transfer is much faster ($\tau = \sim 10^{-15}$ sec) than the reorganization of the solvation shell and the solvent dipoles ($\tau = \sim 10^{-11}$ sec). Thereafter, the solvent dipoles eventually reorganize themselves until the $O_{(solv,R)}$ reaches the stable $O_{(solv,O)}$ state. Similarly, when $O_{(solv,O)}$ receives an electron, it

ends up at first with $R_{(solv,O)}$ and relaxed into the stable $R_{(solv,O)}$ state. The energy relationship in Figure 2.10a can be redrawn in terms of the electronic energy levels of the redox species as shown in Figure 2.10b. The reorganization energy λ can be estimated as the sum of two contributions, the inner (λ_i) and the outer-sphere (λ_o) reorganization energies, which can be can be estimated by Marcus relations as follows:[73]

$$\lambda_i = \frac{1}{2}\sum_j \frac{f_j^{ox} f_j^{red}}{f_j^{ox} + f_j^{red}} \Delta x_j{}^2 \tag{2.12}$$

$$\lambda_o = \frac{e^2}{8\pi\varepsilon_0}\left(\frac{1}{r} - \frac{1}{2d}\right)\left(\frac{1}{\varepsilon_{op}} - \frac{1}{\varepsilon_s}\right) \tag{2.13}$$

where f's are force constants for the jth ion-solvent bond; Δx_j is the displacement in the bond length; ε_0 is the permittivity of free space; r is the radius of redox molecule; d is the distance to the reactant from the surface (usually set to infinity); ε_{op} and ε_s are the optical and the static dielectric constants of the solvent, respectively. Typical values of λ range from 0.5 to 2 eV.

Thermal fluctuation of the solvation shells makes the energy levels of O and R in solution essentially behave like an acceptor and a donor 'bands', respectively. Assuming harmonic oscillation of the solvation shell, Gaussian type distribution functions for the acceptor and the donor states are obtained as follows:

$$D_O(E) = (4\pi k_B T\lambda)^{-\frac{1}{2}} c_O \exp\left[-\frac{(E - E^{0\prime} - \lambda)^2}{4k_B T\lambda}\right] \tag{2.14}$$

$$D_R(E) = (4\pi k_B T\lambda)^{-\frac{1}{2}} c_R \exp\left[-\frac{\left(E - E^{0\prime} + \lambda\right)^2}{4k_B T\lambda}\right] \tag{2.15}$$

where E is the energy level and $E^{0\prime}$ is the energy level corresponding to the formal potential of the reaction. Cathodic and anodic current densities (j_c and j_a, respectively) across the electrode/electrolyte interface are given by:

$$j_c = -e\kappa Z \int_{-\infty}^{\infty} \underbrace{f(E)D(E)}_{\text{occupied}} \underbrace{D_O(E)}_{\text{empty}} dE \tag{2.16}$$

$$j_a = e\kappa Z \int_{-\infty}^{\infty} \underbrace{(1-f(E))D(E)}_{\text{empty}} \underbrace{D_R(E)}_{\text{occupied}} dE \tag{2.17}$$

where κ is the transmission coefficient (having a value between 0 and 1), Z is the frequency factor for the electron transfer, $f(E)$ is the Fermi-Dirac distribution function, and $D(E)$ is the density of states (DOS) of the electrode surface. These equations indicate that the charge transfer rate at a given E is essentially determined by the energy states overlap of occupied and empty states between the two phases as schematically shown in Figure 2.11.

For a wide bandgap n-type semiconductor, in which the valence band edge (E_v) is located far below $E^{0\prime}$, equation 2.16 and 2.17 can be further reduced to:

$$j_c \approx -\frac{e\kappa Z}{(4\pi k_B T\lambda)^{\frac{1}{2}}} \exp\left[-\frac{\left(E_c - E^{0\prime} - \lambda\right)^2}{4k_B T\lambda}\right] n_s\, c_O = -ek_c\, n_s\, c_O \tag{2.18}$$

$$j_a \approx \frac{e\kappa Z}{(4\pi k_B T\lambda)^{\frac{1}{2}}} \exp\left[-\frac{\left(E_c - E^{0\prime} + \lambda\right)^2}{4k_B T\lambda}\right] p_s c_O \;=\; ek_a\, p_s\, c_R \tag{2.19}$$

where k_c and k_a are the rate constants for cathodic and anodic charge transfer, E_c is the conduction band edge level, and n_s and p_s are the surface concentrations of electrons and

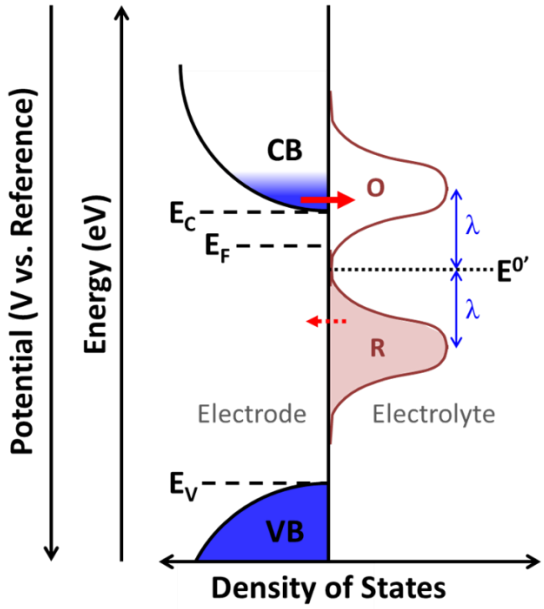

Figure 2.11. Illustration of energy level distributions at an electrode/electrolyte interface. The red arrows indicate the electron transfer across the interface. This specific example shows the case of a wide bandgap semiconductor electrode and equimolar O and R dissolved in solution.

holes on the electrode, respectively. When the Fermi level E_F lies more than $2k_BT$ below E_c, n_s and p_s in equation 2.18 and 2.19 can be approximated as:

$$n_s = N_c \exp\left[-\frac{(E_c - E_F)}{k_B T}\right]; \quad p_s = N_c \tag{2.20}$$

where N_c is the effective DOS at the lower edge of the conduction band.

Electric Double Layers. When an electronic conductor is brought into an ionic conductor (i.e., electrolyte), an electric double layer (EDL) almost inevitably forms at their interface. The double layer consists of layers of positive and negative charges, and region of high electric field between, or within, the charged layers. It is often very important to consider the existence of the double layers to correctly describe many physical phenomena

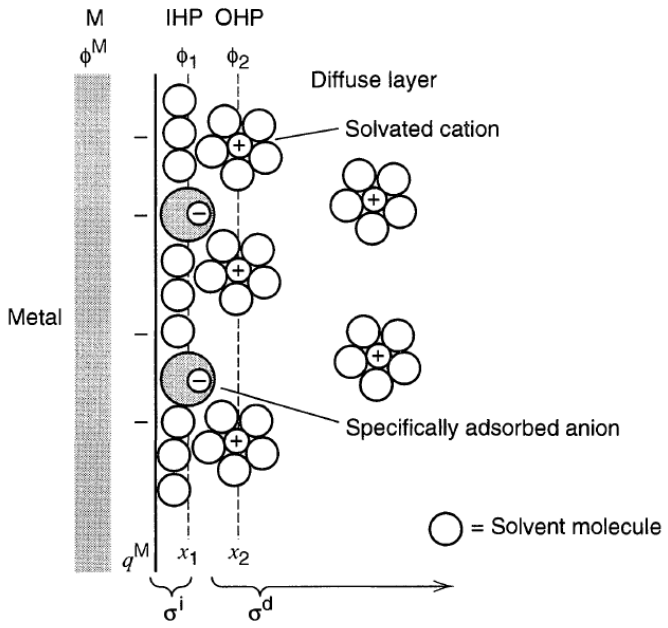

Figure 2.12. Structure of electric double layer (EDL) formed at a metal/solution interface. [Reproduced from ref. 61 with permission; Copyright 2000 by John Wiley & Sons, Inc]

occurring at the electrode/electrolyte interfaces, because they are dominant in controlling the electrical and chemical properties of the electrode surface. Figure 2.12 shows an example of EDL structure formed at a solid/liquid interface. The solid side simply consists of a 2D charge plane (in case of metal) or a space charge layer (in case of semiconductor). In contrast, the solution side may have a more complex structure with multiple layers. The *inner layer*, which contains solvent molecules and sometimes other species (ions and molecules) that are *specifically* adsorbed on the solid surface; the specific adsorption generally accompanies a chemical bonding between the adsorbate and the solid surface. The locus of the electrical centers of the specifically adsorbed ions is called the *inner Helmholtz plane* (IHP).[61] In contrast, the long range electrostatic interaction makes the solvated ions in the solution be *non-specifically* adsorbed to the solid surface. Since the

size of the solvated ions limits the distance that they approach the surface, the centers of these nearest solvated ions defines the *outer Helmholtz plane* (OHP). Because of thermal agitation in the solution, the non-specifically adsorbed ions can be distributed over a relatively long range, which can extend from the OHP into the bulk solution, to form the *diffuse layer*. The thickness of the diffuse layer depends on the ionic concentration of the solution; for concentrations greater than 0.01 M, the thickness is less than ~10 nm. In a sufficiently highly concentrated electrolyte, the excess charge and the potential drop in the diffuse layer can be ignored and only those within the OHP are considered. For the charge neutrality of the system to be satisfied, the total excess charge in these layers in the solution should be the same as the total charge induced in the solid. The overall potential distribution within the solid and the solution phase is determined by Poisson's equation:

$$\frac{d^2\phi}{dx^2} = -\frac{\rho}{\varepsilon\varepsilon_0} \tag{2.21}$$

where ε is the relative permittivity, ε_0 is the permittivity of free space, and ϕ and ρ are the potential (e.g., one corresponding to the local vacuum level) and the charge density at position x, respectively. Accordingly, if a concentrated electrolyte is used and the specifically adsorbed species do not respond to potential change, the double layer on the solution side can be modeled as a parallel plate capacitor having the capacitance C_{dl} that follows the Helmholtz relation:

$$C_{\mathrm{dl}} = \frac{\varepsilon_s\varepsilon_0}{x_2} \tag{2.22}$$

where ε_s is the relative permittivity of the solvent, and x_2 is the distance of the OHP from the electrode surface. Assuming typical values of ε_s of ~10 and x_2 of ~1 nm, C_{dl} is predicted to be ~10 μF/cm^2.

Note that the existence of the double layer leads to non-Faradaic *double layer charging current*. Therefore, when an electrochemical system is investigated with potential step or sweep methods, this charging current, as well as the Faradaic reaction current caused by charge transfer across the electrode/electrolyte interface, should be taken into account. The double layer charging current can be eliminated at a steady state where the electrode potential is fixed.

2.5. Research Objectives

The central goal of this dissertation project is to (1) prepare *gate-tunable* 2D electrodes having FET-like structures, in which surface electronic structure can be modulated with the field effect, and (2) study how three representative interfacial electrochemical phenomena occurring at electrode/solution interfaces—(i) double layer charging, (ii) electron transfer across the interface, (iii) surface binding of redox species—are affected by the back gating. The reasons why our interest at this point is limited to only these interfacial phenomena are that (1) they often determine the overall reaction kinetics in many important electrochemical systems and (2) the electric field generated by the back gate would be completely screened outside the OHP due to the abundant mobile ions in the electrolyte.

To realize the proposed ideas, the working electrode should be sufficiently thin; otherwise, the electric field from the back gate would be canceled out in the space charge

layer within the electrode and thus would not change the electronic properties at the surface. Consider a gate-tunable ZnO electrode for example. Although the maximum thickness of space charge layer in a bulk ZnO spans up to a few micrometers (e.g., 1.7 μm for a typical n-doped ZnO with $N_d = 1 \times 10^{15}$ cm^{-3}), the maximum charge density in accumulation or inversion layer, in which electronic properties of the semiconductor show the most dramatic change, occurs just a few nanometers from the semiconductor-dielectric interface according to quantum mechanical calculations.[74,75] Therefore, an ultrathin (preferably, equal or thinner than ~5 nm) semiconductor layer needs to be prepared for the gate-induced charge to be fully accessible at the semiconductor surface.

A value of the gate-tunable electrodes lies in the fact that gating is basically an electrostatic charging process in which, in principle, no extra work is needed to maintain the charge induced in the electrode. Therefore, field effect modulation can be a potential means to improve energy efficiencies of electrochemical processes on 2D electrode surfaces. Furthermore, a gate-tunable electrode can serve an excellent research platform to study electrochemical interfaces in that the interfacial phenomena are continuously and reversibly controlled without changing chemistry of the system. This would allow systematic investigation of electrochemical interfaces while excluding chemical effects.

In this dissertation project, as initial investigations to prove the proposed concepts, relatively simple model systems that consist of a gate-tunable 2D semiconductor electrode and an electrolyte with (or without) outer-sphere redox species have been studied. In the following chapters, field effect modulation of EDL structures and outer-sphere charge transfer kinetics are demonstrated first, and possibilities and requirements to realize the

field effect modulation of surface binding and (photo)electrocatalytic activities are discussed in the last chapter.

3. Experimental

This chapter outlines the device structure, fabrication, and experimental techniques used in this dissertation project. Specific experimental details in sample preparations and measurements are described in the respective sections of the following chapters.

3.1. Gate-Tunable Electrodes: General Features and Issues

Figure 3.1 schematically shows the general device structure of the gate-tunable electrodes used in this project. Essentially, the device structure is analogous to a field-effect transistor made of an ultrathin or 2D semiconductor channel, though some of our devices have additional top structures designed for electrochemical studies. For convenience in device fabrications, a SiO_2/*p*-Si substrate was used as a back gate to induce the field effect to the device in this project; the thermally grown SiO_2 top layer serves as a gate dielectric while the highly doped *p*-Si bottom layer serves as a metallic gate electrode. The ultrathin or 2D semiconductor film is prepared on the substrate either by polymer-assisted film transfer or by atomic layer deposition techniques, which are discussed in more details in

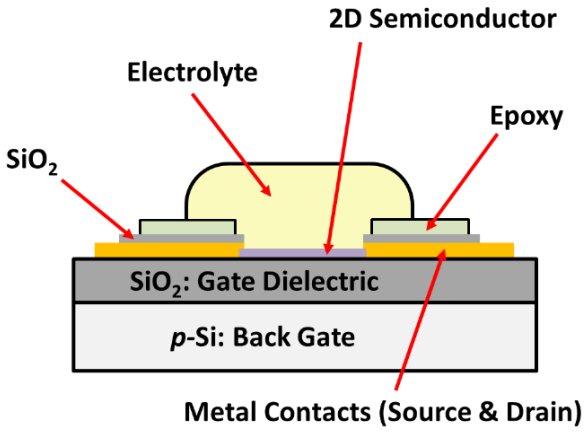

Figure 3.1. Schematic of device structure used in this project.

the following section. The *source* and the *drain* electrodes are prepared by photolithography process followed by electron beam evaporation of appropriate metallic sources. If the devices are used to investigate electrochemical reactions, additional passivation layers are coated on the metallic contacts (i.e., the source and the drain) to prevent charge transfer reaction on them; since we are interested in the electrochemistry on the semiconductor, the reaction current should be collected exclusively on the semiconductor surface for proper data interpretation. The passivation is achieved by evaporating 100 nm thick SiO_2 film on them and, in some cases, coating an additional polymer layer for better passivation.

Another critical issue that can arise when using gate-tunable electrodes to study electrochemical reaction is the in-plane polarization within the 2D semiconductor electrode. In a gate-tunable electrode, in order for an electrochemical reaction to occur at a certain site on the semiconductor surface, charge carriers should first move from the metal contacts to the site and then interact with active reaction species in the electrolyte. Therefore, there are three polarization sources that can potentially limit the overall reaction kinetics: (i) in-plane charge transport within the electrode, (ii) out-of-plane charge transfer to the electrolyte, and (iii) mass transport of redox species in the electrolyte. In contrast to a conventional working electrode, in which the active electrode material is prepared on a metallic current collector, there might be considerable in-plane polarization on gate-tunable electrodes because the active material is prepared on an insulating gate dielectric. This means the in-plane charge transport, rather than out-of-plane charge transfer or mass transport, can be potentially the limiting step that controls overall reaction rate on the

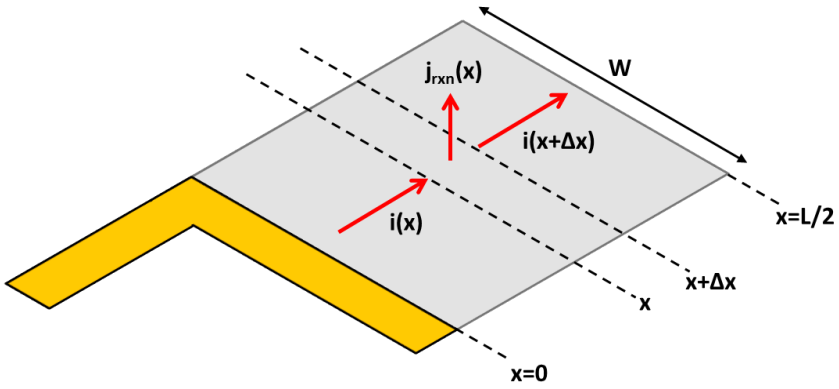

Figure 3.2. 1-D model of a gate-tunable electrode in redox-active electrolyte. Note that the distance between the two peripheral metal contacts is L but here we presented only half of the electrode assuming the electrode is symmetric with respect to x=L/2. W indicate the width of the electrode; i(x) indicate the in-plane current at position x; j_{rxn}(x) is reaction current density at position x.

electrode. Since the main objective of this project is to investigate how the field effect affects the interfacial reaction kinetics (i.e., out-of-plane processes), the gate-tunable electrodes should be designed to minimize the in-plane polarization.

To deduce the factors determining the in-plane polarization, a simple 1-D model shown in Figure 3.2 is used. The charge balance at location x is given by:

$$[i(x) - i(x + \Delta x)] - j_{rxn}(x)W\Delta x \tag{3.1}$$

where $i(x)$ is local in-plane current and $j_{rxn}(x)$ is local reaction current density at x. For $\Delta x \to 0$, we get:

$$\frac{\mathrm{d}i(x)}{\mathrm{d}x} + j_{rxn}(x)W = 0 \tag{3.2}$$

With the assumption that the polarization across the electrode is sufficiently small that j_{rxn}(x) is nearly constant over the electrode, the integration of equation 3.2 gives:

$$i(x) - i(0) = -W \int_0^x j_{\text{rxn}}(x)\, dx \approx -W j_{\text{rxn}} x \tag{3.3}$$

Using the boundary conditions, $i(0) = i_0$ and $i(L/2) = 0$, $i(x)$ is given by:

$$i(x) = i_0 \left(1 - \frac{2x}{L}\right) \qquad \text{where } i_0 = \frac{WLj_{\text{rxn}}}{2} \tag{3.4}$$

On the other hand, by Ohm's law, we get:

$$\mathrm{V}(x) - i(x)\rho_s \frac{\Delta x}{W} = V(x + \Delta x) \tag{3.5}$$

where ρ_s is the sheet resistance (Ω/sq) of the electrode. For $\Delta x \to 0$, we get:

$$\frac{\mathrm{d}V(x)}{\mathrm{d}x} + i(x)\frac{\rho_s}{W} = 0 \tag{3.6}$$

$$\mathrm{V}(L/2) - \mathrm{V}(0) = \frac{\rho_s}{W}\int_0^{\frac{L}{2}} i(x)\, dx = \frac{\rho_s}{W} i_0 \left(x - \frac{x^2}{L}\right)\Big|_0^{\frac{L}{2}} = \frac{\rho_s L}{4W} i_0 = \frac{\rho_s j_{\text{rxn}} L^2}{8} \tag{3.7}$$

Therefore, the in-plane polarization $\mathrm{V}(L/2) - \mathrm{V}(0)$ can be minimized by (i) using electrode materials with high carrier mobilities, (ii) reducing reaction current density on the electrode (e.g., by reducing the concentration of redox species), and (iii) reducing the distance between the two peripheral metal contacts. In this regard, the ideal gate-tunable electrode for electrochemical studies would be the device having a microelectrode made of semiconductor with high carrier mobilities. In the electrochemical measurements, the concentration of the reaction species can be adjusted to realize reasonably small in-plane polarization while obtaining sufficiently large reaction current signals.

3.2. Device Fabrication and Characterization

3.2.1. Preparation of 2D Semiconductor Electrodes

Graphene Electrodes. The graphene electrodes were prepared by transferring a commercial CVD graphene sample on Cu substrates to SiO_2/*p*-Si substrates with the method proposed by the Ruoff group[76] with a modified protocol described below. The transfer procedure is also schematically shown in Figure 3.3.

Graphene Transfer Procedure

1. Cut the CVD-grown graphene sample into an appropriate size (usually 1 cm x 1 cm)
2. Poly(methylmethacrylate) (PMMA) solution (20 mg/mL in chlorobenzene) was spin-coated on one side of the graphene sample at 3000 rpm for 30 s and baked at 180 ^oC on a hot plate for 5 min. The PMMA film prevents possible damages of the graphene layer in the rest of transfer process.
3. Since the CVD graphene is grown on both side of the Cu substrate, the graphene on the uncoated side is removed using O_2 plasma for 20 sec.

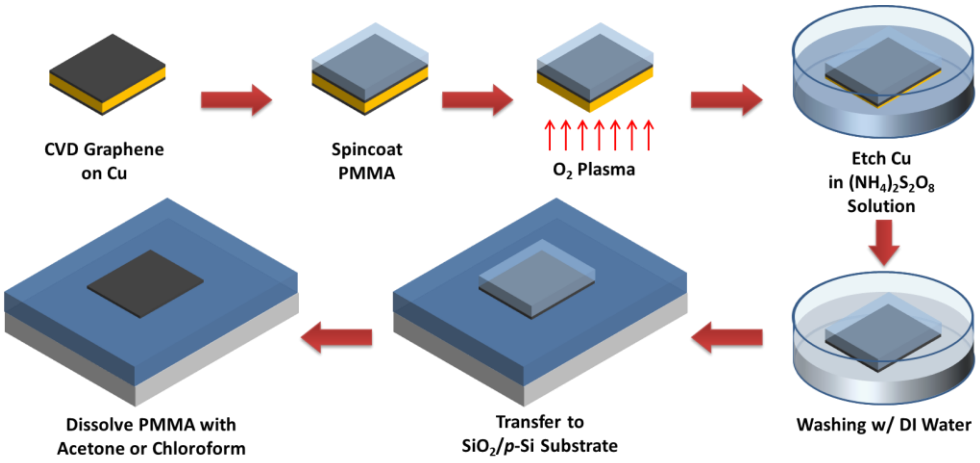

Figure 3.3. Schematic of PMMA-assisted graphene transfer to a SiO_2/*p*-Si substrate.

4. To etch the Cu substrate underneath the PMMA/graphene, the sample is floated on ammonium persulfate aqueous solution (0.1 g/mL) for 12 hrs.
5. After the Cu substrate is completely dissolved, the PMMA/graphene film is transferred to freshly deionized water bath so that it is floated on the surface and kept in the bath for 5 min. This step is repeated three times to thoroughly rinse the residual etchant solution on the sample.
6. The PMMA/graphene sample is transferred onto a SiO_2/*p*-Si and baked at 180 ^oC on a hot plate for 30 min. (Note: for graphene devices, the source and the drain are prepared on the substrate before the transfer process for more efficient device fabrications.)
7. The graphene-transferred substrate is immersed in acetone or chloroform for 1-3 hrs to remove the PMMA film.
8. The sample is rinsed with methanol and isopropyl alcohol, and dried for subsequent device fabrication steps.
9. After the device fabrication is completed, the sample is annealed at 130-300 ^oC in nitrogen atmosphere for 30 min before measurements.

The Raman spectra of the transferred graphene (Figure 3.4) were collected in a backscattering geometry using a confocal Raman spectrometer (Witec Alpha300R) with linearly polarized radiation at 514.5 nm from an Ar laser. The Raman spectra of CVD graphene show three characteristic peaks: the G peak (~1580 cm^{-1}), D peak (~1360 cm^{-1}), and 2D peak (~2700 cm^{-1}). The G peak corresponds to the E_{2g} phonon at the Brillouin zone center.[77] The D peak is due to breathing modes of sp^2 atoms and requires a defect for its activation.[77–79] The 2D peak is the second order D peak which is observed even when no D peak is present.[80,81] Monolayer graphene has a sharp, single 2D peak 2–4 times bigger than its G peak, which distinguishes it from multilayer graphene or graphite phases.[80,81]

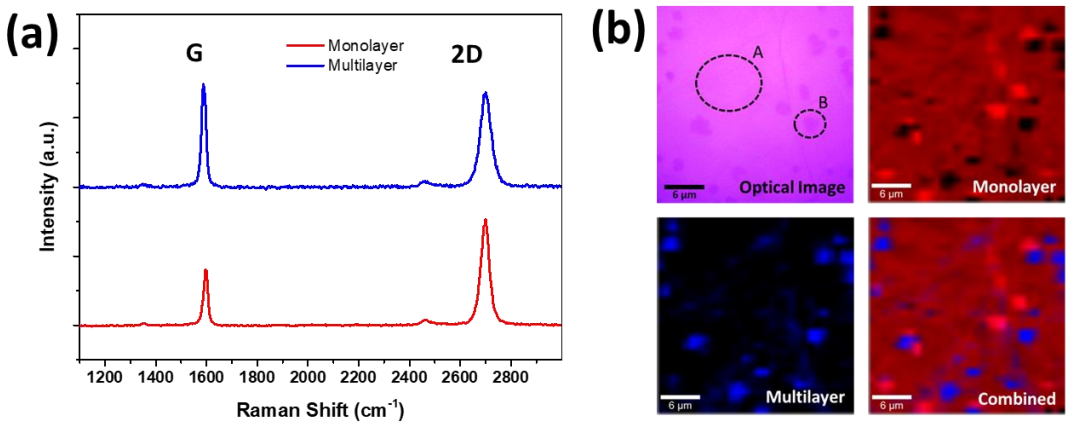

Figure 3.4. (a) The averaged Raman spectra of monolayer and multilayer graphene phases, which were obtained at the areas indicated as A and B in the optical image in (b). (b) The optical image and the corresponding spectral Raman map of CVD graphene that was transferred on a SiO_2/p-Si substrate. The red and blue spots indicate spectroscopically monolayer and multilayer phases, respectively.

To obtain the spectral Raman map, the Raman spectra obtained at each point were fit to the linear combination of the Raman spectra obtained from internal standard points. The areas with higher contrast in the optical image in Figure 3.4b, which are believed to be multilayer graphene phases, have either the *multilayer* spectrum or the *monolayer* spectrum with a stronger signal. The phases of the latter case are likely composed of loosely coupled monolayers with a different stacking order.[82] The Raman spectrum at each point could be deconvoluted into a linear combination of the average spectra of *monolayer* and *multilayer* spectra shown in Figure 3.4a. Optically clean graphene areas, which were used for subsequent measurements, did not show significant D peak (~1360 cm^{-1}). In our observation, the transferred CVD graphene consists of ~82% monolayer phase and ~18% multilayer islands with ~1-3 μm sizes.

ZnO Electrodes. ZnO films were grown on clean SiO_2/*p*-Si substrates using an ALD system (Savannah Series, Cambridge Nano Tech) with diethylzinc (DEZ) and water vapor as precursors which undergo the following reaction mechanism:

$$Zn(C_2H_5)_2^* + H_2O(g) \longrightarrow ZnO^* + 2C_2H_6(g)$$

where $*$ denotes a surface species. Since this reaction is quite exothermic, ZnO film can be grown at relatively low temperatures in the range of 100−200 °C. But the DEZ precursors have been successfully used even at room temperature and at temperatures as high as 600 °C.[83] The film growth condition used in this work is as follows:

ALD Film Growth Procedure

1. Clean up a SiO_2/*p*-Si wafer, on which the ZnO film is to be deposited, with isopropyl alcohol and dry it.
2. Load the wafer in the ALD chamber and pump down the chamber.
3. Set the temperature of the chamber at 235 °C and wait until the temperature is stabilized.
4. Set the flow rate of the carrier gas (N_2) to 20 sccm and wait for 60 sec.
5. Pulse water vapor for 15 ms and wait for 5 sec.
6. Pulse DEZ for 15 ms and wait for 5 sec.
7. Repeat step 5 and 6 for desired number of cycles.
8. Unload the wafer from the chamber.

The thickness of the ZnO films was measured using a variable angle spectroscopic ellipsometer (VASE, J.A. Woollam) with monochromatic polarized light (500-1100 nm in wavelength) at two different incident angles (60^o and 75^o). The obtained data was fitted to the Cauchy model,[84] which showed mean square error (MSE) of 0.01-0.33 $Å^2$ depending on the film thickness. The growth rate of ZnO films at the given condition was observed to

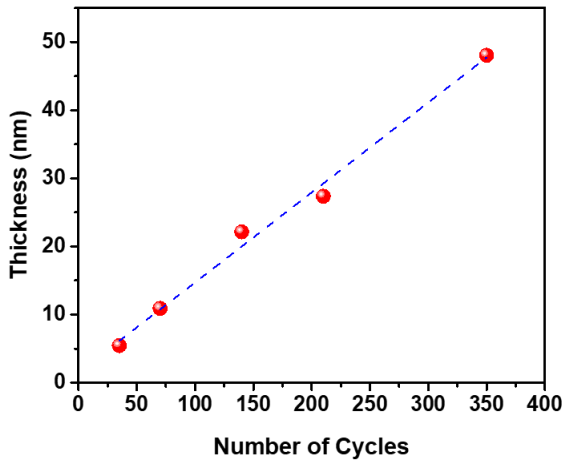

Figure 3.5. Thickness of ALD-grown ZnO films versus number of cycles.

be ~1.32 Å per cycle (Figure 3.5). Among the prepared ZnO/SiO_2/*p*-Si samples, we used the samples with ~5 nm and ~50 nm thick ZnO films to fabricate gate-tunable electrodes. Before device fabrication, the 5 nm and 50 nm samples were annealed in N_2 at 300 ^oC and in O_2 at 400 ^oC, respectively, for 10 min in a rapid thermal annealer (RTP-600S, Modular Process Technology). The 50 nm thick films were annealed under more oxidative condition than the 5 nm thick film because otherwise it behaved like a metal, rather than an n-type semiconductor, due to incomplete annealing of the thick ZnO layer. We observed no changes in thickness after the annealing processes.

3.2.2. Integration of Metal Contacts and Passivation Layers

Metal contacts and passivation layers are integrated on the prepared samples (i.e., the SiO_2/*p*-Si substrates with the semiconductor films on top) through a series of photolithography processes followed by etching or deposition steps. The procedure presented here is a general example, and specific details for different types of devices will

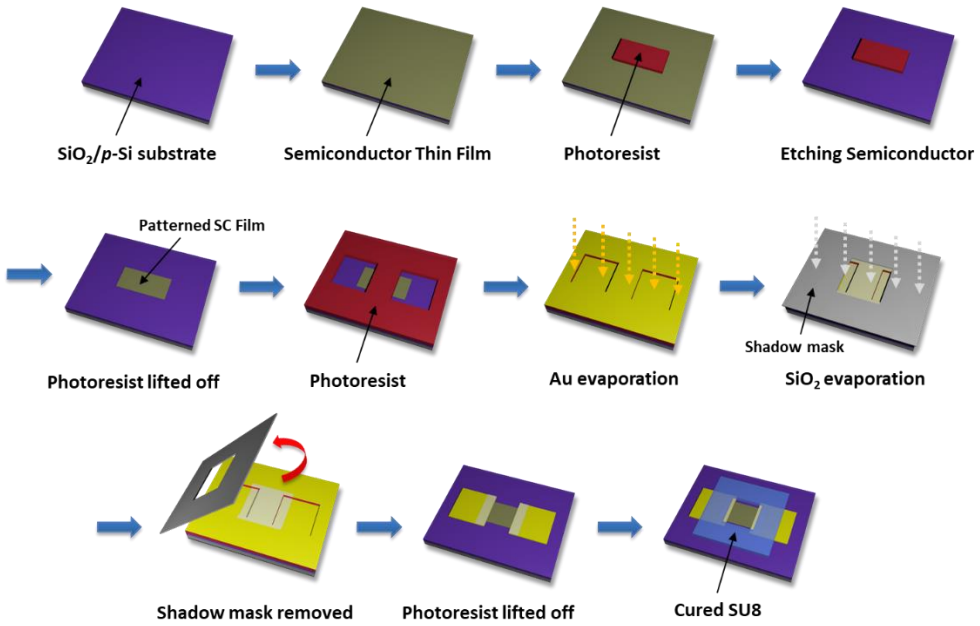

Figure 3.6. Device fabrication procedure of back-gated 2D electrodes (not to scale).

be described in the respective experimental sections in the following chapters. Figure 3.6 schematically shows the integration procedure and alignments between different layers.

Patterning Semiconductor Films. The semiconductor films on the substrates were patterned into a rectangular shape via photolithography. After preheating the samples at 105 ^{o}C for 1 min, the photoresist (Microposit S1813, Dow Electronic Materials) was spin-coated onto the wafer at 3000 rpm for 30 s. After soft baking at 105 °C for 1 min, we exposed the wafer to UV light (12 mW/cm^2) for 5 s through a photomask using contact mask aligner (MA6, SUSS MicroTec Inc.). The wafer was then baked at 105 °C for 1 min, developed in Shipley 351:H_2O=1:5 (v/v) solution for 20 s, and thoroughly rinsed with deionized water. The exposed semiconductor area was removed by oxygen plasma treatment (for graphene) or by wet etching with HCl solution (for ZnO).

Metal Contacts and Passivation Layers. Metal contacts to the patterned semiconductor electrodes were made via another photolithography process. After developing photoresist patterns on the wafers following the same procedure described above, 30 Å Ti and 300 Å Au layers were sequentially evaporated using an electron beam evaporator with the growth rate at 1 Å/s. For the ZnO devices to study electrochemical reactions, the surface of the metal contacts near the ZnO films were passivated by further evaporating 30 Å Ti and 1000 Å SiO_2 layers through a shadow mask (Figure 3.6) using another electron beam evaporator with the growth rate at 1 Å/s. In this way, we could achieve nearly perfect alignment between the metal and the passivation layers because a single photoresist pattern is used for both evaporation steps. This, in turn, makes the whole semiconductor area between the metal contacts is susceptible to both the back gate and the electrolyte in electrochemical measurements. After the evaporations steps, the photoresist was lifted off in acetone and the samples were sequentially sonicated in methanol and isopropyl alcohol baths.

For the devices fabricated for cyclic voltammetry study, epoxy-based cross-linkable photoresist (SU-8 2005, MicroChem) was coated on the samples so that the active semiconductor area was exposed through a slightly larger window. After preheating the samples at 120 ^{o}C for 1 min, the photoresist was spin-coated onto the samples at 3500 rpm for 30 s. After soft baking at 95 °C for 2 min, the photoresist film was exposed to UV light (12 mW/cm^2) for 9 s through a photomask. The exposed film was then baked at 95 °C for 3 min, and rinsed in developer solution (SU-8 developer, MicroChem) for 30 s. Finally, the film was cured at 120 °C for 15 min.

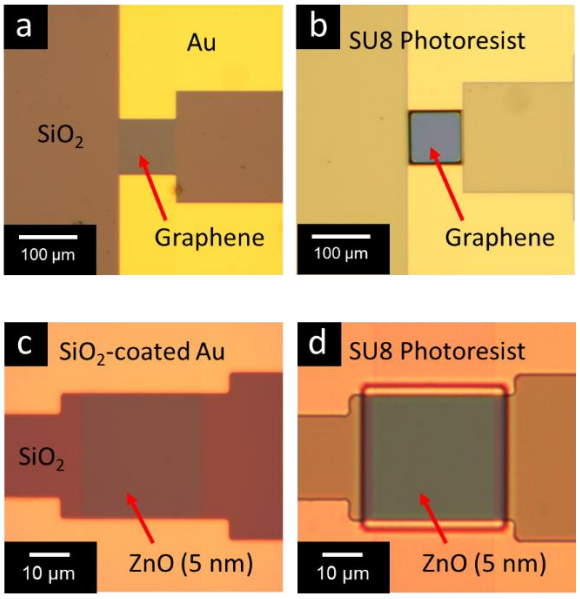

Figure 3.7. Top view of fabricated (a-b) graphene and (c-d) ZnO devices (a, c) before and (b, d) after transparent SU8 passivation layer is coated on top.

3.2.3. Charge Transport Characteristics of the Devices

Figure 3.8 shows the transfer curves of graphene and ZnO devices in back gating mode under N_2 atmosphere without electrolyte phase on them. The graphene device showed the expected ambipolar transport characteristics due to the lack of bandgap. The conductivity minimum (also referred to as "Dirac point") is initially at $V_{BG} =$ ~100 V but shifted to nearly zero bias after annealing the device at 300 °C in N_2 environment. The Dirac point shift occurs because p-dopants including oxygen, water vapor, and PMMA residue on graphene, which introduce holes in graphene, are removed during the annealing process. The annealed graphene device had mobility is ~1,200 $cm^2\ V^{-1}\ s^{-1}$ with on/off current ratio of ~5. In contrast, the ZnO devices showed typical n-type carrier transport characteristics with mobility of ~1.2 $cm^2\ V^{-1}\ s^{-1}$ and on/off current ratio of > 10^3.

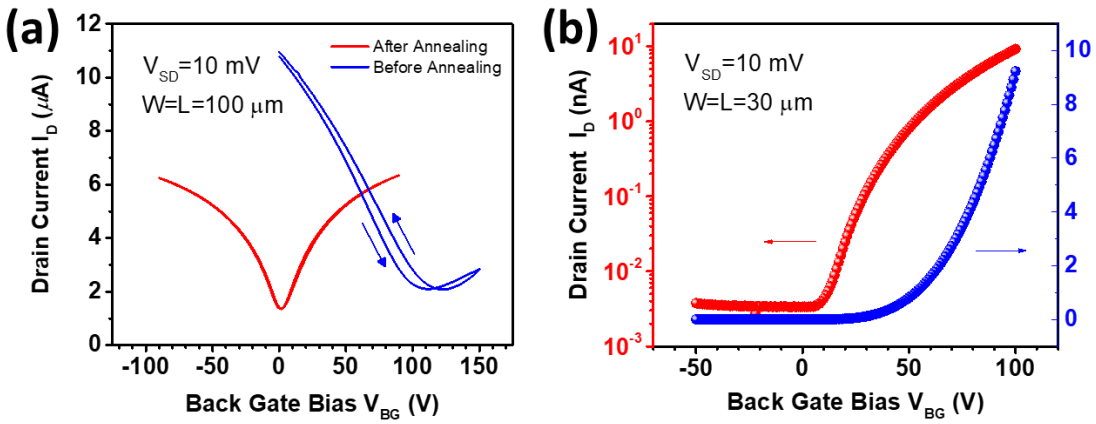

Figure 3.8. Transfer characteristics of the fabricated (a) graphene and (b) ZnO devices.

3.3. Instrumental Setup for Electrical Measurements

All electrical and electrochemical measurements of gate-tunable electrodes were performed at room temperature using multiple source-meters and high impedance electrometers (Keithley 2612, 2611B, 236, 237, and 6517A were used in this study) with a probe station. The general electrical configuration used in this project is illustrated in Figure 3.9. Note that the operational amplifier shown in the configuration essentially represent a potentiostat. The voltage bias applied to V_{SD} is typically 0 V or very small value (1-10 mV) so the potential distribution within semiconductor electrode is minimized during electrochemical measurements. The reaction current at the active semiconductor area is obtained from a sum of i_S and i_D (*i.e.*, $i_{rxn} = i_S + i_D$).

With the proposed configuration, simultaneous measurements of reaction current and in-plane polarization on the active semiconductor electrode can be achieved. To experimentally determine the in-plane polarization during electrochemical measurements, the electrode/electrolyte interface is modeled as the simplified equivalent circuit shown in

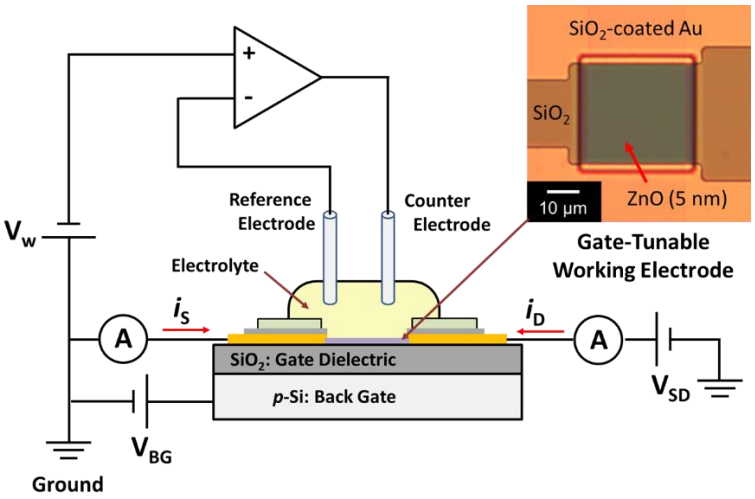

Figure 3.9. Cross-sectional view of a gate-tunable working electrode with the electrical configuration used in this study. The optical image on the right side shows a 5 nm thick ZnO electrode exposed through an epoxy window.

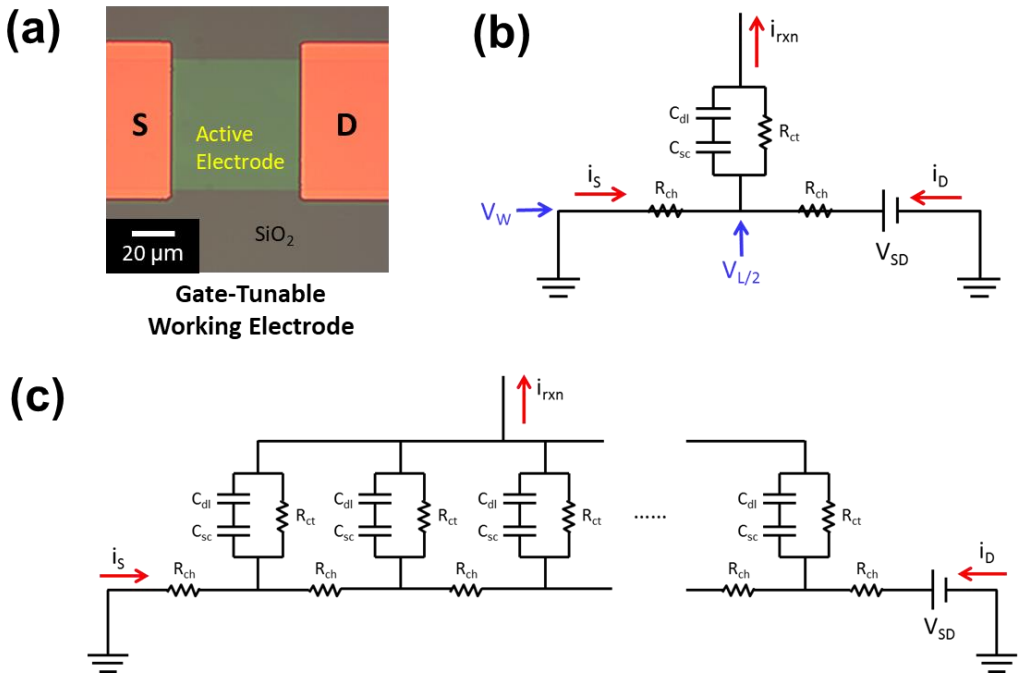

Figure 3.10. (a) Top view of the gate-tunable electrode, which is modeled as (b) simplified and (c) actual equivalent circuits to represent electrode/electrolyte interface of a back-gated electrode. The symbols C_{dl}, C_{sc}, R_{ct}, and R_{ch} on the circuits indicate the double layer capacitance, the space charge capacitance (for 2D semiconductor, C_{sc} is replaced with the quantum capacitance C_Q), the charge transfer resistance, and the channel resistance on the electrode, respectively.

Figure 3.10b; although the electrode can be more accurately modeled with an infinite ladder circuit (Figure 3.10c), it is not possible to determine the voltages and currents at infinite number of nodes in the circuit from i_S, i_D, and V_{SD} only. By applying the Kirchhoff's laws to the simplified circuit, the following relations are obtained.

$$i_{rxn} = i_S + i_D \tag{3.8}$$

$$\frac{V_{SD}}{i_D - i_S} = R_{ch} = \frac{L}{2\sigma_s W} \tag{3.9}$$

$$V_{L/2} - V_W = -i_S R_{ch} = -\frac{i_S V_{SD}}{i_D - i_S} \tag{3.10}$$

where L and W indicate the length and the width of the active semiconductor area, i_{rxn} is the reaction current, and σ_s is the sheet conductance of the semiconductor channel. The term $V_{L/2} - V_W$ indicate the maximum in-plane polarization, which occurs at the center of the active electrode as shown in Section 3.1.

Figure 3.11 shows the actual electrical connection to the source-meters used for the measurements, which realizes the electrical configuration shown in Figure 3.10. Note that the source-meter B is operated in 4-wire remote sensing mode in order for the working electrode potential V_w is applied with respect to the reference potential while the reaction current flows between the working and the counter electrode; this is exactly how the operational amplifier (or the potentiostat) presented in Figure 3.10 is supposed to work. In the measurements without electrolyte phase, the instrument B is not connected to any electrodes, so the device works as a regular field-effect transistor. The operation and data

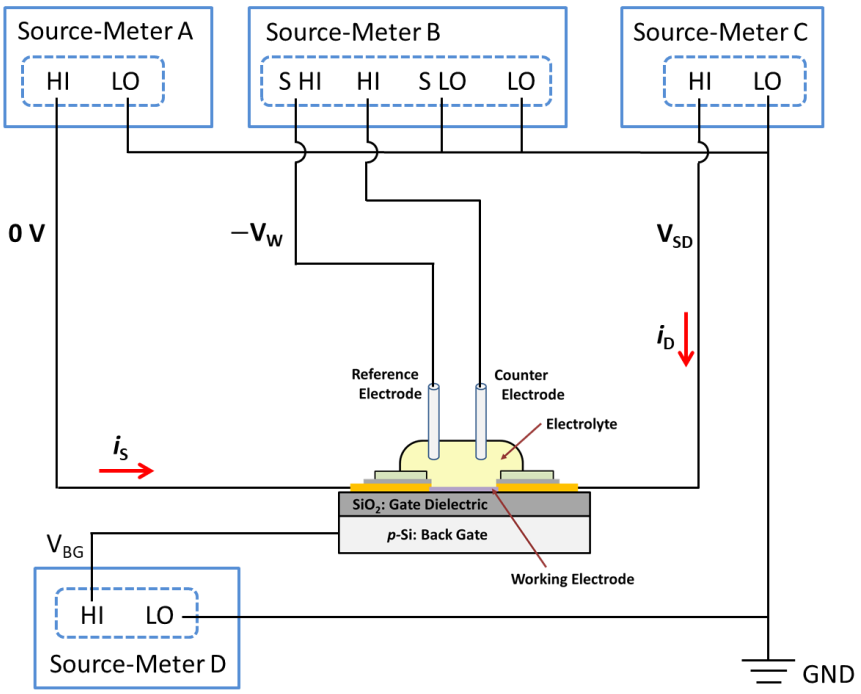

Figure 3.11. Schematic of electrical connections of source-meters to an electrochemical cell used in this study. Note that the instrument B is operated in 4-wires remote sensing mode while the other channels are operated in 2-wires local sensing mode.

acquisition of the instruments were done with scripts running on the TSP program provided by Keithley or with in-house LabVIEW programs.

3.4. Cyclic Voltammetry

Cyclic voltammetry (CV) is a powerful electrochemical analysis technique which is typically applied for initial investigations of electrochemical systems. In CV, the working electrode potential ramps linearly with time in cyclical phases, and the obtained data are plotted as the current versus the working electrode potential. Although a cyclic voltammogram typically has a complicate wave form primarily due to the transient concentration profiles of reaction species near the working electrode, it provides some important information to figure out the nature of the electrochemical system. First of all,

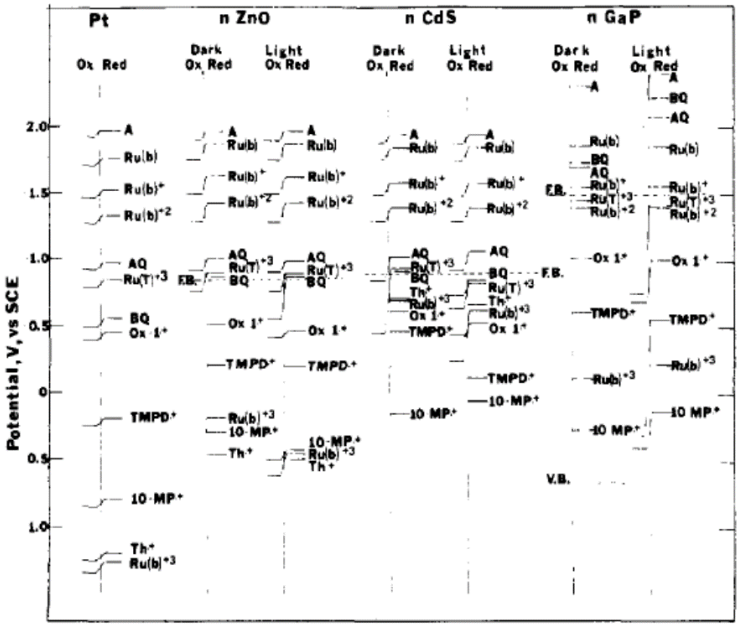

Figure 3.12. The reduction and reoxidation peak potentials for different redox species on a Pt disk electrode and on the three semiconductor electrodes in the dark and illuminated with white light. F.B denotes flat band potential of the electrode. [Reproduced with permission from ref. 85; Copyright 1977 by the American Chemical Society]

the peak potentials and peak currents in a cyclic voltammogram indicate whether a reaction species is active (i.e., can be oxidized or reduced) at a certain electrode potential range. In some cases, CV can also be used to identify the kinetic nature of the reaction; Nicholson's method[86] is an example that estimates the kinetic parameter k^0 of quasi-reversible reversible redox system from the peak separation.

It is noteworthy to mention the research reported by Kohl and Bard,[85] in which the flat band potentials V_{fb} (i.e., band edge positions) of n-type semiconductor electrodes were determined from CV data of various redox couples. Figure 3.12 summarizes the reduction and oxidation peak potentials of the redox couples on platinum and the n-type semiconductors. To put reactions on n-ZnO as an example, the redox couples are categorized into three different types according to the potential regions. The first type, of

which formal potential is more negative than V_{fb} such as $Ru(bpy)_3^{2+}$, shows similar reversible CV behaviors on Pt and n-ZnO; i.e., the n-ZnO essentially behaves like a metal, because the accumulation layer is formed at the electrode surface in the potential regime. The second type, of which the formal potential lies at or somewhat positive of V_{fb} such as BQ, shows a reversible behavior on Pt, but shows only an irreversible reduction at ZnO with the foot of the cathodic wave shifted almost to V_{fb}. Under illumination, oxidation peak of BQ due to photooxidation is observed. The third type, of which the formal potential is far more positive than V_{fb} such as Th^+, reversibly reduced on platinum but only shows an irreversible reduction peak on ZnO at a very negatively shifted potential. Similarly, electronic and electrochemical nature of gate-tunable ZnO electrodes were investigated using different redox couples in CV experiments in this project.

3.5. Steady-State Analysis in Microchannel Flow Cells

Although CV gives some valuable information about electrochemical systems, it is basically a qualitative (or semi-quantitative) method that is sometimes inappropriate to study reaction kinetics. Hydrodynamic methods such as rotating electrode techniques (i.e., RDE and RRDE), which can generate a steady-state condition in the electrochemical system, have been proven more useful for such a quantitative analysis. Unfortunately, the unique structure of gate-tunable electrodes somewhat prohibits the usage of the rotating electrode techniques, which are the most popular hydrodynamic methods, in this project. Therefore, we integrated our gate-tunable electrodes into microfluidic flow cells for steady-state analysis; the forced convection in the microfluidic channel enhances mass transport and generates a time-invariant concentration profiles near the working electrode.

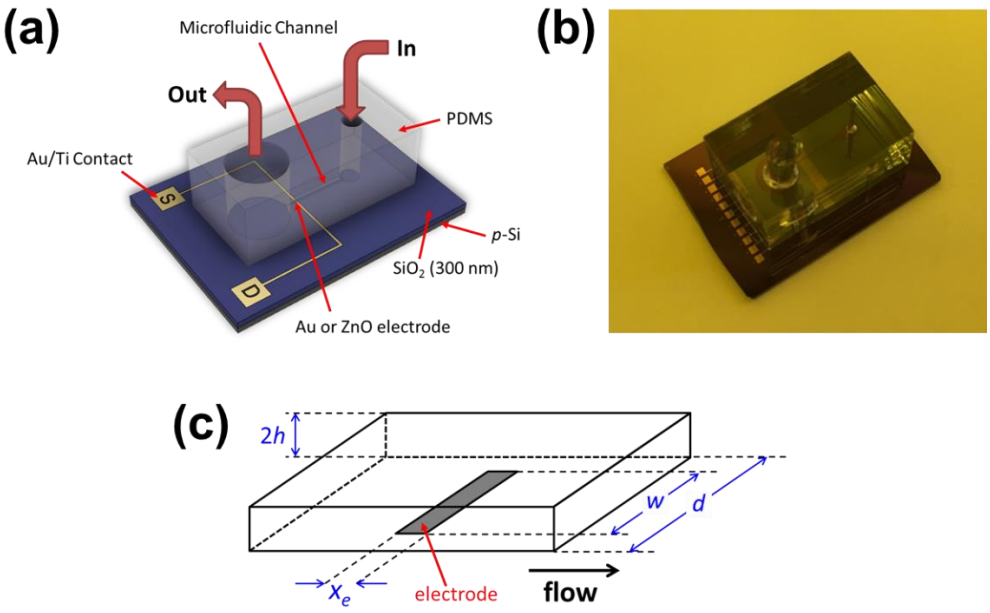

Figure 3.13. (a) Structure of the gate-tunable electrochemical flow cell with Au or ZnO electrode. (b) Photography of a fabricated device. (c) Geometry of microfluidic channel (width d and height $2h$) and active electrode area (length x_e and width w).

Device Structure. Figure 3.13 shows the structure of the flow cell. A flow cell is made by integrating PDMS microfluidic channel on a gate-tunable electrode. The PDMS microfluidic channel is made by replicating a master mold prepared by photolithography processes with PDMS precursors. The integration of PDMS and the SiO_2 substrate is achieved by plasma treatment followed by thermal annealing. The detailed device fabrication procedure is described in the respective experimental section in the Chapter 6.

Mathematical Model. Due to the structural similarity of the flow channel, the electrochemical and the hydrodynamic behaviors of our flow cells can be described by the mathematical model reported previously.[87,88] This model was developed for quasi-reversible redox reaction in a "high-speed channel flow cell". This model deals with an electrochemical reaction with the form: $\mathrm{Ox} + e \rightleftarrows \mathrm{Red}$, where both oxidized (Ox) and

reduced (Red) species are kinetically stable on the timescale of the experiment, and the bulk solution contains only Ox before it enters the flow cell. The analytical solution for the steady-state voltammogram (i.e., *I vs U*) is given by:

$$\frac{I}{I_{\mathrm{rev}}} = 1 - 2u + 2u^2 \ln(1 + u^{-1}) \tag{3.11}$$

$$\mathrm{u} = \frac{0.6783\ {D_{\mathrm{red}}}^{2/3}(3V_f/4dx_e h^2)^{1/3}}{k_b + (D_{\mathrm{ox}}/D_{\mathrm{red}})^{2/3}k_f} \tag{3.12}$$

$$I_{\mathrm{rev}} = -\frac{0.925Fwc_{\mathrm{ox}}{}^{*}(x_e D_{\mathrm{ox}})^{2/3}(h^2 d)^{-1/3}\ {V_f}^{1/3}}{1 + (D_{\mathrm{ox}}/D_{\mathrm{red}})^{2/3}(k_b/k_f)} \tag{3.13}$$

where k_f and k_b are the rate constants (cm/s) for forward and backward reactions which are functions of the electrode potential U, $c_{\mathrm{ox}}{}^{*}$ is the bulk concentration of Ox in the feed solution, D_{i} is diffusion constant of i, V_f is volumetric flow rate of the feed solution, F is the Faraday constant, and the other terms represent the geometrical parameters given in Figure 1b. When k_f is sufficiently large compared to k_b, I reaches a limiting current I_{lim} given by the Levich equation:

$$I_{lim} = -0.925Fwc_{\mathrm{ox}}{}^{*}(x_e D_{\mathrm{ox}})^{\frac{2}{3}}\left(\frac{V_f}{h^2 d}\right)^{\frac{1}{3}} \tag{3.14}$$

In such a mass transport limiting condition, charge transfer at the electrode/electrolyte interface is so fast that the surface concentration c_{ox} of Ox becomes zero and the overall reaction rate is essentially limited by the mass transport rate of Ox through the *diffusion layer* formed near the electrode; i.e., mass transport becomes the rate determining step (RDS).

Note that the analytical solutions in equations 3.11 to 3.14, are valid for a laminar flow with a negligible horizontal diffusion effect (i.e., the Reynolds number $Re = \frac{V_f}{h\nu} <$ 2500, where ν is the kinematic viscosity of the feed solution, and the Peclet number $Pe = \frac{3V_f x_e^2}{2dD_{ox}h^2} > 10^3$).

Correction of Mass Transport Effect. Under the forced convection with a fixed V_f, it can be assumed that a stagnant *diffusion layer* of thickness δ_{ox} forms at the electrode surface where the solution velocity is zero at y=0 and the concentration of Ox is maintained at $c_{\mathrm{ox}}{}^*$ beyond y= δ_{ox}. If the forward reaction dominates (i.e., the situation where sufficiently negative potential is applied to the working electrode), the mass transport rate of Ox should be the same as the reduction rate at the working electrode surface in a steady-state. Therefore, the reduction rate of Ox is given by:

$$-\frac{j}{F} = \frac{D_{\mathrm{ox}}}{\delta_{\mathrm{ox}}}(c_{\mathrm{ox}}{}^* - c_{\mathrm{ox}}) \tag{3.15}$$

where j is the current density and c_{ox} is the concentration of Ox at the electrode surface. Here, the mass transport via migration is assumed to be negligible because the total ionic concentration of the electrolyte sufficiently high in all measurement conditions. The current density j is maximized when c_{ox} becomes zero and thus the mass transport becomes the RDS. Once such a mass transport limiting condition is attained, j does not further increase even if a more negative electrode potential V_w is applied. Therefore, the limiting current density j_{lim} is given by:

$$-\frac{j_{lim}}{F} = \frac{D_{\mathrm{ox}}}{\delta_{\mathrm{ox}}} c_{\mathrm{ox}}{}^{*} \tag{3.16}$$

Considering $j = -k_f c_{\mathrm{ox}}$, combination of the equations 3.15 and 3.16 gives the following Koutecký-Levich equation:

$$j_{\mathrm{k}} = -k_f c_{\mathrm{ox}}{}^{*} = \left(\frac{1}{j} - \frac{1}{j_{lim}}\right)^{-1} \tag{3.17}$$

Note that the mass-transport-corrected current density $j_{\mathrm{k}} = -k_f c_{\mathrm{ox}}{}^{*}$ represents the reaction current density without the mass transport effect (i.e., the situation when the mass transport rate of Ox is extremely fast that c_{ox} equals to c_{ox}^{*}).

In the derivation using this diffusion layer model, it is assumed that the mass transport coefficient ($D_{\mathrm{ox}}/\delta_{\mathrm{ox}}$) is constant at a given V_f. To check the validity of this assumption and the correction method, we compared $j_{\mathrm{k}} = \left(\frac{1}{j} - \frac{1}{j_{lim}}\right)^{-1}$, where j and j_{lim} are calculated with the analytical solution (equations 3.11 to 3.14), with $j_{\mathrm{ideal}} = -ek_f c_{\mathrm{ox}}^{*}$ for various k_f values. For the calculation, parameters for our experimental conditions [$k_b = 0$ cm/s (i.e., a totally irreversible reaction was assumed), $D_{\mathrm{ox}} = D_{\mathrm{red}} = 1.4 \times 10^{-5}$ cm^2/s, $c_{\mathrm{ox}}{}^{*} = 2$ mM, $V_f = 10$ μL/min], and the geometrical parameters given for our flow cell design were used. Figure 3.14a shows (i) the j_{k} as a function of k_f compared to (ii) the corresponding ideal current density without mass transport effect j_{ideal} in a log-log plot. Although j_{k} and j_{ideal} quite well match to each other in a wide range of kinetic constant k_f ranging from 10^{-6} to 10^{4} cm/s, it is found that the diffusion layer model can introduce up to ~25% deviation of j_{k} from j_{ideal} in a severe mass transport limiting condition (i.e., high

k_f regime in Figure 3.14b), because the assumption of linear diffusion layer no longer holds in such a limiting condition.

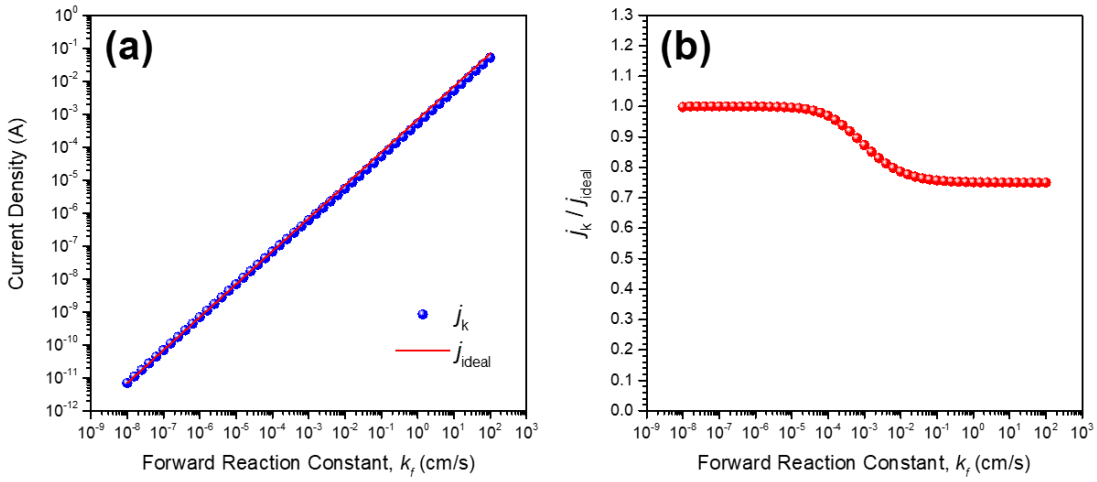

Figure 3.14. Comparion of j_{k} and j_{ideal} at different values of k_f: (a) j_{k} and j_{ideal} versus k_f. (b) $j_{\mathrm{k}}/j_{\mathrm{ideal}}$ versus k_f.

4. Electrochemical Behaviors of Graphene Transistors with Dual Electrochemical and Field-Effect Gates*

4.1. Abstract

As the first step to identify how the field effect affects the electrode/electrolyte interfaces, we here report an investigation of graphene field-effect transistors (G-FETs) in which the graphene channel is in contact with an electrolyte phase. The electrolyte allows direct measurement of graphene's Fermi level versus a reference electrode also in contact with the electrolyte. In addition, the electrolyte can be used to gate the graphene, i.e., a dual gate structure is realized. We employed this electrolyte-modified G-FET architecture to (1) track the Fermi level of the graphene channel while changing the gating condition; (2) determine the density of states (i.e., the quantum capacitance C_{Q}) of graphene; and (3) experimentally separate the *band filling potential* δ from the *double layer charging potential* $\Delta\phi_{\mathrm{EDL}}$. Additionally, we were able to determine the capacitance C_{EDL} of the electric double layer at the graphene/electrolyte interface, which is ~5 μF/cm^2, the same order of magnitude as C_{Q}. Overall, the electrolyte modified G-FETs provide an excellent model system for probing the electronic structure and transport properties of graphene and for understanding the differences between the two gating mechanisms.

4.2. Introduction

Graphene is a stable, atomically thin sheet of carbon atoms with the sp^2-hybridized honeycomb crystal structure. Since the field-effect on monolayer graphene was first

* Reproduced in part with permission from Kim, C.; Frisbie, C. D. *J. Phys. Chem. C* **2014**, *118*, 21160. Copyright 2014 by the American Chemical Society

demonstrated by Novoselov et al.[89,90] in 2004, graphene has received great attention in the scientific research community for its fascinating electrical,[30,91,92] electrochemical,[93–95] mechanical,[96] and optical[92,97] properties. In momentum space, graphene has symmetric cone-shaped conduction and valence bands in the low energy regime which touch at six corners of the Brillouin zone—the Dirac points. In other words, graphene is a zero bandgap semiconductor (or semi-metal) having linear energy dispersion and linear density of states (DOS) around the Fermi level.

One of most extensively studied graphene-based devices is graphene field-effect transistor (G-FET), in which the conductance of the graphene channel between the two metal contacts (the source and drain, respectively) is controlled by the voltage applied to the gate. Like transistors made of conventional semiconductors, the gate control enables a G-FET to be used as an electronic switch for digital logic devices and analog amplifiers.[98–101] In particular, the high carrier mobilities of graphene (up to ~10^5 cm^2 V^{-1} s^{-1} near room temperature for suspended graphene[102]) makes it a potentially attractive material for next-generation, high-frequency switching devices. A G-FET is also a useful component for physical, chemical, and biological sensor applications. Because all carbon atoms in a graphene sheet are surface atoms, carrier transport in a G-FET is highly sensitive to environmental conditions (*e.g.*, pH,[103–106] ionic concentration,[107–109] gas concentration,[110–113] flow rate,[114,115] and binding of biomolecules such as proteins[116,117] or DNAs[118,119]).

Most G-FET based devices are fabricated with either a back gate or a top gate configuration, in which the gate is located (1) on the back side of a dielectric layer supporting the graphene or (2) on top of a dielectric layer deposited on the graphene,

respectively. An electrolyte gate configuration, in which the top gate is a metal electrode immersed in an ionic solution covering the top of the graphene channel, has been employed in several G-FET applications, such as sensors operating in liquid or solid electrolyte solutions.[103–109,111,114–122] In an electrolyte-gated G-FET, the electrons or holes induced in the polarized graphene channel are compensated with counter ions packed at the graphene/electrolyte interface. This interfacial structure, referred to as an electric double-layer (EDL), is usually a few nanometers thick and consequently the gate capacitance can be as large as ~10−20 μF/cm^2, which is 1−2 orders higher than that can be achieved with oxide dielectrics.[123] Therefore, electrolyte gating is especially useful when high charge carrier accumulation (up to ~10^{13}-10^{14} cm^{-2}) and low voltage operation (<5 V) are needed.[11,124,125] Because of its atomically thin nature, graphene also can be gated simultaneously from two sides. The dual gate configuration provides an important platform for understanding electrical and optical properties of graphene such as electric field induced bandgap opening[126–130] and the Quantum Hall effect.[131–134]

In this study, we have investigated dual-gated G-FETs with a back and electrolyte gate configuration (Figure 4.1). The introduction of the ion gel (electrolyte) phase has an important advantage for fundamental measurements—the Fermi level position E_F of the graphene channel can be directly tracked by measuring its electrochemical potential with respect to a (quasi-)reference electrode. Tracking E_F using the reference electrode while sweeping the back gate bias gives the potential δ required to fill the energy band of graphene with charge carriers (*i.e.*, electrons or holes). In turn, the quantum capacitance

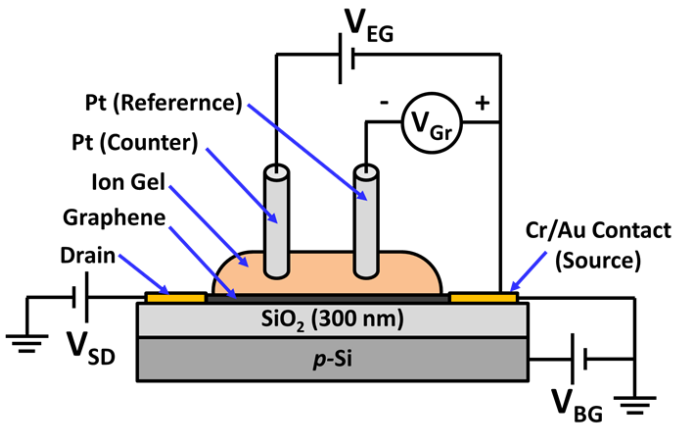

Figure 4.1. Cross-sectional view of a G-FET device with electrical/electrochemical configuration used in this study.

C_Q (*i.e.*, the DOS) of graphene can be estimated from this information. Such direct measurements of δ and C_Q are difficult, if not impossible, with dual-gated transistors using conventional oxide gates or electrolyte-gated transistors having only a single gate, because in these systems there is no good method for measuring the channel E_F while independently controlling carrier density.[135–137] Furthermore, the potential $\Delta\phi_{EDL}$ associated with the double layer charging at the graphene/electrolyte interface can be separated conveniently from δ by comparing the reference electrode potential in back gating mode to that in electrolyte gating mode, in which the counter electrode and the electrolyte are employed as a gate. Thus, as we will show, our dual-gated devices allow systematic determination of four parameters — δ, C_Q, $\Delta\phi_{EDL}$, and double layer capacitance C_{EDL} — at graphene/electrolyte interfaces. The dual-gated devices are generally useful testbeds for understanding carrier transport and electronic structure, and the approaches we follow here should also be applicable for investigating other 2D materials such as MoS_2 and ultrathin layers of conventional semiconductors.

4.3. Materials and Methods

Materials. Highly p-doped silicon wafers with thermally grown 300 nm-thick SiO_2 on top (SiO_2/*p*-Si wafers) were purchased from Silicon Valley Microelectronics (Santa Clara, CA) and used as back gates for G-FETs. Monolayer CVD graphene grown on Cu foil was purchased from Graphene Supermarket (Calverton, NY). Poly(methylmethacrylate) (PMMA, molecular weight: 350 kDa) and ammonium persulfate were purchased from Sigma-Aldrich (St. Louis, MO). The ionic liquid 1-ethyl-3-methylimidazolium bis-(trifluoromethylsulfonyl)amide ([EMI][TFSA]) was purchased from EMD Chemicals (Gibbstown, NJ). Poly(styrene-*b*-methyl methacrylate-*b*-styrene) triblock copolymer [SMS(15-81-15), the numbers in parentheses denote the block molecular weights in kDa] was synthesized via two-step atom-transfer radical polymerization[138] by Dr. Keun Hyung Lee. All organic solvents, including chloroform, ethyl acetate, chlorobenzene, were purchased from Sigma-Aldrich and used as received.

Fabrication of Graphene FETs. Metal pads for source and drain contacts were prepared using photolithography. An electron-beam evaporator was used to deposit a 30 Å Cr adhesion layer and 300 Å Au on top of SiO_2/*p*-Si substrates. G-FETs were prepared by transferring CVD graphene to the Au patterned SiO_2/*p*-Si substrate. The detailed procedure for graphene transfer used in this study is described in Section 3.2.1. The transferred graphene was patterned by mechanical scratching so the width and the length of the channel became 365 μm and 700 μm, respectively.

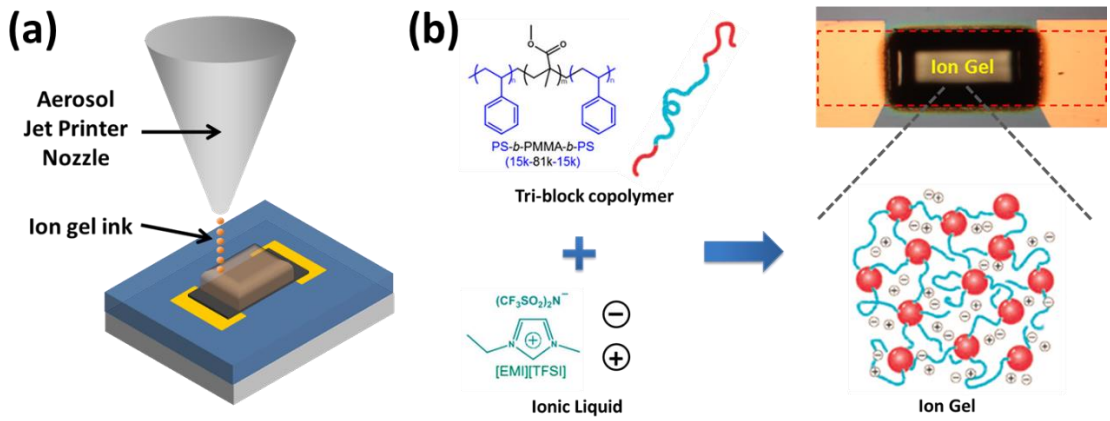

Figure 4.2. (a) Aerosol jet printing of ion gel on the graphene channel. (b) Schematic illustration of the ion gel formed by self-assembly of an ABA tri-block copolymer with insoluble A blocks and soluble B block in an ionic liquid. + and – symbols correspond to cation and anion, respectively. The optical image shows a G-FET device printed with the ion gel.

Printing Ion Gel on Graphene Channel. Ion gel printing was performed using a commercially available aerosol-jet printing system (Optomec AJ200). The ion gel ink was prepared by dissolving 9 wt % of [EMI][TFSA] and 1 wt % of SMS(15-81-15) in 90 wt % of ethyl acetate. The flow rates of carrier and sheath gas (N_2, 99.998%) were 15 standard cubic centimeters per minute (sccm) and 25 sccm, respectively. The ink was atomized into aerosol mist by ultrasonication at 15 ^oC and transported by the carrier gas into a print nozzle with a 150 μm diameter opening. The ion gel was printed to cover the graphene channel but not to touch the source and drain electrodes while the substrate was heated at 60 ^oC in air to enhance solvent drying. Since the ion gel does not flow at room temperature thanks to its *physically crosslinked* nature (Figure 4.2b), it can be applied on the graphene channel without a reservoir to hold the electrolyte phase. Therefore, the ion gel allows one to avoid further photolithography and/or epoxy coating processes which isolate metal contacts from the electrolyte but potentially contaminate or damage the graphene channel. The ion gel

coated G-FETs were annealed at 130 ^{o}C on a hot plate in a N_2-filled glovebox for 30 min before electrical and electrochemical measurements.

Electrical and Electrochemical Measurements. All electrical and electrochemical measurements were performed at room temperature in a N_2-filled glovebox. The electrical configuration used in this work is illustrated in Figure 4.1. The current-voltage characteristics of the G-FETs were measured by connecting a two-channel source meter (Keithley 2612A) to source, drain and back gate electrodes. In ion gel coated G-FETs, a high impedance electrometer (Keithley 6517A) was connected to the quasi-reference electrode (Pt wire, 100 μm in diameter) immersed in the ion gel to measure the electrochemical potential of the graphene channel. Electrolyte gating was performed by applying voltage to the counter electrode (another Pt wire, 100 μm in diameter) immersed in the ion gel using a source meter (Keithley 237).

4.4. Results and Discussions

Effect of Ion Gel Printing on Back Gate Capacitance and Carrier Transport in G-FETs. Figure 4.3a shows the transfer curves (I_{SD}–V_{BG}) of a G-FET at a source-to-drain bias $V_{SD} = 10$ mV, which were obtained before and after ion gel printing. Before printing ion gel, the Dirac point ($V_{BG,Dirac}$), the potential at which the total charge carrier density and the conductivity of the graphene channel are minimized, was observed at $V_{BG} = 88$ V. This indicates the graphene channel was initially in a highly p-doped state; the Dirac point is determined as $V_{BG,Dirac} = e\bar{n}/C_{ox}$ where e is the charge of a single electron, $\bar{n}$ is the carrier density induced by doping,[139–141] and C_{ox} is the back gate

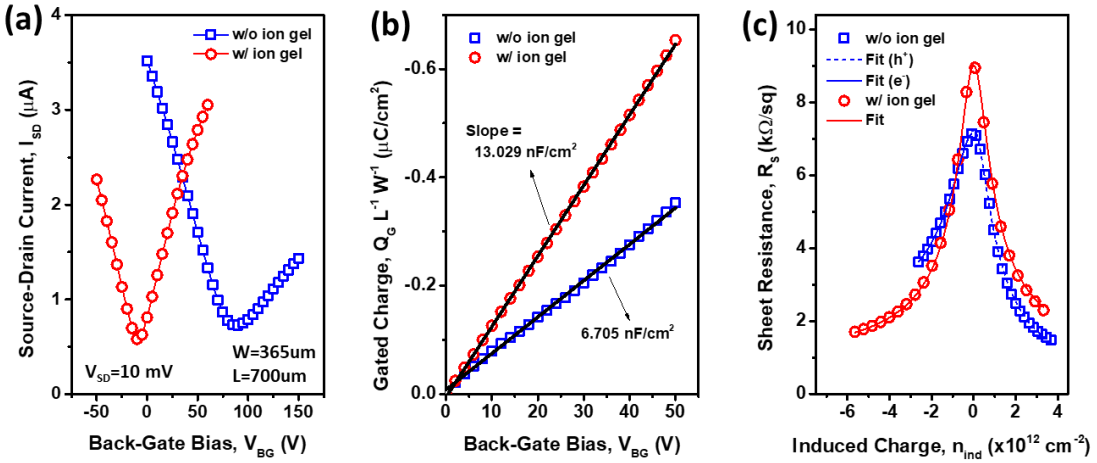

Figure 4.3. Charge transport characteristics of G-FETs before and after ion gel printing. (a) Back-gate transfer curves (I_{SD}–V_{BG}) obtained at V_{SD}=10 mV and dV_{BG}/dt = 29.5 V/s. (b) Back-gate-induced charge densities on the graphene channel at different V_{BG}, which were obtained by integrating the displacement current (I_{BG}) at dV_{BG}/dt = 5.66 V/s. (c) Sheet resistances of graphene channel as a function of induced carrier density n_{ind}. The lines in (c) indicate the result of curve fitting.

capacitance per unit area, respectively. Such highly positive $V_{BG,Dirac}$ have been typically observed in G-FETs that are made of CVD graphene transferred on SiO_2 substrate and not annealed under forming gas ($H_2 + N_2$) or vacuum condition before the measurements.[142,143] Possible p-dopants in our devices include charged impurities trapped on the SiO_2 substrate,[144–147] ambient molecules adsorbed on the graphene surface,[112,113] and PMMA residues.[148] After printing the ion gel on the graphene channel, however, we observed the Dirac point shifted to near zero gate bias ($V_{BG} = -9.3$ V). This behavior has been observed in G-FETs covered with a dielectric medium[141,149] or ionic solution,[150,151] which can effectively screen charged impurities on graphene. Likewise, it is believed that the counter ions in the ion gel effectively neutralize the charged impurities on graphene.

Although it is generally assumed that the capacitance of a gate dielectric layer is constant and can be directly estimated from its dielectric constant and thickness ($C_{ox} =$

$\varepsilon_{ox}\varepsilon_0/t_{ox}$), it has been reported that C_{ox} can dramatically change depending on the type and the size of dielectric medium on top of graphene. Xia et al.[141] used Hall measurements to estimate the charge carrier density on graphene during back gating and they found that C_{ox} can increase by up to 2 orders of magnitude in presence of a high-k top dielectric medium such as water droplet. Because it is important to know accurate C_{ox} values for correct interpretation of electronic transport on graphene, we measured back-gate-induced charge on the graphene channel by integrating the displacement current (I_{BG}) while sweeping back gate bias. Note that the contribution of the gold pads was subtracted from total displacement current to estimate the gated charge on the graphene channel only. Figure 4.3b shows the induced charge densities in the graphene channel at different gate biases, in which C_{ox} values were estimated. In our devices, ~2 times increase in C_{ox} was observed after ion gel printing.

Figure 4.3c shows the sheet resistance $R_S = (V_{SD}/I_{SD})(W/L)$ of the graphene channel plotted against the induced carrier density $n_{ind} \approx -C_{ox}\,(V_{BG} - V_{BG,Dirac})/e$. To investigate the charge transport characteristics, the R_S–n_{ind} curves are fit to a model,[152] in which the total carrier density on the graphene channel (n_{tot}) is approximated by:

$$n_{tot} = \sqrt{n^{*2} + {n_{ind}}^2} \tag{4.1}$$

where n^* is the residual carrier density at the Dirac point. Although ideal monolayer graphene is a zero bandgap material and has zero DOS at the Dirac point, a non-zero residual carrier density is always observed because there are (1) thermally excited electrons/holes in conduction/valence bands, respectively, (2) electron/hole puddles on

graphene introduced by potential fluctuations at randomly distributed charged impurities on SiO_2 substrate,[153] and (3) structural defects of the graphene. With a given n_{tot}, the sheet resistance is given by:

$$R_{\mathrm{S}} = R_{\mathrm{contact}}\left(\frac{W}{L}\right) + R_{\mathrm{channel,S}} = R_{\mathrm{contact}}\left(\frac{W}{L}\right) + \frac{1}{n_{\mathrm{tot}} e \mu} \tag{4.2}$$

where R_{contact} is the contact resistance at the metal/graphene contacts, $R_{\mathrm{channel,S}}$ is the sheet resistance of graphene channel, e is the charge of an electron, and μ is the mobility of charge carriers, respectively. The parameters R_{contact}, n^* and μ obtained from the curve fitting are summarized in Table 4.1.

Due to the asymmetric nature of the data obtained before ion gel printing, electron ($n_{\mathrm{ind}} < 0$ cm^{-2}) and hole ($n_{\mathrm{ind}} > 0$ cm^{-2}) transport regimes are fit to two different curves of equation 4.2. Such asymmetric carrier transport has been attributed to carrier-dependent Coulomb scattering cross-sections at charged impurities[140,154,155] and contact-induced

Table 4.1. Physical parameters of the G-FETs shown in Figure 4.3c.

	Before ion gel printing		**After ion gel printing**	
	Hole	Electron	Hole	Electron
C_{ox} (nF/cm^2)	6.70 ± 0.01		13.03 ± 0.01	
$V_{BG,Dirac}$ (V)	87.6		-9.3	
$R_{contact}$ (kΩ)	-0.09 ± 0.09	2.81 ± 0.01	1.27 ± 0.09	
n* (x 10^{12} cm^{-2})	0.76 ± 0.01	1.07 ± 0.00	0.70 ± 0.01	
μ (cm^2 V^{-1} s^{-1})	1131 ± 23	1020 ± 3	1069 ± 22	

*The errors denote standard errors in curve fitting.

doping in graphene adjacent to the metal contact[156–159] which leads to gate bias dependent injection barriers. The ion gel printed G-FET, in contrast, shows a much more symmetric transfer curve that can be fit to a single curve of equation 4.2. This is likely a result of the ionic screening effect; since the counter ions in the ion gel effectively neutralize the charge impurities on graphene, Coulomb scattering at the impurities becomes less dependent on carrier type. Chen et al.[160] also reported a decrease in asymmetric transport in the G-FETs immersed in concentrated ionic solutions. Interestingly, we observed only slight change in carrier mobility (Table 4.1), while neutralization of charged impurities generally leads to significant increase in carrier mobility.[139,161] This might be because the increased interaction between graphene and adjacent ions,[141,162] which does not exist before the ion gel printing, cancels out the benefit of charge neutralization.

Determination of C_Q by Tracking E_F in Back Gating Mode. Figure 4.4a displays the electrochemical potentials of the graphene channel (V_{Gr}) with respect to the potential of a Pt reference electrode measured at different back gate biases. V_{Gr} is shifted to a more negative (positive) potential when a positive (negative) back gate bias is applied. This trend can be understood as a result of the Fermi level shift within the graphene energy band due to back-gate-induced charge. That is, as a positive back gate bias induces more electrons to fill the energy band of graphene, the Fermi level shifts to a higher energy level with respect to the Dirac point. Because the V_{Gr} shift reflects how electrons fill the energy band, we can estimate the DOS (or quantum capacitance, C_{Q}) of graphene from it.

Before doing so, it is useful to consider energy band diagrams. Figures 4.5a and 4.5b show the energy band diagrams of a G-FET with electrolyte in contact with the

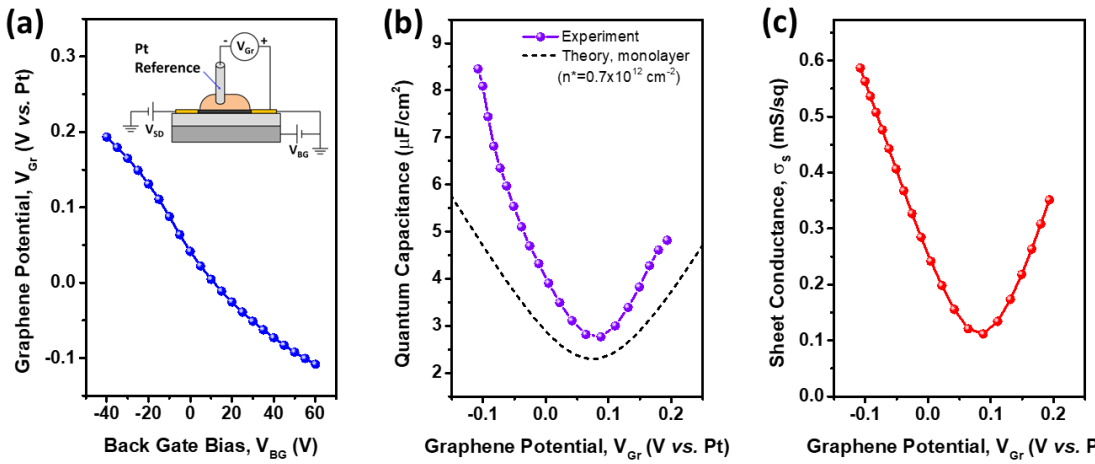

Figure 4.4. (a) Electrochemical potential of the graphene channel V_{Gr} measured during back gating. The inset represents the electrical configuration for the measurement; (b) Quantum capacitance of graphene C_Q obtained from the data in (a). The dashed line represents the quantum capacitance of monolayer graphene estimated by the model from ref. 135 with $n^* = 0.7 \times 10^{12}$ cm^{-2} and $v_F = 10^6$ m/s; (c) Sheet conductance measured during back gating. Note that data in (a) and (c) are obtained simultaneously at V_{SD}=10 mV and dV_{BG}/dt = 29.5 V/s.

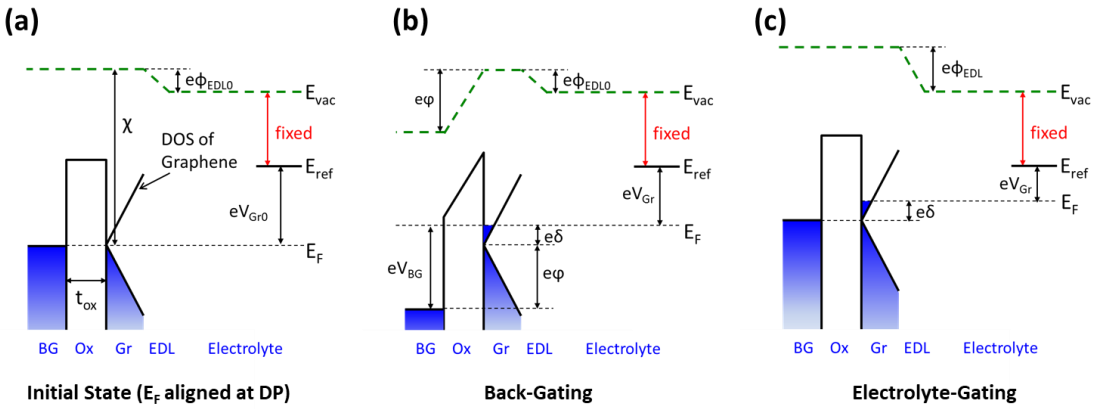

Figure 4.5. Energy diagrams of an ion gel coated G-FET (a) at an initial state where the Fermi-level (E_F) is aligned to the Dirac point (DP) of graphene channel at zero back gate bias, (b) when a positive back gate bias (V_{BG}) is applied to the G-FET (back gating), (c) when a negative bias is applied to the graphene channel with respect to the Pt counter electrode (electrolyte gating). BG, Ox, Gr, EDL, and Electrolyte in the diagrams denote back gate, oxide gate dielectric, graphene, electrical double layer, and ion gel, respectively. χ, δ, and φ represent the work functions of an undoped graphene, the band filling potential in graphene, and the potential drop within the oxide dielectric layer, respectively. E_{vac} and E_{ref} represent the local vacuum level and the Fermi level of the Pt quasi-reference electrode, respectively.

channel when zero and a positive voltage biases are applied to the back gate, respectively. For simplicity, it is assumed that (1) the Fermi level is aligned to the Dirac point of the graphene channel in the initial state (Figure 4.5a) where zero bias is applied to the back gate; (2) no charge transfer occurs across the graphene/electrolyte interface; and thus (3) all electronic charge induced by gating is confined within the atomically thin graphene layer. The electric field within the bulk electrolyte phase should be zero at equilibrium because otherwise the mobile ions in the electrolyte are redistributed so that any non-zero electric field in the bulk electrolyte is cancelled out. Accordingly, the entire potential drop (or vacuum level shift) from the graphene surface to the bulk electrolyte occurs only within the EDL formed at the graphene/electrolyte interface as shown in Figure 4.5. Similarly, the back-gate/SiO_2/graphene stack can be regarded as a parallel plate capacitor, in which the electric field generated by a voltage bias V_{BG} is confined between the two plates and completely screened outside the capacitor. In this regard, it is assumed that the initial potential drop across the EDL (ϕ_{EDL0} in Figure 4.5a) is not affected by back gate bias. From the energy diagrams, we can derive the following relationships:

$$e\mathrm{V_{BG}} = e(\varphi + \delta) \tag{4.3}$$

$$n_{\mathrm{ind}} = -\mathrm{C_{ox}}\,\varphi/e \tag{4.4}$$

$$\mathrm{e}\delta + e\mathrm{V_{Gr}} = e\mathrm{V_{Gr0}} \tag{4.5}$$

where δ indicates the deviation of electrode potential from the Dirac point, and φ indicates the potential drop within the oxide dielectric layer. Accordingly, the quantum capacitance of graphene $\mathrm{C_Q}$ (F/cm^2) is given by:

$$C_Q = -\frac{dQ_{ind}}{d\delta} = -e\frac{dn_{ind}}{d\delta} = C_{ox}\frac{d\varphi}{d\delta} = -C_{ox}\left(\frac{dV_{BG}}{dV_{Gr}} + 1\right) \quad (4.6)$$

Figure 4.4b shows the quantum capacitance extracted from Figure 4.4a using equation 4.6. The minimum capacitance is observed at $V_{Gr} = 0.07$ V vs Pt, which is consistent with the Dirac point observed in the transfer curve (σ_S–V_{Gr}) shown in Figure 4.4c. Note that the experimentally obtained C_Q is comparable to, but systemically larger than the theoretically predicted[135] curve of monolayer graphene (the dashed line in Figure 4.4b, calculated with $n^* = 0.7 \times 10^{12}$ cm^{-2} from Table 4.1). This difference is at least partially attributed to the additional capacitance derived from defects and multilayer phases in CVD graphene. In the Raman analysis of CVD graphene on SiO_2, which can be found in Section 3.2.1, we observed ~18% of our sample is composed of multilayer islands with ~1−3 μm sizes while most areas were the monolayer phase.

The deviation from the theory may also be attributed to the assumption that the EDL structure is not influenced by back gate bias. Although this is a good approximation that allows us to keep our model simple, it may not be rigorously true because the closest ions in the electrolyte are only a few nanometers away from the charge plane in graphene. In such a situation, local interaction between the charges induced in graphene and the ions very near the graphene surface can be strong enough to disturb the EDL structure. For example, consider a situation where back-gate-induced electrons in graphene attract more cations in electrolyte to the graphene surface due to the local interactions. This 'partial' charge transfer to the electrolyte phase would reduce the potential drop across the EDL (i.e., ϕ_{EDL0} in Figure 4.5b). Since this results in V_{Gr} responding less sensitively to back

gate bias, the C_Q calculated from equation 4.6 becomes larger than the actual quantum capacitance of graphene. To better understand the influence of back gate bias on EDL structure, further theoretical and experimental investigations must be pursued and integrated into a more rigorous model.

Separation of $\Delta\delta$ from $\Delta\phi_{EDL}$ via Simultaneous Back and Electrolyte Gating. Figure 4.6a shows the σ_S–V_{Gr} curves obtained in back and electrolyte gating, respectively. If a constant carrier mobility is assumed, the sheet conductance σ_S of the graphene channel is simply determined by the total carrier density in the channel regardless of whether the carriers are induced by back gating or by electrolyte gating. As can be seen from equation 4.5, V_{Gr} shift observed in back gating mode (Figure 4.4a) is essentially the Fermi level shift within graphene (i.e., the *band filling potential* δ, which occurs because induced charge carriers fill graphene's energy bands). Therefore, the larger V_{Gr} shift observed in

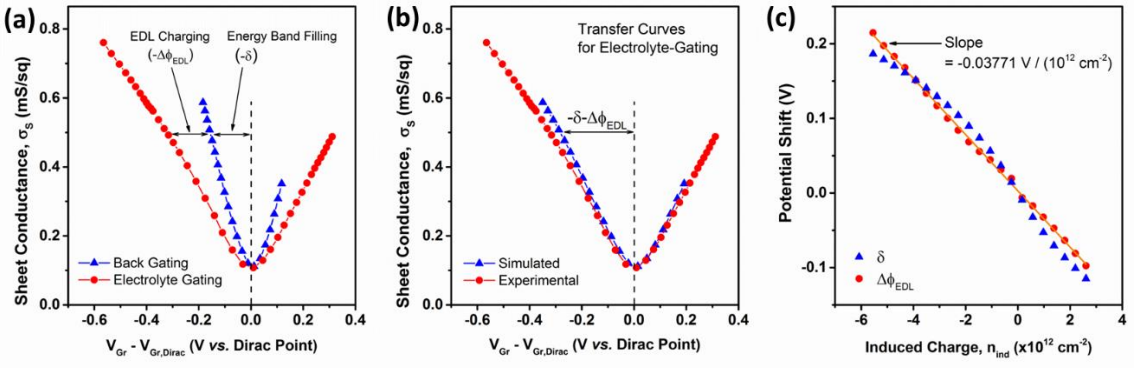

Figure 4.6. (a) Sheet conductance (σ_S) versus electrochemical potential of graphene (V_{Gr}) obtained during back gating and electrolyte gating at V_{BG}=0 V. (b) Experimental and simulated σ_S–V_{Gr} curves for electrolyte gating. (c) δ and $\Delta\phi_{EDL}$ as a function of induced charge density in the graphene channel $n_{ind} \approx -C_{ox}(V_{BG} - V_{BG,Dirac})/e$. Note that $\Delta\phi_{EDL}$ in (c) is obtained from the potential difference between the back gating and the electrolyte gating curves in (a).

electrolyte gating than that in back gating in Figure 4.6a indicates that an additional potential appears in electrolyte gating mode to attain a certain sheet conductance. Referring again to the energy level diagrams in Figure 4.5, we can see this additional potential is essentially the potential required for charging EDL capacitor. Figure 4.5c shows the energy diagram of the G-FET that is electrolyte gated from its initial state in Figure 4.5a. The following equations can be derived from an energy balance in Figures 4.5a and 4.5c.

$$\begin{aligned}\chi &= eV_{\mathrm{Gr0}} + \left(E_{\mathrm{vac,el}} - E_{\mathrm{ref}}\right) + e\phi_{\mathrm{EDL0}} \\ &= e\delta + eV_{\mathrm{Gr}} + \left(E_{\mathrm{vac,el}} - E_{\mathrm{ref}}\right) + e\phi_{\mathrm{EDL}}\end{aligned} \tag{4.7}$$

or

$$(V_{\mathrm{Gr}} - V_{\mathrm{Gr0}}) = -\delta - (\phi_{\mathrm{EDL}} - \phi_{\mathrm{EDL0}}) = -\delta - \Delta\phi_{\mathrm{EDL}} \tag{4.8}$$

where χ is the work function of undoped graphene, and $E_{\mathrm{vac,el}}$ and E_{ref} are the vacuum level of the electrolyte and the Fermi level of the Pt reference electrode, respectively. Because an EDL can be considered as a nanometer-thick capacitor consisting of two parallel charge planes at the electrode surface and adjacent electrolyte (i.e., electrons/holes induced on the electrode surface and the corresponding counter ions), the electrolyte-gate-induced charge density in each layer is the same (i.e., $n_{\mathrm{ind}} = -\mathrm{Q}_{\mathrm{EDL}}/e = -\mathrm{C}_{\mathrm{EDL}}\Delta\phi_{\mathrm{EDL}}/e$, where $\mathrm{C}_{\mathrm{EDL}}$ is the EDL capacitance). Therefore, the additional potential change $\Delta\phi_{\mathrm{EDL}}$ in equation 4.8 (referred to as *double layer charging potential*) can be interpreted as the potential required to charge EDL capacitor. Figure 4.6b shows two σ_{S}–V_{Gr} curves for electrolyte gating, one of which is the experimental curve also presented in Figure 4.6a, and the other is a simulated curve, which is obtained by shifting the potential V_{Gr} of each

back gating data point in Figure 4.6a by the expected double layer charging potential (i.e., $-\Delta\phi_{\mathrm{EDL}} = en_{\mathrm{ind}}/\mathrm{C_{EDL}} \approx -\mathrm{C_{ox}}\,(\mathrm{V_{BG}} - \mathrm{V_{BG,Dirac}})/\mathrm{C_{EDL}}$ where $\mathrm{C_{EDL}}$ =5.43 μF/cm^2 is obtained from the dual gating experiments discussed below). The two transfer curves nearly coincide with each other, supporting the idea that the difference between the back gating and the electrolyte gating curves in Figure 4.6a is the double layer charging potential. The slightly smaller σ_{S} in the experimental curve compared to the simulated curve in the high carrier density regime ($\left|\mathrm{V_{Gr}} - \mathrm{V_{Gr,Dirac}}\right| > 0.2$ V) probably originates from the difference in Coulomb scattering effects in back and electrolyte gating.[162] Figure 4.6c shows a plot of δ and $\Delta\phi_{\mathrm{EDL}}$ with respect to n_{ind}. At this point, our measurements and analysis are able to separate δ and $\Delta\phi_{\mathrm{EDL}}$ in electrolyte gating, subject to two approximations: (1) that the carrier mobility is essentially the same for back and electrolyte gating and (2) that the second term in equation 4.8 is near zero for back gating.

It is also noteworthy that the ideal electrolyte gating shown in Figure 4.5c, in which the voltage drop within the oxide dielectric (φ) remains constant and thus there is no back gate induced charge in the graphene channel, changes the back gate bias to $\mathrm{V_{BG}} = \delta$. This means that back gate induced charge during the "actual" electrolyte gating, which is conducted while $\mathrm{V_{BG}}$ is fixed at 0 V (grounded), is non-zero. Nevertheless, as long as $\mathrm{V_{BG}}$ is fixed while electrolyte gating, we can ignore the back gate contribution to the total induced charge in graphene because $\left|\Delta n_{\mathrm{ind,BG}}/\Delta n_{\mathrm{ind}}\right| \ll 1$. This is a direct consequence of the fact that $\mathrm{C_Q} \gg \mathrm{C_{ox}}$ for entire δ range.

Determination of the $\mathrm{C_{EDL}}$. Importantly, the dual gate configuration also allows accurate determination of $\mathrm{C_{EDL}}$. From the slope of the $\Delta\phi_{\mathrm{EDL}}$ vs. n_{ind} in Figure 4.6c, the

EDL capacitance can be estimated: $C_{EDL} = -e\Delta n_{ind}/\Delta\phi_{EDL}$ = ~4.22 μF/cm^2. It should be noted, however, that the carrier mobility should be assumed to be the same for back and electrolyte gating to obtain $\Delta\phi_{EDL}$ shown in Figure 4.6c, and thus mobility discrepancy in the two gating modes can introduce error in the C_{EDL} estimation. To avoid this problem and better estimate C_{EDL}, we performed dual gating of a G-FET in which source-to-drain current was measured while electrolyte gating at fixed back gate biases from -70 to 70 V. As shown in Figures 4.7a and 4.7b, the potential at the Dirac point ($V_{Gr,Dirac}$) systematically shifts with the applied back gate bias. At the Dirac point in each curve, the back gate induced charge is counterbalanced with electrolyte-gate-induced charge, giving minimum carrier density and sheet conductance.

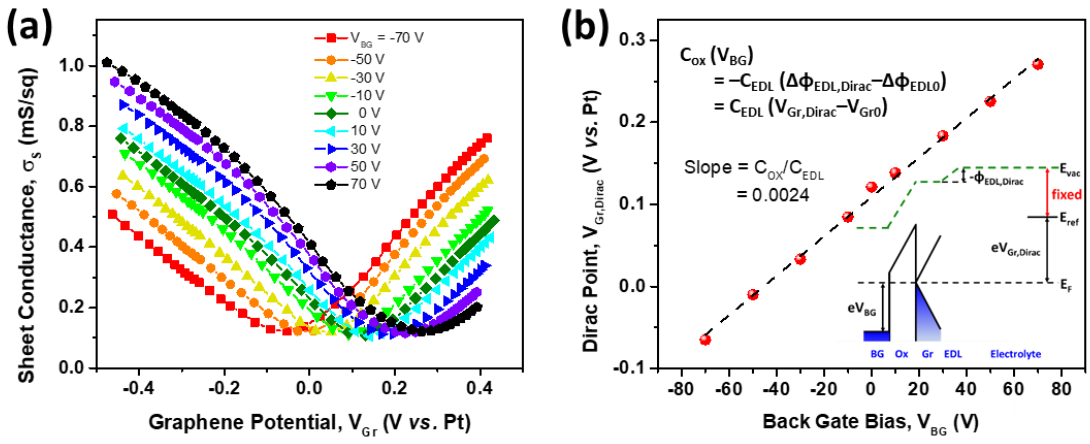

Figure 4.7. (a) Sheet conductance measured during electrolyte gating at dV_{EG}/dt = 0.59 V/s, V_{SD}=10 mV, and fixed back gate biases from −70 V to 70 V. (b) The electrochemical potential of graphene at the Dirac point at different back gate biases. The inset shows an energy diagram where the back-gated and electrolyte-gated charges are counterbalanced and the Fermi-level is aligned at the Dirac point.

Therefore, the following charge balance relationship holds at each Dirac point ($\delta = 0$ V).

$$\begin{aligned} \mathrm{C_{ox}}(\mathrm{V_{BG}}) &= -\mathrm{C_{EDL}}\left(\phi_{\mathrm{EDL,Dirac}} - \phi_{\mathrm{EDL0}}\right) \\ &= \mathrm{C_{EDL}}\left(V_{\mathrm{Gr,Dirac}} - V_{\mathrm{Gr0}}\right) \end{aligned} \tag{4.9}$$

Note that this relationship is derived from the energy diagrams in Figure 4.5a and 4.7b (inset). Accordingly, from the slope of the plot shown in Figure 4.7b, the EDL capacitance is estimated to be $\mathrm{C_{EDL}} = \mathrm{C_{ox}}/0.0024 = 5.43$ μF/cm^2. Previously, Zhang et al.[138] measured the EDL capacitance of similar ion gel sample ([EMI][TFSA] with 10 wt % SMS(18-86-18)) using electrochemical impedance spectroscopy (EIS) analysis. The reported EDL capacitance (~6 μF/cm^2 at 1 Hz at 30 ºC) is close to the value obtained in this work. From the obtained EDL capacitance, the double layer charging potential required in electrolyte gating ($\Delta\phi_{\mathrm{EDL}} = -en_{\mathrm{ind}}/\mathrm{C_{EDL}}$) can be calculated without the assumption of mobility invariance for back and electrolyte gating modes.

One final point is that $\delta \sim \Delta\phi_{\mathrm{EDL}}$ (Figure 4.6c), which is a consequence of the fact that $\mathrm{C_Q} \sim \mathrm{C_{EDL}}$. Indeed, $\mathrm{C_Q}$ ranges from ~2.5 to ~8.5 μF/cm^2 (Figure 3.4b), which is comparable to the obtained $\mathrm{C_{EDL}}$.

Hysteresis in Transfer Curves of Back- and Electrolyte-Gated G-FETs. Figure 4.8 shows the transfer curves of G-FETs in forward and reverse sweep of (a-c) back-gating and (d) electrolyte-gating modes, respectively. While negligible hysteresis was observed in I_{SD}–V_{BG} curve before ion gel printing (Figure 4.8a), significant hysteresis was observed at the same V_{BG} sweep rate after ion gel printing (Figure 4.8b). Recently, Levesque et al.[144] demonstrated that the charge transfer between graphene and adjacent donors/acceptors (e.g.

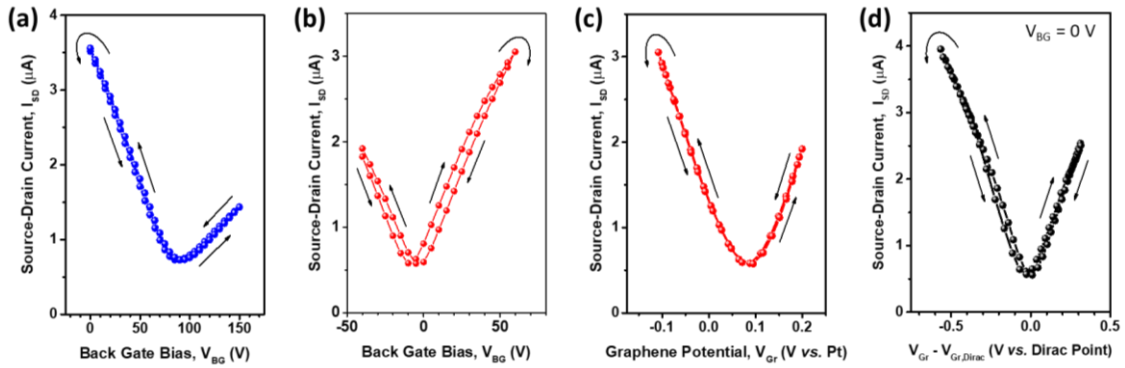

Figure 4.8. Source-to-drain current vs. back gate bias (I_{SD}−V_{BG} curves) of the G-FET (a) before and (b) after ion gel printing. The data was obtained at V_{SD}=10 mV and $dV_{BG}/dt = \pm 29.5$ V/s. (c) Source-to-drain current vs. graphene potential (I_{SD}−V_{Gr}) curve of the ion gel printed G-FET. Note that the data in (b) and (c) were simultaneously measured in back gating mode. (d) I_{SD}−V_{Gr} curve obtained in electrolyte gating mode with V_{SD}=10 mV, V_{BG}=0 V, and $dV_{EG}/dt = \pm 0.59$ V/s, where V_{EG} is the voltage applied to the Pt counter electrode.

O_2/H_2O molecules adsorbed on the graphene surface) is an important mechanism that causes large hysteresis in I_{SD}−V_{BG} curves. Likewise, when the Fermi level in the graphene channel shifts to a sufficiently high energy level at $V_{BG} \gg 0$ V in our device, the electrons induced in the graphene channel can transfer to adjacent electron acceptors in ion gel phase rather than reside in the graphene channel. Because this charge transfer reduces the number of electrons in graphene channel at $V_{BG} \gg 0$ V, the Dirac point is observed at more positive V_{BG} in the reverse sweep (Figure 4.8b). The hysteresis leads to less accurate estimation of charge carrier density and quantum capacitance C_Q (especially at high V_{BG}), and thus should be minimized. In this work, smaller hysteresis could be achieved by increasing the V_{BG} sweep rate (Figure 4.9). The fast V_{BG} scan makes the Fermi level stay at the high energy range for shorter time, and thus minimizes the hysteresis caused by charge transfer between graphene and the electrolyte.

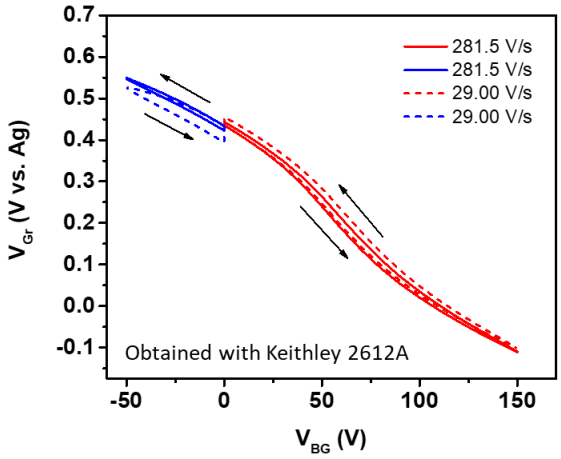

Figure 4.9. Hysteresis in V_{Gr}–V_{BG} curves at two different V_{BG} scan rate. Note that the faster V_{BG} scan rate generates smaller hysteresis.

Negligible hysteresis is observed in the I_{SD}–V_{Gr} curve (Figure 4.8c), where V_{Gr} was simultaneously measured in the back gating mode (Figure 4.8b). This shows that V_{Gr}, rather than V_{BG}, is a good indicator of charge carrier density in the graphene channel especially when there is significant charge transfer between graphene and ion gel phase.

Lastly, we observed little but observable hysteresis in $I_{SD}-V_{Gr}$ curves in the electrolyte-gating mode (Figure 4.8d). It is believed that this small hysteresis comes from relatively slow ionic transport, which does not occur in back-gating mode, compared to carrier injection into the graphene channel—the slow ion transport prohibits the EDL structure at the graphene/ion gel interface from reaching thermodynamic equilibrium and thus V_{Gr} at a given carrier density in graphene can have different values in the forward and reverse sweeps.

4.5. Conclusion

In this chapter, we demonstrated (1) the effects of ion gel coating on back gate capacitance and carrier transport in graphene; (2) an electrolyte-modified G-FET

architecture that enables simultaneous estimation of the quantum capacitance C_{Q}, the double layer capacitance C_{EDL}, carrier density, and energy band alignments of graphene at a given gating condition. It was observed that the ion gel coating leads to more symmetric carrier transport as well as ~2 times higher back gate capacitance. By measuring the changes in the electrochemical potential during back gating and electrolyte gating in the ion gel coated G-FETs, the potentials associated with (1) energy band filling δ in graphene and (2) double-layer charging $\Delta\phi_{\mathrm{EDL}}$ at the graphene/electrolyte interface could be experimentally separated. With the quantum capacitance and the double layer capacitance obtained from the experimental data, the carrier densities and the energy band alignments throughout the back gate/SiO_2/graphene/electrolyte system can be specified in terms of the back gate bias and the electrochemical potential of the graphene. Overall, the electrolyte-modified G-FETs provide an excellent model system for probing the electronic structure and transport properties of graphene and for understanding the differences between the two gating mechanisms. This basic strategy should be applicable to other 2D materials.

5. Field Effect Modulation of Outer-Sphere Electrochemistry on ZnO Electrodes: Cyclic Voltammetry Study†

5.1. Abstract

Here we report field-effect modulation of solution electrochemistry at 5 nm thick ZnO working electrodes prepared on SiO_2/degenerately doped Si back gates. We find that an ultrathin ZnO electrode behaves like a 2D semiconductor, in which charge carriers electrostatically induced by the back gate lead to band edge shift at the front electrode/electrolyte interface. This, in turn, manipulates the charge transfer kinetics on the electrode at a given electrode potential. Experimental results and the proposed model indicate that band edge alignment can be effectively modulated by 0.1-0.4 eV depending on the density of states in the semiconductor and the capacitance of the gate/dielectric stack.

5.2. Introduction

The electrochemistry of semiconductors is central to the development of photoelectrochemical conversion systems[163–167] and to understanding the geophotochemistry of light-absorbing minerals in water,[168] for example. The recent advent of ultrathin two dimensional (2D) semiconductor materials prepared either by exfoliation[89,169] or thin film growth methods[42,170] opens up new opportunities to examine the role of dimensionality in semiconductor electrochemistry.[171–179] A particularly

† Reproduced in part with permission from Kim, C.; Frisbie, C. D. *J. Am. Chem. Soc.* **2016**, *138*, 7220. Copyright 2016 by the American Chemical Society

intriguing possibility explored here is to exploit the transverse field effect[180]—so central to silicon CMOS technology—to modulate the carrier density in the valence (VB) and conduction bands (CB) of a 2D semiconductor that simultaneously serves as the working electrode (WE) in an electrochemical cell. This can be accomplished by placing the (grounded) 2D material on a metal gate/dielectric stack, Figure 1a, where application of voltage on the gate shifts the VB and CB edges with respect to the Fermi-level; this phenomenon is the transverse field effect.

The potential significance of such a field effect modulated WE architecture is two-fold: (1) because of the extreme thinness of the 2D material, the charge induced in the semiconductor by the back gate should in principle be accessible to an electrolyte solution on the opposite (front) face; (2) this charge is separate from, but in addition to, double-layer charge induced by the independently controlled WE potential with respect to the reference (RE). We posit that such a gate tunable semiconductor electrode may open opportunities to modulate (reduce) electrochemical overpotentials for both outer-[181–183] and inner-sphere[184,185] (electrocatalytic) redox reactions, and thus may serve as a useful platform for electrochemical investigations. To our knowledge, the possibility of gate tunable, ultrathin semiconductor electrodes has not been demonstrated before. For this initial demonstration, we focus on outer sphere redox chemistry at ultrathin ZnO electrodes, as described below.

5.3. Materials and Methods

Materials. Highly boron doped silicon wafers with thermally grown 300 nm-thick SiO_2 layer (SiO_2/*p*-Si) were purchased from Silicon Valley Microelectronics.

Polydimethylsiloxane (PDMS) blocks used for electrolyte reservoirs were made from the precursor solutions (Sylgard 184 Silicone Elastomer, Dow Corning). Platinum wires for reference and counter electrodes (99.99%, 100 μm and 500 μm in diameter, respectively) were purchased from Sigma-Aldrich. The redox species 2,3,5,6-tetrabromo-1,4-benzoquinone (TBBQ, >98%) and tris(2,2'-bipyridine) ruthenium(II) hexafluorophosphate ($Ru(bpy)_3(PF_6)_2$, 97%) were purchased from TCI America and Sigma-Aldrich, respectively, and used as received without further purification. The room temperature ionic liquid 1-buthyl-3-methylimidazolium bis(trifluoromethylsulfonyl) imide ([BMI][TFSI]) was synthesized by following the literature[186] by Dr. Hong Chul Moon.

Device Fabrication and Characterization. ZnO electrodes on back gates were prepared following the procedure fully described in Section 3.2.1 and 3.2.2. Briefly, a ZnO layer was deposited on a SiO_2/*p*-Si substrate (~300 nm thick oxide thermally grown on 525 μm thick degenerately boron doped silicon wafer) by atomic layer deposition (ALD),

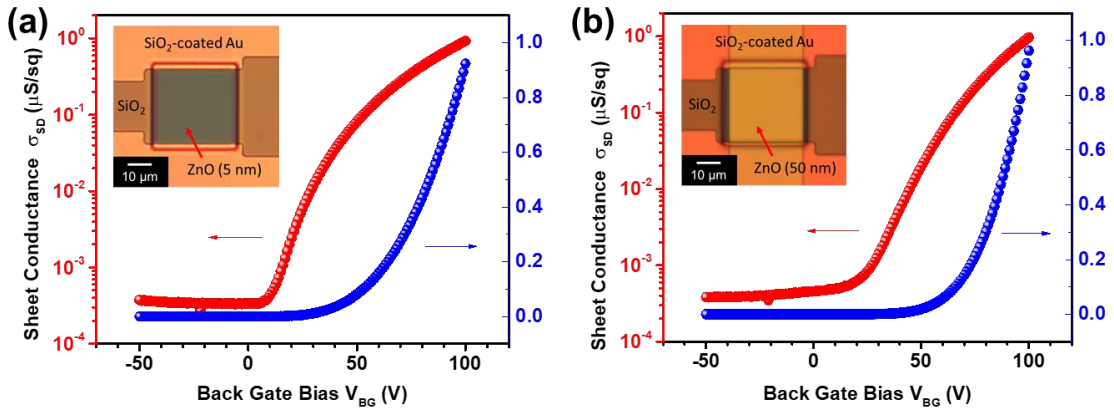

Figure 5.1. Sheet conductance (σ_{SD}) between two gold source and drain contacts versus back gate bias (V_{BG}) for (a) 5 nm thick and (b) 50 nm thick ZnO devices without electrolyte phase. Measurements were done in N_2 atmosphere.

followed by a series of annealing, photolithography, wet etching, and e-beam evaporation steps to make metal contacts and passivation layers that prevent electrochemical reaction from occurring on the metal contacts. We prepared 5 nm and 50 nm thick ZnO electrodes, both of which show n-type characteristics upon reaching the threshold back gate bias $V_{BG,T}$ at ~10−20 V (Figure 5.1); electrons induced at positive V_{BG} enhance sheet conductance of the ZnO layer between peripheral source and drain metal contacts while depletion of electrons at negative V_{BG} turns off the electronic conduction within the layer.

Electrochemical Measurements. To perform electrochemical tests while applying variable back gate biases, we configured the setup as shown schematically in Figure 5.2. All electrochemical measurements were performed at room temperature in a N_2-filled

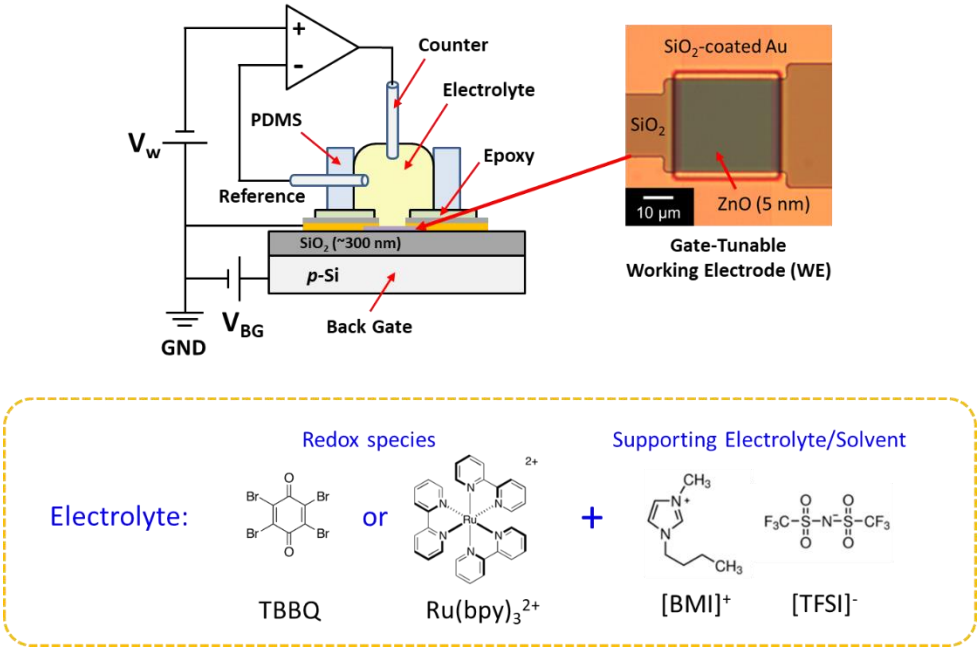

Figure 5.2. Cross-sectional view of a back-gated electrochemical cell with the experimental setup used in this study.

glove box with a 3-electrode configuration—thin ZnO (30 x 30 μm^2) as the WE, platinum wires as quasi-reference and counter electrode (100 μm and 500 μm in diameter, respectively), and the room temperature ionic liquid 1-butyl-3-methylimidazolium bis(trifluoro-methylsulfonyl) imide ([BMI][TFSI]) as supporting electrolyte and solvent.

Calibration of Pt Quasi-Reference Electrodes. WE potentials in redox-active electrolytes, if not specified, are reported vs. $Fc^{0/+}$ (i.e., the formal potential of ferrocene/ferrocenium on Au electrode) by using the redox species in the electrolyte as an internal standard. To calibrate the Pt quasi-reference electrode, all CV measurements were conducted first on gold electrode and then on ZnO electrode that were prepared on the same substrate (Figure 5.3). The gold electrode was prepared during the photolithography and the subsequent Ti and Au evaporation steps as described above but without further SiO_2 passivation. Figure 5.4 shows that the redox peak potentials (vs. Pt quasi-reference) of these two redox species on gold electrodes are neither a function of scan rate (dV_W/dt) nor applied V_{BG}. This indicates that (1) redox reactions of the redox species on gold are electrochemically reversible (i.e., charge transfer kinetics is fast), and (2) the electric field from the back gate is effectively screened in the bulk electrolyte and does not perturb the quasi-reference potential. In this regard, the formal potentials of $TBBQ^{0/-}$ or $Ru(bpy)_3^{2+/+}$ (estimated from the respective half wave potentials) on gold were used as internal standards to identify where the Pt quasi-reference potential indicates in each electrochemical cell. Knowing the redox potentials of $TBBQ^{0/-}$ and $Ru(bpy)_3^{2+/+}$ with respect to $Fc^{0/+}$ (Figure 5.4c and 5.4f), we reported working electrode potentials V_W in vs. $Fc^{0/+}$ scale, if desirable.

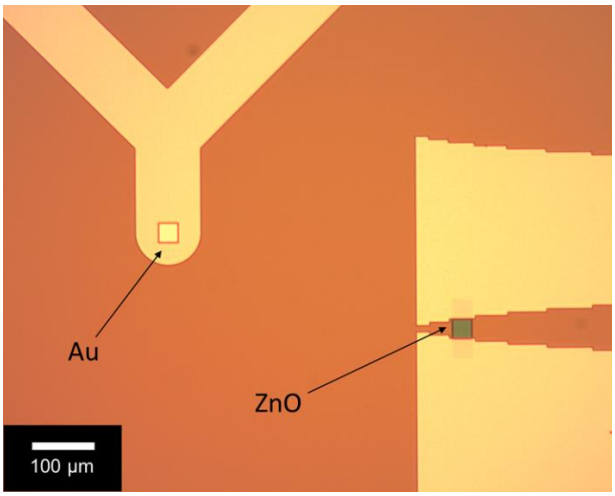

Figure 5.3. Optical image of ZnO and Au electrodes fabricated on a SiO_2/*p*-Si substrate. Note that the ZnO and the Au electrodes are exposed through square-shaped windows on transparent epoxy-based photoresist (SU8) film that covers the whole substrate.

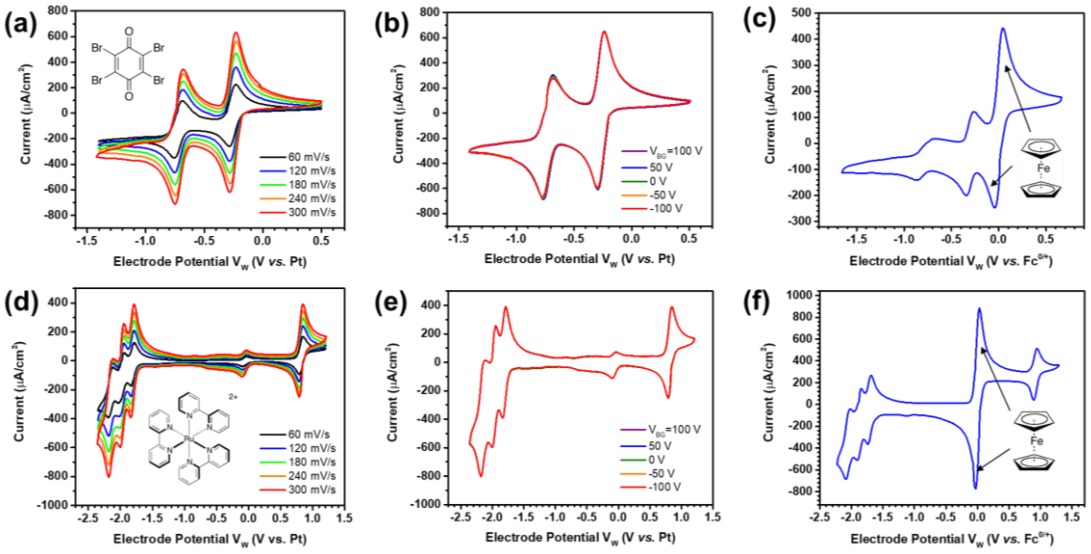

Figure 5.4. Cyclic voltammograms of (a-c) 10 mM TBBQ and (d-f) 10 mM $Ru(bpy)_3(PF_6)_2$ on gold electrodes. (a) and (d) were obtained at different V_W scan rates and V_{BG}=0 V. (b) and (e) were obtained at different back gate biases and V_W scan rate at 300 mV/s. (c) and (f) were obtained after ferrocene (Fc) was added to the electrolyte with V_W scan rate at 300 mV/s.

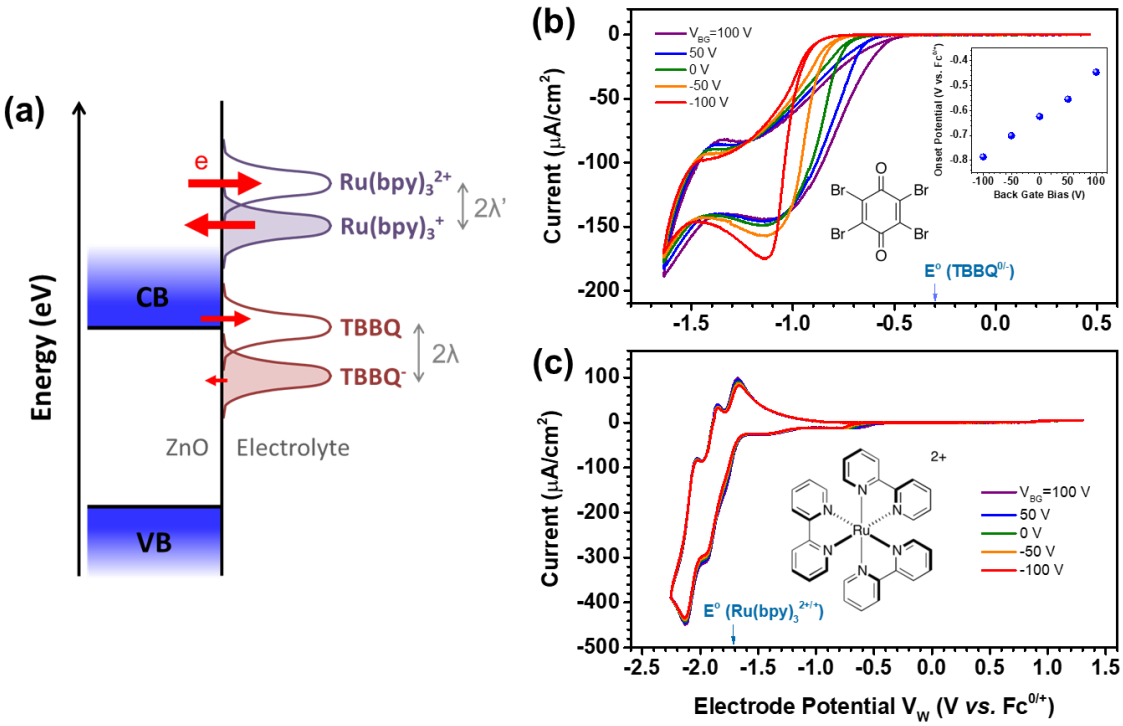

Figure 5.5. (a) Schematic showing electron transfer (red arrows) at ZnO/electrolyte interface. Note that λ represents solvent reorganization energy, and $TBBQ^{\bullet-}$ and $Ru(bpy)_3^{+}$ have lower energy than TBBQ and $Ru(bpy)_3^{2+}$, respectively, due to the solvent reorganization. Cyclic voltammetry results of (a) TBBQ and (b) $Ru(bpy)_3(PF_6)_2$ at a 5 nm thick ZnO electrode at different back gate biases (V_{BG}) from −100 V to 100 V. Inset in (a) shows the onset potential (V_{ON}), where the CV current becomes greater than 1 μA/cm^2, for each V_{BG}. The arrows on x-axes in (a) and (b) indicate the formal potential (E^o) of $TBBQ^{0/-}$ and $Ru(bpy)_3^{2+/+}$, respectively. All CV experiments were conducted in 10 mM [BMI][TFSI] solutions at scan rate of 60 mV/s.

5.4. Results and Discussion

Electrochemistry on 5 nm ZnO Electrodes. We conducted cyclic voltammetry (CV) measurements on 5 nm thick back-gated ZnO electrodes in 10 mM TBBQ or 10 mM $Ru(bpy)_3(PF_6)_2$ dissolved in [BMI][TFSI] (Figure 5.5). For the case of TBBQ voltammetry, it is crucial to note that the formal potential E^0 lies *below* the CB edge (~0.7 V vs. $Fc^{0/+}$) for ZnO[85] (*i.e.*, it lies in the band gap), as shown schematically in Figure 5.5a. The key result of this chapter is thus shown in Figure 5.5b, which displays the CV for TBBQ at the

5 nm ZnO electrode as a function of back gate voltage (V_{BG} relative to a grounded contact on the ZnO, Figure 5.2). At V_{BG} = 0 V (the green curve in Figure 5.5b), the first reduction peak of TBBQ is observed at −1.05 V, which is ~0.7 V more negative than E^0 on gold (Figure 5.4). A large overpotential is expected for TBBQ reduction at ZnO as E^0 lies in the band gap and a sufficient concentration of electrons in the CB must first accumulate, due to double layer charging, before reduction can commence. The important point evident in Figure 5.5b is that the onset of TBBQ reduction systematically shifts with V_{BG}. Positive V_{BG} shifts the CB edge down (more negative in electron energy)—closer to E^0—via the field effect. This results in a smaller overpotential for TBBQ reduction. Likewise, negative V_{BG} shifts the CB edge upward (more positive in energy) further from E^0 and increasing the overpotential. The shift is completely systematic and predictable based on a simple model described below. The absence of any significant reoxidation of $TBBQ^{\bullet-}$ in Figure 5.5b, at any gate voltage, is a consequence of the solvent reorganization energy 2λ (Figure 5.5a), which places the electronic manifold for $TBBQ^{\bullet-}$ even deeper in the band gap of ZnO. Thus, it is relatively easy, due to electronic state overlap, to reduce the TBBQ acceptor state once there is sufficient electron occupation of the higher lying ZnO CB, but the reverse process (i.e., reoxidation of $TBBQ^{\bullet-}$) is suppressed because of poor overlap between the $TBBQ^{\bullet-}$ electronic manifold and the CB.[70,71]

The CV of $Ru(bpy)_3^{2+}$ at an identical 5 nm thick ZnO electrode, shown in Figure 5.5c, serves as a control experiment because E^0 lies well above the CB edge for ZnO (Figure 5.5a). No additional overpotential, compared to the same process on gold electrode, is observed for multi-step reduction of $Ru(bpy)_3^{2+}$ because by the point at which the ZnO

WE potential reaches E^0, sufficient electron accumulation in the CB has occurred such that the ZnO surface in contact with the electrolyte is effectively metallic. Thus, reversible reduction *and* reoxidation of $Ru(bpy)_3^{2+}$ can take place at the formal potential (−1.71 V) as is well known in semiconductor electrochemistry.[70,71] Importantly, this behavior is independent of V_{BG} as anticipated given that E^0 for this redox couple is well above the CB edge. Evidently, even very large negative V_{BG} biases are not sufficient to push the CB edge of ZnO above E^0 for $Ru(bpy)_3^{2+}$. Altogether, the significant qualitative differences in the CVs for TBBQ and $Ru(bpy)_3^{2+}$ support the concept that the transverse field effect can modulate the rates of judiciously chosen outer-sphere electron transfer processes at ultrathin semiconductor electrodes.

The electronic coupling between the front and back faces of the 5 nm ZnO layer can also be verified by examining the ZnO source-to-drain sheet conductance σ_{SD} as function of its simultaneously controlled electrochemical potential V_w (i.e., 'front gate' potential) and back gate bias V_{BG}. Figure 5.6a displays σ_{SD} versus V_w at V_{BG} values ranging from −30 V to 50 V. At any one V_{BG} value, σ_{SD} increases as V_w sweeps negative due to electric double layer charging of the ZnO/electrolyte interface. That is, negative V_w values result in electron accumulation in ZnO and turn the conductance of the film 'ON'. There is a clear, systematic trend in the conductance onset with V_{BG}, namely as V_{BG} becomes more positive the conductance onset shifts to more positive V_w. This is shown explicitly in Figure 5.6b, which plots V_w versus V_{BG} at specific values of σ_{SD}. The apparent linear relationship between V_w and V_{BG} can be explained by recognizing that the gate/dielectric/

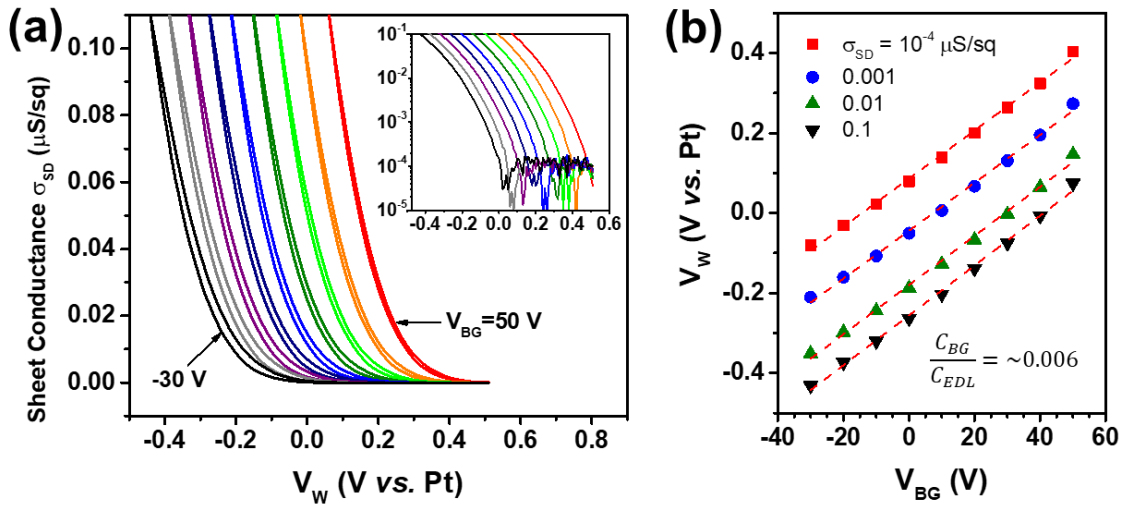

Figure 5.6. (a) Sheet conductance (σ_{SD}) of a 5 nm thick ZnO electrode in [BMI][TFSI] versus electrode potential (V_W) with back gate biases (V_{BG}) adjusted from −30 V to 50 V with 10 V intervals. The sheet conductance was obtained with V_{SD}=10 mV. The inset in (a) shows the same data on log scale. (b) V_W versus V_{BG} at designated σ_{SD} values.

ZnO/electrolyte stack can be viewed as two series-coupled capacitors. The total charge Q_W on the thin ZnO WE is expressed to a first approximation as:

$$Q_W = -C_{BG}V_{BG} + C_{EDL}V_W \tag{5.1}$$

where C_{BG} and C_{EDL} are the back gate and double layer capacitances, respectively. At fixed Q_W, corresponding to fixed σ_{SD} as in the Figure 5.6b plots, equation 5.1 predicts a linear relationship between V_W and V_{BG} with slope

$$\left(\frac{\partial V_W}{\partial V_{BG}}\right)_{\sigma_{SD}} = \frac{C_{BG}}{C_{EDL}} \tag{5.2}$$

Fits to the data in Figure 5.6b give C_{BG}/C_{EDL} ~ 0.006 consistent with the capacitance of the 300 nm SiO_2 dielectric (~20 nF/cm^2) and the estimated double layer capacitance (~10 μF/cm^2) measured with gold electrodes (Figure 5.7).

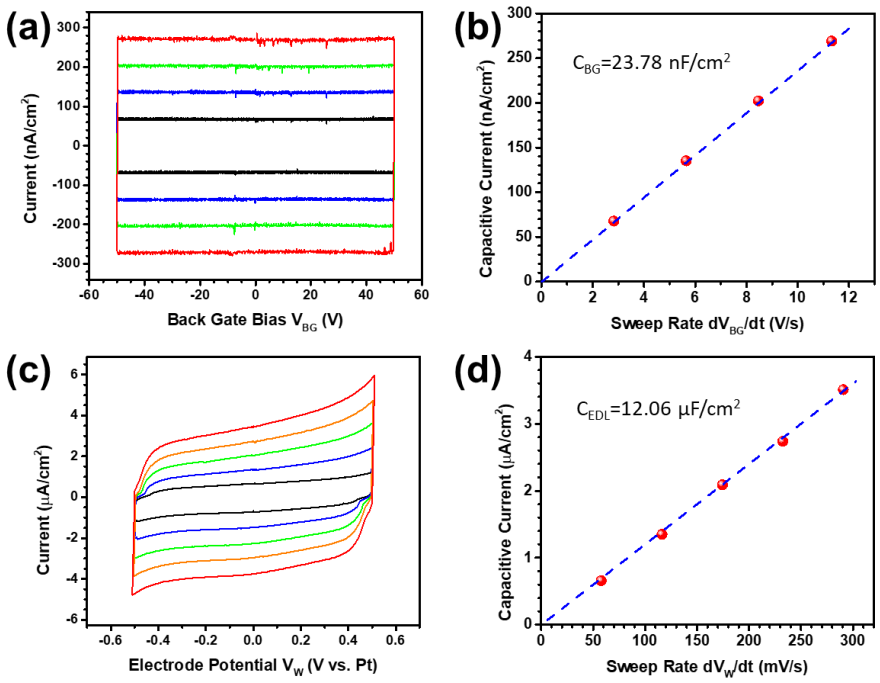

Figure 5.7. (a) Capacitive current in Au/SiO_2/*p*-Si structure with V_{BG} scan rates from ~3 V/s to ~12 V/s. Note that the capacitive current from the cables and the probes was subtracted from the raw data. (b) Averaged capacitive current versus the V_{BG} scan rates in (a). (c) EDL charging current on gold in [BMI][TFSI] with V_W scan rates from ~60 to ~300 mV/s. (d) Averaged EDL charging current versus V_W scan rates in (c). The gold electrodes used in (a) and (c) were prepared following the same procedure to prepare the metal contacts for ZnO. Relatively large Au electrodes (2 x 2 mm^2 and 400 x 400 μm^2 for (a) and (c), respectively) were used for measurements to increase the signal-to-noise ratio.

The data in Figure 5.6 demonstrate definitively that the front and back faces of the 5 nm ZnO layer are coupled; electron accumulations at the ZnO/dielectric and ZnO/electrolyte interfaces overlap, and thus for a given sheet conductance V_W and V_{BG} are strongly and predictably correlated. Importantly, identical sheet conductance measurements on 50 nm thick ZnO films, which will be discussed below, revealed no correlation between V_W and V_{BG}, again indicating that for thicker ZnO the front and back interfaces are not electronically coupled. Altogether, the sheet conductance measurements

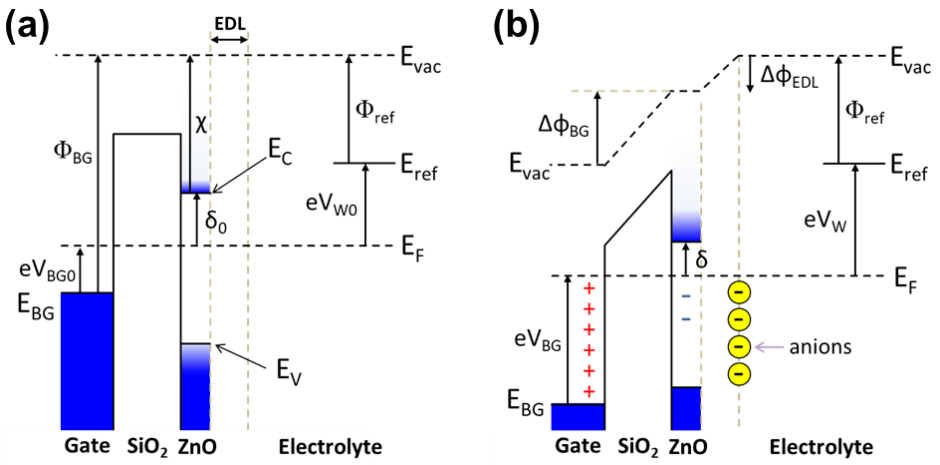

Figure 5.8. Energy diagrams of a back gated ultrathin ZnO electrode in electrolyte when the gate, the ZnO, and the electrolyte are in (a) electrically neutral (V_{BG}=V_{BG0} and V_W=$V_{W0,}$ analogous to a flat band condition in bulk semiconductor) and (b) charged (V_{BG}≠V_{BG0} and V_W≠V_{W0}) states. The symbols used in the diagram are as follows: CB edge (E_c) and VB edge (E_v) of ZnO, local vacuum level (E_{vac}); Fermi-levels of back gate (E_{BG}), ZnO (E_F), and RE (E_{ref}); work functions of back gate (Φ_{BG}) and RE (Φ_{ref}); electron affinity of ZnO (χ); vacuum level shifts in SiO_2 ($\Delta\phi_{BG}$) and EDL ($\Delta\phi_{EDL}$); CB edge offset (δ) from E_F in ZnO. Note that Φ_{BG}, Φ_{ref}, and χ are assumed to be constant.

support the conclusion from Figure 5.5b that the back gate can modulate band edge positions and redox chemistry at suitably thin ZnO working electrodes.

Physical Model for Gate-Tunable Electrodes. Schematic energy level diagrams shown in Figure 5.8 help to conceptualize the back gating experiment. In creating these diagrams, we have assumed that the 5 nm thick ZnO is essentially a 2D semiconductor in which the energy band bending within the electrode can be ignored. Figure 5.8a depicts the initial electrically neutral state at V_{BG}= V_{BG0} and V_W= V_{W0}, where δ_0 represents the initial offset of the CB edge from E_F. Figure 5.8b depicts a charged state that corresponds to the application of $V_{BG} \neq V_{BG0}$ and $V_W \neq V_{W0}$. In (pseudo-)equilibrium condition, the electric fields in the gate and the bulk electrolyte are zero due to effective screening by abundant free electrons and mobile ions in each phase. Therefore, the total charge in the

gate/dielectric/ZnO/electrolyte stack should be zero following Gauss's law—i.e., the charge density Q_W in the thin ZnO working electrode is the sum of the charge in the gate and the electric double layer (EDL) as follows:

$$-eQ_W = C_{\mathrm{BG}}\Delta\phi_{\mathrm{BG}} + C_{\mathrm{EDL}}\Delta\phi_{\mathrm{EDL}} \tag{5.3}$$

where e is the magnitude of the electronic charge, and $\Delta\phi_{BG}$ and $\Delta\phi_{EDL}$ are vacuum level shifts in the dielectric and the EDL, respectively. From Figure 5.8b, $\Delta\phi_{BG}$ and $\Delta\phi_{EDL}$ are given by:

$$\Delta\phi_{\mathrm{BG}} = eV_{\mathrm{BG}} + \delta + \chi - \Phi_{\mathrm{BG}} \tag{5.4}$$

$$\Delta\phi_{\mathrm{EDL}} = \delta + \chi - (eV_W + \Phi_{\mathrm{ref}}) \tag{5.5}$$

where χ is the electron affinity of ZnO, Φ_{BG} and Φ_{ref} are work functions of the gate and the reference electrode, respectively. Considering χ, Φ_{BG}, and Φ_{ref} are constant, we obtain the following fundamental relationship from equation 5.3−5.5:

$$dQ_W = -C_{BG}dV_{BG} + C_{EDL}dV_W - \frac{(C_{EDL} + C_{BG})}{e}d\delta \tag{5.6}$$

Assuming the sheet conductance σ_{SD} and Q_W are both solely determined by δ only, we get the following relation:

$$\left(\frac{\partial Q_W}{\partial V_{BG}}\right)_{\delta} = 0 = -C_{BG} + C_{EDL}\left(\frac{\partial V_W}{\partial V_{BG}}\right)_{\sigma_{SD}} \tag{5.7}$$

which in turn gives equation 5.2. The following relationships can also be derived from equation 5.6.

$$\left(\frac{\partial \delta}{\partial V_{BG}}\right)_{V_w} = \frac{-e}{1 + \frac{C_{EDL}}{C_{BG}} + \frac{C_W(\delta)}{C_{BG}}} \tag{5.8}$$

$$\left(\frac{\partial \delta}{\partial V_W}\right)_{V_{BG}} = \frac{e}{1 + \frac{C_{BG}}{C_{EDL}} + \frac{C_W(\delta)}{C_{EDL}}} \tag{5.9}$$

where $C_W(\delta)$ is the quantum capacitance of the working electrode given by:

$$C_W(\delta) = e\frac{dQ_W(\delta)}{d\delta} \tag{5.10}$$

Note that $C_W(\delta)$ essentially represents the density of states of the ZnO film in capacitance units and thus it has a strong dependence on δ. Assuming an ideal, trap state free ZnO film described with the free conduction electron model,[187] the total charge density $Q_W(\delta)$ can be estimated. Note that the charge density in the VB was ignored because ZnO has a large bandgap (3.2 eV). Since $\delta = E_c - E_F$, where E_c and E_F are the CB edge and the Fermi level in the ZnO layer, respectively, $Q_W(\delta)$ is given by:

$$\begin{aligned} Q_W &= e\, d \int_{E_c}^{\infty} \frac{1}{1 + \exp\left(\frac{E - E_F}{k_B T}\right)} \frac{4\pi (2m_n^*)^{3/2}}{h^3} \sqrt{E - E_c}\, dE \\ &= e\, d \int_{0}^{\infty} \frac{1}{1 + \exp\left(\frac{E + \delta}{k_B T}\right)} \frac{4\pi (2m_n^*)^{3/2}}{h^3} \sqrt{E}\, dE \end{aligned} \tag{5.11}$$

where d is the thickness of ZnO layer, k_B is Boltzmann's constant, T is temperature, h is Plank's constant, and m_n^* is the effective mass of electron for zinc oxide[188] (m_n^*=0.29 m_0 where m_0 is the mass of an electron in rest).

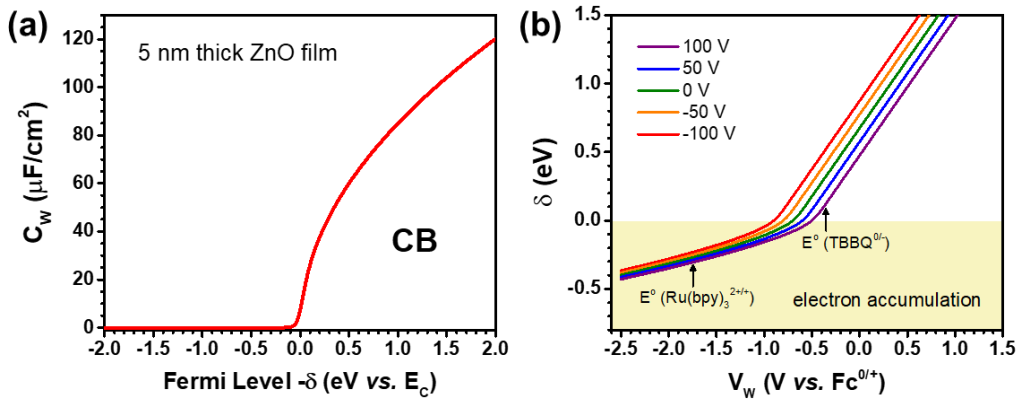

Figure 5.9. (a) Quantum capacitance (C_W) of 5 nm thick ZnO electrode calculated from the free conduction electron model. (b) CB edge offset (δ) at various V_W and V_{BG} conditions. The arrows in (b) indicate the formal potential E^o of TBBQ$^{0/-}$ and Ru(bpy)$_3^{2+/+}$.

Figure 5.9 shows the numerically calculated C_W and δ at various V_w and V_{BG} values. In the calculation, it is assumed that the Fermi level is aligned to the CB edge at V_w = −0.7 V and V_{BG} = 0 V. According to the calculation results, Δδ at fixed V_w=E^o_{TBBQ} is expected to be ~0.4 eV with V_{BG} swinging from −100 V to 100 V, while, for fixed V_w=$E^o_{Ru(bpy)3}$, the same V_{BG} range gives Δδ = ~0.07 eV. This result is qualitatively consistent with our observations shown above. Equations 5.8, which describes band edge shift (Δδ) achieved with application of V_{BG} at a fixed V_w, helps one to understand this trend. Since the reduction of TBBQ on ZnO occurs when the Fermi level is located near or well below the CB edge, where C_w is mostly negligible, TBBQ reduction kinetics can be effectively modulated by significantly shifting the band edge positions with V_{BG}. In contrast, redox reaction of Ru(bpy)$_3^{2+}$ occurs at far more negative potential, where the ZnO undergoes a semiconductor-to-metal transition via EDL charging, and only small Δδ can be achieved due to the huge C_w (~45 μF/cm^2 from the calculation) in the potential range. Ultimately, the magnitude of Δδ will also be controlled by the choice of back gate dielectric

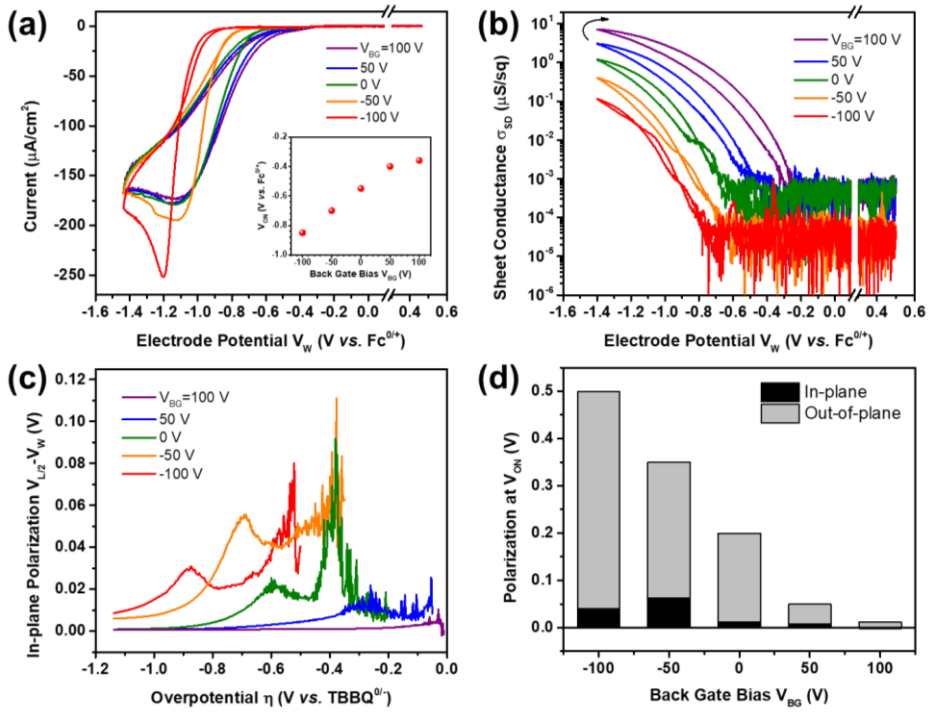

Figure 5.10. (a) Cyclic voltammetry results on a 5 nm thick ZnO electrode in 10 mM TBBQ solution with V_{BG} biased from −100 V to 100 V. Inset in (a) shows the onset potential (V_{ON}) at each V_{BG}. (b) Sheet conductance change in the ZnO electrode during the CV cycles. Note that V_{SD} is biased at 1 mV when V_{BG} =0, 50, 100 V and V_{SD} at 10 mV when V_{BG}=−50, −100 V, respectively, to improve signal in the measurements. (c) In-plane polarization ($V_{L/2} - V_W$) versus overall polarization, which is defined as the potential difference between V_W and E^o of $TBBQ^{0/-}$ (−0.35 V vs. $Fc^{0/+}$), during negative V_W scan. (d) In-plane and out-of-plane polarizations at V_{ON} for different V_{BG}.

material. Thin layers of high dielectric constant HfO_2, for example, can increase C_{BG} ten-fold over the 300 nm SiO_2 layer employed here, allowing larger Δδ values to be obtained.

In-plane Polarization on ZnO Electrodes. Figure 5.10a-c show the reaction current (i_{rxn}), sheet conductance (σ_{SD}=$1/\rho_s$), and the in-plane polarization ($V_{L/2} - V_W$) obtained by the method proposed in Section 3.3, respectively, that were simultaneously collected during CV cycles on a 5 nm thick ZnO electrode. In redox-active potential range (*i.e.*, $V_W < V_{ON}$), the in-plane polarization increases up to ~100 mV but does not exceed

25% of total polarization of the electrode for any V_{BG} (Figure 5.10c). This indicates that in-plane charge transport to the electrode center is relatively fast process and thus overall reaction kinetics is more limited by out-of-plane charge transfer and/or mass transport of redox species. Since there is negligible mass transport polarization in the beginning of TBBQ reduction, the total overpotential at onset potential (V_{ON}) can be divided into in-plane and out-of-plane polarizations as shown in Figure 5.10d. The data clearly shows that gate-controlled redox electrochemistry observed in TBBQ solution is essentially achieved by modulating out-of-plane charge transfer kinetics rather than in-plane charge transport kinetics. It is believed that the in-plane polarization can be more effectively eliminated on single crystal 2D semiconductors (*e.g.*, MoS_2, WSe_2) which have superior carrier mobilities.[189,190]

Electrochemistry on 50 nm ZnO Electrodes. As noted earlier, critical to this concept is that the electrons induced by the back gate are accessible to the electrolyte solution on the front side of the ZnO. Thus, it is expected that thick ZnO WEs in the same back-gated configuration should not show gate modulated electrochemistry, i.e., when the thickness of the ZnO film is greater than the transverse electric field screening length, gate modulated electrochemistry at the ZnO/electrolyte interface should not occur. Indeed, we observed little gate modulation of TBBQ voltammetry at 50 nm thick ZnO electrodes (Figure 5.11a), consistent with expectations. Note that the sheet conductance in Figure 5.11c also clearly shows that, for 50 nm ZnO, the front and back interfaces are not electronically coupled; the electrons induced by the back gate bias are not compensated by the holes induced from the front face via electrolyte gating and vice versa. The sheet

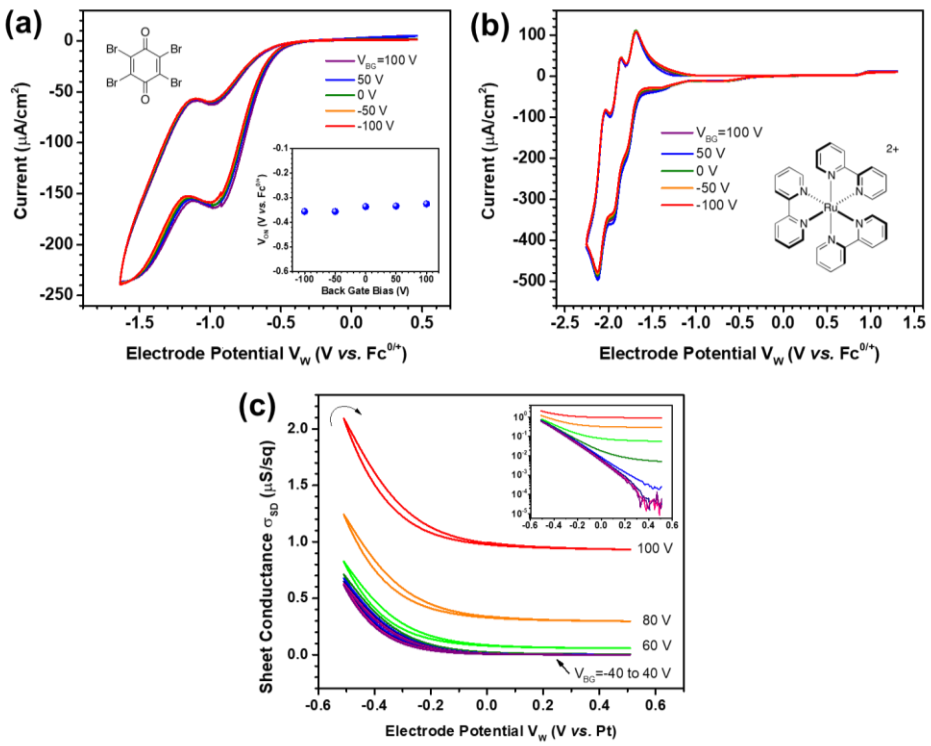

Figure 5.11. Cyclic voltammetry results of (a) TBBQ and (b) $Ru(bpy)_3(PF_6)_2$ on 50 nm thick ZnO electrodes at different V_{BG}. Inset in (a) shows the onset potential (V_{ON}), where the reduction current becomes greater than 1 μA/cm^2, at each V_{BG}. All CV experiments were conducted in 10 mM solutions with V_W scan rate at 60 mV/s. (c) Sheet conductance of the ZnO electrode in [BMI][TFSI] versus V_W at V_{BG} ranging from −40 V to 100 V with 20 V intervals. Inset of (b) shows the sheet conductance on log scale. The sheet conductance was obtained with V_{SD} biased at 10 mV.

conductance at a given V_{BG} asymptotically decreases with V_W to value obtained at the same V_{BG} in N_2 atmosphere (Figure 5.1b). This indicates the charges induced at the front and the back faces (by EDL charging and back-gating, respectively) are spatially separated, and thus charge induced at one face does not effectively compensate opposite charge induced at the other face. Further work is required to determine more precisely the critical thickness (between 5 and 50 nm) at which field effect modulation of the voltammetry can just be observed.

5.5. Conclusion

To summarize, we have demonstrated continuous, *in-situ* modulation of electrochemical reaction kinetics on ultrathin semiconductors with voltage biases applied to a back gate. The onset potential of TBBQ reduction at a 5 nm thick ZnO electrode could be shifted by ~0.4 V with back gate biases. The sheet conductance measurements in electrolyte and the model proposed in this work suggest that the observed gate-controlled redox reaction kinetics are essentially attributed to the shifts in band edge alignments at the electrode/electrolyte interface. Thus, the ability to control the band edge alignment independent of the working electrode potential should be generally useful for quantitative measurements of heterogeneous electron transfer rates at semiconductor/electrolyte interfaces.[181,182] The application of the back-gated electrode structure is not necessarily limited to the band alignment control demonstrated here but may also be employed to modulate surface chemisorption, or degree of band bending for thicker films, for example. We believe that fundamental understanding of gate-controlled electrochemical phenomena will provide a new research platform and an optimization tool for various semiconductor-based electrochemical systems.

6. Field Effect Modulation of Outer-Sphere Electrochemistry on ZnO Electrodes: Steady-State Kinetics Study

6.1. Abstract

Here we report the steady-state kinetic analysis of outer-sphere electrochemistry on *gate-tunable* ZnO working electrodes (i.e., ultrathin ZnO electrodes prepared on SiO_2/degenerate Si back gates). To realize the steady state in the electrolyte phase, a PDMS microfluidic channel is integrated on the gate-tunable ZnO electrode. In this flow cell, continuous supply of fresh electrolyte generates time-invariant diffusion layers near the ZnO surface, allowing steady-state kinetic analysis like other hydrodynamic methods. From the analysis, we found that the electron density on ZnO surface increases with the voltage bias applied to the back gate, while the rate constant for electron transfer decreases due to band alignment shift at the ZnO/electrolyte interface. This trend is consistent with the behaviors observed and predicted in Chapter 5, considering the energy distribution function of the redox species (TBBQ) used in this study; at a fixed working electrode potential, a positive back gate bias shifts the conduction band edge down, leading to an increased surface electron density and a reduced number of acceptor states available in the solution near the conduction band edge.

6.2. Introduction

Recently, our group demonstrated continuous and reversible tuning of outer-sphere redox reaction kinetics on *back-gated* ultrathin ZnO electrodes without altering chemistry of the system.[59] The redox reaction on a *back-gated* electrode becomes *gate-tunable*, in that the reaction rate at a given electrochemical potential is freely modulated by a voltage

bias applied to the *back gate* (note: the term *back gate* is adopted from MOSFETs because of their structural similarity). The idea underlying the gate-tunable electrode is to electrostatically induce extra charge carriers on the 2D electrode to alter the electrode/electrolyte interface. Because of extreme thinness of the 2D electrode, the gate-induced carriers are accessible to the electrolyte solution on the opposite (front) face and thus alter the electric double layer (EDL) structure (i.e., energy alignment at the electrode/electrolyte interface). In the previous studies, despite the fact that we could successfully modulate redox reaction rate at a given electrochemical potential, we could not fully clarify how the kinetic parameters of the redox reactions are influenced by the applied back gate bias in the overall potential range because the current-to-voltage responses obtained from cyclic voltammetry (CV) were not simple enough to interpret with well-known kinetic analysis techniques, such as Nicholson's method.[86] Accordingly, the current investigation introduced a more advanced electrochemical cell in which a microfluidic channel was integrated onto the gate-tunable electrode. In this *gate-tunable electrochemical flow cell*, continuous supply of fresh electrolyte under forced convection generates time-invariant diffusion layers near the electrode surface, so we can conduct steady-state analysis of the reaction kinetics on the gate-tunable electrode. Like other electrochemical cells using hydrodynamic methods, such as rotating electrode techniques, our flow cell provides several important advantages over CV including: (1) easier and more accurate analysis of charge transfer kinetics is possible because the mass transport contribution to the overall electrode polarization can be minimized under forced

convection; (2) the current flow measured on the electrode exclusively comes from redox reaction because double layer charging current does not flow at a steady state.

Herein, with the gate-tunable electrochemical flow cells and a rate law based on the Gerischer model,[70,71] we investigated how the charge transfer kinetics between an outer-sphere redox species and ultrathin ZnO film are modulated by a voltage bias applied to the back gate. Our results indicate that a positive back gate bias leads to an increased electron density on the ZnO surface but a reduced kinetic constant at a given electrochemical potential. Overall, the activation overpotential to attain a given reaction current decreases at a positive back gate bias because the electron density is more susceptible to the back gate bias than the rate constant. With the prediction from the Gerischer model, these experimental results confirm that the continuous and reversible change of charge transfer kinetics on ZnO surface is attributed to the gate-induced band alignment shift at the ZnO/electrolyte interface. We believe that the concept and the system adopted in this study will open new opportunities to modulate kinetics of other outer- and inner-sphere redox reactions and serve a useful platform for electrochemical investigations of various solid/liquid interfaces.

6.3. Materials and Methods

Materials. Highly boron doped silicon wafers with thermally grown 300 nm-thick SiO_2 layer on top (SiO_2/*p*-Si) were purchased from Silicon Valley Microelectronics. Polydimethylsiloxane (PDMS) precursor solutions (Sylgard 184 Silicone Elastomer) were purchased from Dow Corning. The redox species, 2,3,5,6-tetrabromo-1,4-benzoquinone (TBBQ, >98%), was purchased from TCI America. Platinum wires (99.99%, 500 μm in

diameter) for counter electrode, tetrahexylammonium hexafluorophosphate (THAP, ≥97%), silver nitrate (≥99%), and acetonitrile (MeCN, anhydrous, 99.8%) were purchased from Sigma-Aldrich. All chemical reagents were used as received without further purification.

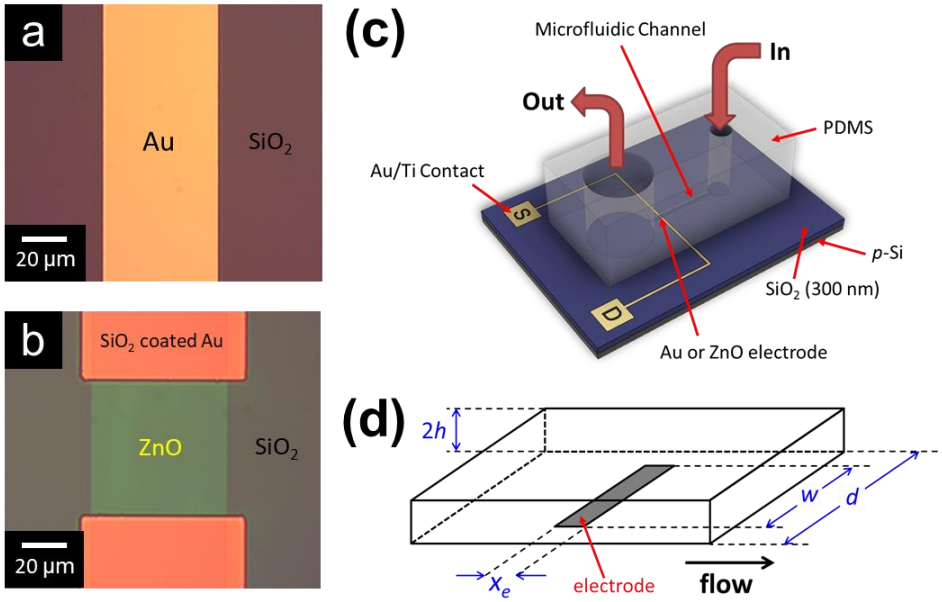

Figure 6.1. Optical images of (a) Au and (b) gate-tunable ZnO electrodes underneath PDMS microfluidic channel. (c) Structure of the gate-tunable electrochemical flow cell with Au or ZnO electrode. (d) Geometry of microfluidic channel (width d and height $2h$) and active electrode area (length x_e and width w).

Fabrication of Electrochemical Flow Cells. The fabrication procedure of gate-tunable ZnO electrodes (before integrating microfluidic channels on them) is thoroughly described in Section 3.2.1 and 3.2.2. Briefly, 5 nm ZnO film was grown on a SiO_2/*p*-Si substrate (~300 nm-thick oxide thermally grown on 525 μm thick highly boron doped silicon wafer) by atomic layer deposition (ALD), and a series of annealing, photolithography, wet etching was performed to pattern the ZnO film into an array of

microband electrodes with desired dimensions. Then a series of photolithography and electron beam evaporation steps were taken to prepare Au/Ti metal contacts (30 nm thick Au top layer on 3 nm thick Ti adhesion layer) and SiO_2 passivation layer that prevents electrochemical reaction from occurring on the metal contacts. Similarly, Au microband electrodes were prepared on a SiO_2/*p*-Si wafer by a series of photolithography and electron beam evaporation steps (3 nm Ti and 30 nm Au, respectively). Figure 6.1a and 6.1b show Au (50 μm wide) and ZnO (60 μm x 60 μm) electrodes prepared for this study.

For the hydrodynamic steady-state kinetic analysis, a microfluidic channel was prepared on a poly(dimethylsiloxane) (PDMS) block and integrated onto Au or ZnO electrodes as shown in Figure 6.1c. The width and the height (*d* and 2*h* in Figure 6.1d) of the microfluidic channel are 200 μm and 50 μm, respectively. To prepare PDMS microfluidic channels, we first fabricated a master mold via photolithography. To begin with, epoxy-based cross-linkable photoresist (SU-8 2050, MicroChem) was spin-coated on a Si wafer at 3000 rpm for 1 min and then soft baked at 65 °C and 95 °C for 2 min and 7 min, respectively, on a hot plate. To remove the thicker photoresist film built up on the edge of the wafer, which prohibits a close contact between the wafer and the photomask, we used a small stream of solvent (EBR PG, Microchem) while spinning the wafer at 700 rpm. After drying up the solvent, the wafer was exposed to UV light (12 mW/cm^2) for 14 s through the photomask with micro patterns using a contact mask aligner (MA6, SUSS MicroTec). The wafer was then baked at 65 °C and 95 °C for 2 min and 6 min, respectively, on a hot plate, and developed in SU-8 developer solution (MicroChem) for 3 min. For the developed patterns to be fully cured, the wafer was hard baked at 120 °C for >30 min.

Lastly, the master mold was treated with HMDS vapor for 30 min at room temperature to prevent the Si substrate from sticking to PDMS during the replication step. The height of the patterns on the master mold was measured to be ~50 μm by a surface profiler (P-16, KLA-Tencor).

To replicate the microchannel patterns, PDMS precursors (base:curing agent=10:1 in weight) were thoroughly mixed, vacuum de-aired, and carefully poured onto the master mold in a container made of Al foil. Then, the container was covered and transferred to a convection oven, so that the PDMS was cured at 65 °C for 4 hours. After cooling down to room temperature, the cured PDMS was carefully detached from the master mold, and cut into blocks with proper sizes so that each block has a microchannel at the center. In each PDMS block, two holes with 0.75 mm and 3 mm in diameters which served as the inlet and the outlet of the microfluidic channels, respectively, (as shown in Figure 6.1c) were made using punch tools.

Integration of a PDMS microfluidic channel on a gold or gate-tunable ZnO electrode was achieved by O_2 plasma treatment followed by thermal annealing. To maximize the mechanical integrity of the flow cell, the PDMS block (the microchannel side up) and the substrate (Au or ZnO side up) were treated with O_2 plasma in optimal condition[191] (gas composition: O_2 100%, pressure: 120 mTorr, power: 40 W, treatment time: 15 sec); the O_2 plasma improves bonding between PDMS and SiO_2 by removing surface contaminants, and introducing roughened bonding surfaces and reactive chemical groups. In particular, the surface functional groups –O-Si$(CH_3)_2$ on PDMS are converted to silanol group (–OH), which can form a chemical bonding (–Si-O-Si–) with another

silanol group on SiO_2 via condensation. While observing the alignment between the microfluidic channel and the electrodes on the substrate through the transparent PDMS block with an optical microscope, the two components were assembled so the active electrode is located near the outlet of the microfluidic channel. The assembled flow cell then was annealed at 100 °C and 120 °C for 30 min each on a hot plate. Lastly, the back gate (i.e., *p*-Si) of the flow cell was scratched with a tungsten carbide tip and painted with a silver paste to provide a better electrical contact to the instruments.

Electron Mobility in ZnO Electrode. The electron mobility on the prepared ZnO electrode was calculated from its transfer curve (I_D vs. V_{BG}) shown in Figure 6.2, which was obtained in a nitrogen-filled glove box without electrolyte phase. Given the applied $V_{SD} = 10$ mV and V_{BG} varying from −50 to 100 V, the device works as a MOSFET with a n-type semiconductor in a linear regime, in which the drain current I_D is given by equation 2.1. The threshold voltage $V_{BG,T}$ of 65.9 ± 0.6 V was observed, and the electron mobility was calculated to be ~1.1 $cm^2\ V^{-1}\ s^{-1}$ with $C_{BG} = 23.8\ nF/cm^2$ from Figure 5.7.

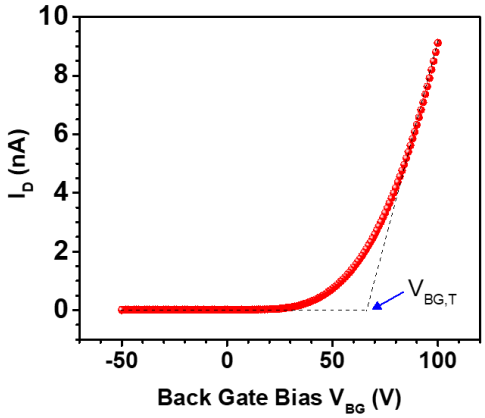

Figure 6.2. Transfer curve (I_D vs V_{BG}) of a ZnO device obtained at V_{SD}= 10 mV in N_2 environment without electrolyte. The threshold voltage $V_{BG,T}$ of identical devices are observed at 65.9 ± 0.6 V.

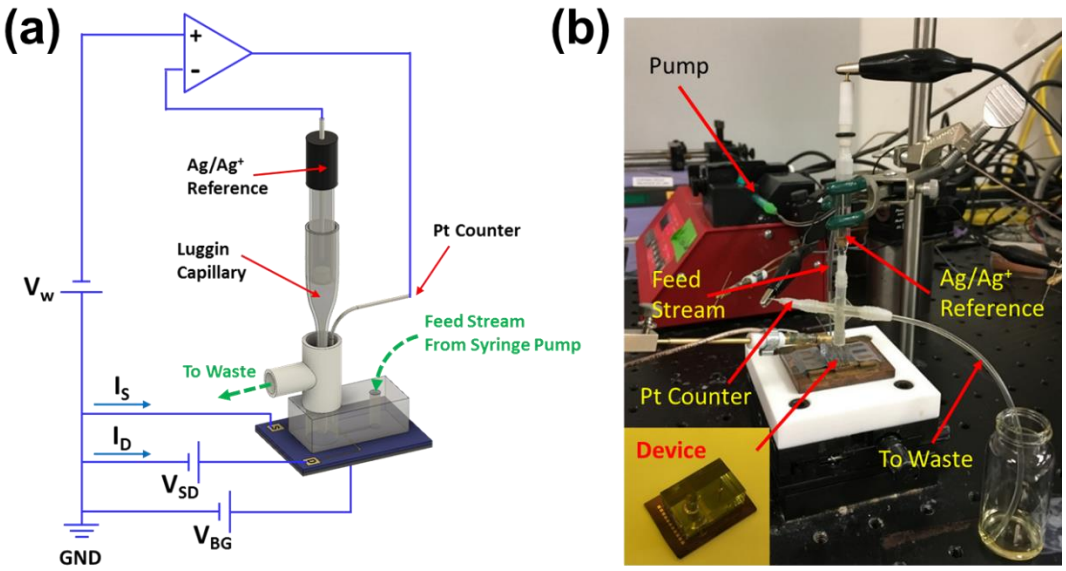

Figure 6.3. (a) Electrical configuration and electrolyte solution streams connected to the flow cell. The symbols indicated in the scheme are as follows: WE potential (V_w), source (I_s) and drain (I_d) current, source-to-drain bias (V_{SD}), and back gate bias (V_{BG}). (b) photograph of the experimental setup and the device (inset) used in this study.

Instrumental Setup for Steady-State Analysis. To perform electrochemical measurements while applying variable back gate biases, we configured the instrumental setup as schematically shown in Figure 6.3a. In this study, TBBQ and THAP were used for the outer-sphere redox species and the supporting electrolyte, respectively. 0.5−2.0 mM TBBQ and 0.1 M THAP in MeCN solution was supplied to the microfluidic channel using a syringe pump (Model 00323VE, Cole-Parmer). An Ag/Ag^+ reference electrode (BASi Co., filled with 10 mM $AgNO_3$ and 0.1 M THAP in MeCN) was plugged to a Luggin capillary filled with 0.1 M THAP in MeCN, and the tip of the capillary was placed at the outlet of the microfluidic channel. A platinum wire used for the counter electrode was placed ~3−5 mm away from the outlet of the microfluidic channel. Note that, if not specified in the article, V_{SD} in Figure 6.3a is set to 0 V. The reaction current I_w at the grounded working electrode (WE) was obtained from the sum of the current flow through

source and *drain* (i.e., I_S and I_D in Figure 6.3a, respectively). For ZnO electrodes, V_{BG} was applied to the back gate (i.e., *p*-Si) to induce the *field effect*. The complete detail of the electrical connections to multiple source meters for electrochemical measurements can be found in Section 3.3. All electrochemical measurements were performed at room temperature in ambient condition and the data were collected with an in-house LabVIEW program.

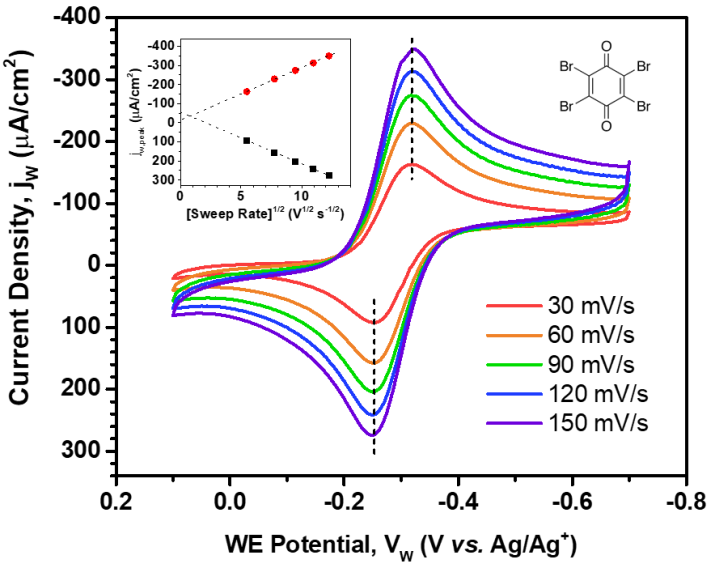

Figure 6.4. Cyclic voltammograms of 1 mM TBBQ and 0.1 M THAP in MeCN solution on gold electrodes which are obtained at different V_W scan rates. Inset shows the cathodic and anodic peak current densities as a function of (sweep rate)$^{1/2}$.

Formal Potential of TBBQ. The formal potential $U^{0\prime}$ of the TBBQ was estimated by cyclic voltammetry (CV) in a stationary electrochemical cell. A gold disk electrode (BASi Co., 1.6 mm in diameter) and a platinum wire (500 μm in diameter) were used as working and counter electrodes, respectively. An Ag/Ag$^+$ reference electrode (BASi Co., filled with 10 mM $AgNO_3$ and 0.1 M THAP in MeCN), which is identical to one used for

flow cell experiments, was prepared for the CV measurement. The electrolyte was 1 mM TBBQ and 0.1 M THAP dissolved in MeCN. Figure 6.4 shows the cyclic voltammograms of the TBBQ solution obtained at five different V_w sweep rates. The cathodic and the anodic peak potentials ($\Delta V_{\mathrm{w,peak}} \approx 65$ mV) not varying at different sweep rates and the linearity between the peak current density $j_{\mathrm{w,peak}}$ and $(\mathrm{d}V_w/\mathrm{d}t)^{1/2}$ indicate that the redox kinetics of TBBQ on a Au electrode can be regarded as Nernstian, in which the half wave potential $U_{1/2}$ is given by:[61]

$$U_{1/2} = U^{0'} + \left(\frac{RT}{nF}\right) \ln\left(\frac{D_{\mathrm{red}}}{D_{\mathrm{ox}}}\right) \tag{6.1}$$

where R is the gas constant, T is the temperature, F is the Faraday constant, n is the number of electrons associated with the reaction, and D_{red} and D_{ox} are the diffusion constants of reduced and oxidized species, respectively. Assuming $D_{\mathrm{red}} = D_{\mathrm{ox}}$, $U^{0'}$ is estimated to be -0.286 V vs. $\mathrm{Ag/Ag^+}$.

Correction of V_{w} by IR Compensation. In this study, V_w in microchannel flow cells was corrected by "IR compensation", which offsets potential drop due to ohmic resistance between the WE and the reference electrode (RE), as follows. Like in other typical electrochemical systems, the equivalent circuit between the working, the reference, and the counter electrodes in the electrolyte in our system can be represented as Figure 6.5 (note: here V_{SD} is assumed to be 0 V and the back gate is not shown to focus only on the electrolyte phase). The blue components stand for the equipment for electrochemical measurements, and the black components represent the three electrode including the

interface with the electrolyte. The red components indicate the lumped ohmic resistances of the electrolyte between three electrodes: the *uncompensated resistance* R_{u}, the solution resistance R_{sol}, and the bridge resistance R_{bridge}. Although R_{bridge}, the ohmic resistance of the electrolyte filled in the Luggin capillary, can be significant, a properly designed electrical equipment accurately measures the solution potential at the tip of the Luggin capillary because the current I_{ref} through the reference electrode is minimized and the potential drop in the Luggin capillary ($I_{\mathrm{ref}}R_{\mathrm{bridge}}$) becomes negligible.

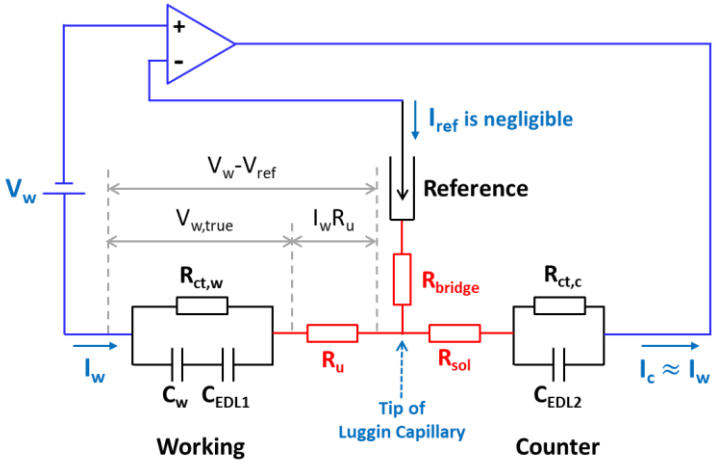

Figure 6.5. Equivalent circuit that represents the electrical connection (blue), the electrode/electrolyte interfaces (black), and bulk electrolyte between the working, the reference, and the counter electrodes (red).

When investigating the charge transfer kinetics on a working electrode, it is important to measure the actual potential difference applied at the electrode/electrolyte interface (i.e., $V_{\mathrm{w,true}}$ indicated in Figure 6.5). In practice, however, the working electrode potential ($V_{\mathrm{w}} - V_{\mathrm{ref}}$) obtained from the equipment should always include the additional ohmic polarization from iR_{u} as well as $V_{\mathrm{w,true}}$. Although R_{u}, in general, can be minimized by placing the tip of the Luggin capillary very close to the working electrode, such an

approach cannot be applied in our flow cell because inserting the tip to the microfluidic channel can cause an irregular flow pattern of the electrolyte near the working electrode. Therefore, the tip of the Luggin capillary is placed at the outlet of the microfluidic channel while the working electrode is located within the microfluidic channel but near the outlet. Even though the distance between the outlet and the working electrode is relatively short compared to the length of the entire channel, R_{u} can be significant due to the narrow nature of the microfluidic channel. Therefore, instead of eliminating R_{u} of the system, we offset the ohmic polarization to estimate $V_{\mathrm{w,true}}$ with an *IR compensation* technique described below.

Figure 6.6a shows a series of Au electrodes in a microfluidic channel, and Figure 6.6b shows the steady-state voltammograms of 2mM TBBQ solution (with 0.1 M THAP as the supporting electrolyte and MeCN as the solvent) obtained on the corresponding Au electrodes with volumetric flow rate $10\,\mu\mathrm{L/min}$. The voltammogram shows that the electrode polarization (i.e., $V_{\mathrm{w}} - V_{\mathrm{ref}}$) to attain a certain current I_w increases linearly with the distance, l, between the working electrode and the outlet, while the onset potential for TBBQ reduction is the same on all electrodes. The linearity between V_{w} and l is explicitly shown in the inset of Figure 6.6b, in which the slope is given by $I_w R_{\mathrm{u}}/l$. Considering the relationship $R_{\mathrm{u}} = l/\kappa A$, where κ is the bulk conductivity of the electrolyte and A is the cross-sectional area of the microfluidic channel (200 μm x 50 μm), κ is estimated to be to be 10.9 mS/cm. The obtained κ is very close to ~10 mS/cm, the bulk conductivity of 0.1 M tetrahexylammonium hexafluorophosphate (TBAP) dissolved in MeCN,[192] most likely due to their structural and chemical similarities. Given the fact that the total amount of the

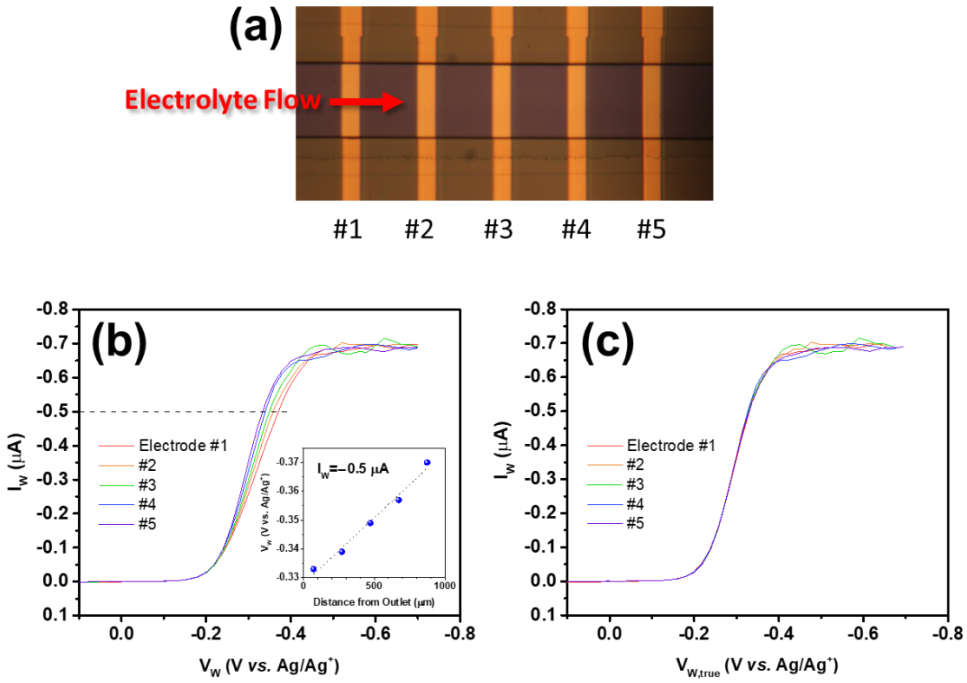

Figure 6.6. (a) Array of Au electrodes, numbered from #1 to #5, in a microfluidic channel. (b-c) Steady-state voltammograms of 2 mM TBBQ solution on the corresponding Au electrodes at V_f=10 μL/min. (b) shows the plot of raw data obtained from the measurement and (c) shows the same data corrected by IR compensation. Inset of (b) shows the electrode potential V_W to attain the I_W = −0.5 μA as a function of the distance from the outlet.

supporting electrolyte (THAP) is 50 times greater than the redox species (TBBQ), κ should be little influenced by the generation or consumption of the redox species during the redox reaction. Assuming a constant κ, $V_{\mathrm{w,true}}$ can be estimated as follows:

$$V_{\mathrm{w,true}} = V_w - I_w\left(\frac{l}{\kappa A}\right) \tag{6.2}$$

By correcting the electrode potential V_w in Figure 6.6b to $V_{\mathrm{w,true}}$, Figure 6.6c is obtained; the *IR compensation* makes the steady-state voltammograms on different Au electrodes nicely collapse on top of one another. Note that, in the rest of this chapter, the working

electrode potentials shown in all data plots are corrected by IR compensation, but designated as V_{w} for simplicity.

6.4. Results and Discussion

Mathematical Model for Outer-Sphere Electrochemistry in Microfluidic Channels. The hydrodynamic and electrochemical behaviors in our flow cells are described by the mathematical model explained in Section 3.5, which was developed to analyze quasi-reversible redox reaction with the form ($\mathrm{Ox} + e \rightleftarrows \mathrm{Red}$) where both oxidized (Ox) and reduced (Red) species are kinetically stable on the timescale of the experiment, and the bulk solution contains only Ox before it enters the flow cell. In all experiments conducted in this work, dimensionless parameters *Re* and *Pe* are kept in $0.93-14.9$ and $1.72 \times 10^3 - 2.76 \times 10^4$ ranges, satisfying the criteria that the analytical solutions of the model are valid.

Redox Reaction of TBBQ on Gold Electrodes. To confirm the validity of the experimental setup and the mathematical model used for this study, we first performed the hydrodynamic analysis of TBBQ reaction on gold microband electrodes. It is assumed the redox reaction follows Bulter-Volmer kinetics with k_f and k_b determined as:

$$k_f = k_0 \exp\left(-\frac{\alpha F}{RT}(V_w - U^{0'})\right) = k_0 \exp(-\alpha\theta) \tag{6.3}$$

$$k_b = k_0 \exp\left(\frac{(1-\alpha) F}{RT}(V_w - U^{0'})\right) = k_0 \exp((1-\alpha)\theta) \tag{6.4}$$

where α is the transfer coefficient, $U^{0'}$ is the formal potential of the redox couple, θ is a dimensionless potential, k_0 is the standard rate constant, R is the ideal gas constant, and T is the temperature.

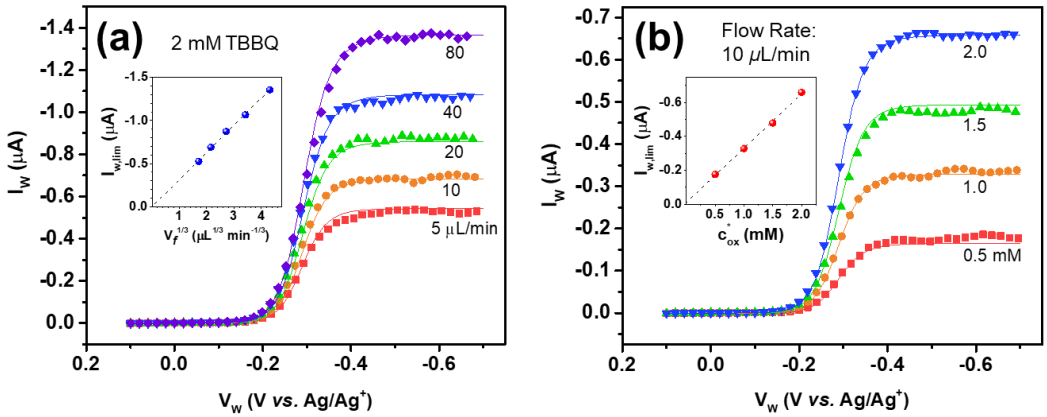

Figure 6.7. (a) Steady state voltammograms of 2 mM TBBQ solution on Au band electrode at different flow rates V_f. The inset of (a) shows the limiting current $I_{w,lim}$ vs $V_f{}^{1/3}$. (b) Steady state voltammograms of TBBQ solution on Au band electrode with different concentrations $c_{ox}{}^*$ and the flow rate fixed at 10 µL/min. The inset of (b) shows the limiting current $I_{w,lim}$ vs $c_{ox}{}^*$. The symbols and the lines in (a) and (b) indicate the experimental data and the simulated curves, respectively.

Figure 6.7a and 6.7b show that the steady-state voltammograms of TBBQ, which were obtained at different flow rates V_f and bulk concentrations $c_{ox}{}^*$, match well with the curves simulated with equations 3.11–3.13, 6.3, and 6.4 with parameters $k_0 = 0.3$ cm/s, $\alpha = 0.5$, and $D_{ox} = D_{red} \approx 1.4 \times 10^{-5}$ cm^2/s (note: Ox and Red correspond to TBBQ and TBBQ$^{\bullet-}$, respectively, in this work). The parameters used to fit the experimental data are consistent with the previously reported values ($k_0 = 0.3$ cm/s, $\alpha = 0.5$, and $D_{ox} = D_{red} = 1.25 \times 10^{-5}$ cm^2/s).[193] The insets of Figure 6.7a and 6.7b show that $I_{w,lim}$ have the good linear relationships with $V_f{}^{1/3}$ and $c_{ox}{}^*$ as predicted in equation 3.14. From these results,

we could confirm (1) a stable, time-invariant diffusion layer is formed near the electrode in our devices in the given V_f range, (2) $TBBQ^{\bullet -}$ radical formed by reduction of TBBQ is kinetically stable and does not further reduced to $TBBQ^{2-}$ as long as $V_w > -0.7$ V. We observed that sweeping the potential to more negative range leads to an insoluble organic film formed on the gold electrode. This unfavorable behavior becomes more severe when TBAP was used for the supporting electrolyte. Therefore, it is believed that $TBBQ^{2-}$ reacts with cations in supporting electrolyte to form insoluble film on the electrode like other quinone-type molecules.[194]

Redox Reaction of TBBQ on Gate-Tunable ZnO Electrodes. The energy diagram in Figure 6.8 schematically represents an example of the ZnO/electrolyte interface, where equimolar Ox and Red species are dissolved in the electrolyte and the applied V_w is slightly more negative than their formal potential $U^{0'}$ (i.e., $V_w = \frac{E_F - E_{\mathrm{ref}}}{-e} < U^{0'} = \frac{E^{0'} - E_{\mathrm{ref}}}{-e}$ where E_F and E_{ref} represent the Fermi levels of WE and RE, respectively). While the left side of the diagram represents the electronic states of an ideal ZnO surface which consists of the conduction band (CB) and the valence band (VB) separated by the bandgap energy (E_g=~3.2 eV for ZnO), the right side of the diagram represents the donor ($TBBQ^{\bullet -}$) and the acceptor (TBBQ) states (corresponding to Red and Ox, respectively) at the electrode surface (namely, outer Helmholtz plane, OHP). The Gerischer model, which is briefly explained in Section 2.4, explains that the energy difference between the donor and the acceptor states is due to the solvent reorganization energy λ (generally in the range 0.5-2 eV), and that their Gaussian type of distribution is a consequence of the thermal fluctuation of the solvation shell. Charge transfer rate at a given *E* is essentially determined by the

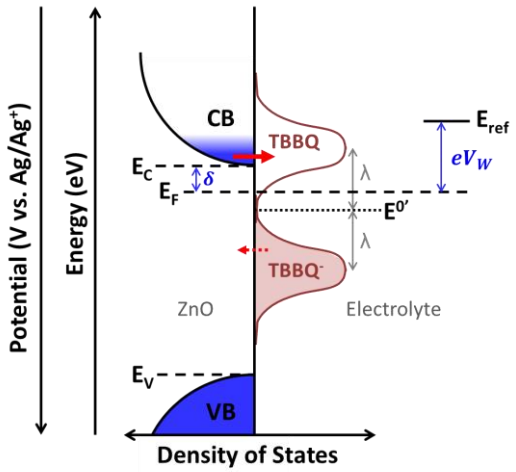

Figure 6.8. Schematic representation of DOS and electronic occupations at the surface of ZnO WE (left) and those in electrolyte solution containing equimolar TBBQ and $TBBQ^{\bullet-}$ (right). The symbols used in this diagram are as follow: CB edge (E_c) and VB edge (E_v) of ZnO; Fermi levels of ZnO WE (E_F) and RE (E_{ref}); CB edge offset (δ) from E_F in ZnO; electrochemical potential (vs reference) of the ZnO WE (V_w); energy level corresponding to the formal potential of TBBQ/$TBBQ^{\bullet-}$ ($E^{0'}$); and the solvent reorganization energy (λ). The red arrows indicate the electron transfer across the interface. Note that the electron transfer from CB to TBBQ is fast (expressed as a solid line) because the overlap between the filled (blue shadow in CB) and the empty states (TBBQ) is significant, while the electron transfer from $TBBQ^{\bullet-}$ to CB is negligible (expressed as a dotted line) because there are not acceptor states available in ZnO that can receive electrons from $TBBQ^{\bullet-}$.

overlap of occupied and empty states between the two phases. As already shown in Section 2.4, the cathodic and anodic current density (j_w^- and j_w^+, respectively) on the ZnO surface can be described as follows:

$$j_w^- \approx -k_{\text{et,max}} \exp\left[-\frac{\left(E_c - E^{0'} - \lambda\right)^2}{4k_B T\lambda}\right] n_s\, c_{\text{ox}} = -ek_{\text{et}}^-\, n_{\text{s}}\, c_{\text{ox}} \qquad (6.5)$$

$$j_w^+ \approx k_{\text{et,max}} \exp\left[-\frac{\left(E_c - E^{0'} + \lambda\right)^2}{4k_B T\lambda}\right] p_{\text{s}} c_{\text{red}} \;=\; ek_{\text{et}}^+\, p_{\text{s}}\, c_{\text{red}} \qquad (6.6)$$

where k_{et}'s are the rate constants ($cm^3\ s^{-1}$) for cathodic and anodic charge transfer, and n_s and p_s are the densities (cm^{-2}) of electrons and holes on 2D ZnO electrode, respectively. Note that E_F is assumed to be more than $2k_BT$ below CB edge (E_C) when deriving these equations. Considering $n_s \sim f(E_c)D(E_c)$ and $p_s \sim (1-f(E_c))D(E_c)$, we can get:

$$\left|\frac{j_w^-}{j_w^+}\right| \approx \exp\left[\frac{E_F - E^{0'}}{k_BT}\right]\frac{c_{ox}}{c_{red}} \tag{6.7}$$

Note that $c_{ox}/c_{red} \ll 1$ can be achieved only when $|j_w^-/j_w^+| \gg 1$ because, in our system, Red is initially not present and only generated from the reduction of Ox on the electrode. Therefore, as long as $E_F - E^{0'} \gg k_BT$ (i.e., $V_w - U^{0'} \ll -26$ mV), the anodic current density j_w^+ is negligible compared to the total current density ($j_w = j_w^- + j_w^+$) and $j_w \approx j_w^-$. When E_F lies within the bandgap, n_s in equation 6.5 can be approximated as:

$$n_s = N_c \exp\left[-\frac{(E_c - E_F)}{k_BT}\right] \tag{6.8}$$

where N_c is the effective DOS at the lower edge of the CB.

The mass transport effect in electrolyte can be corrected (see Section 2.4 for detail) as follows:

$$j_{w,k} = \left(\frac{1}{j_w} - \frac{1}{j_{w,lim}}\right)^{-1} = -ek_{et}^-\, n_s\, c_{ox}^* \tag{6.9}$$

Note that $j_{w,k}$ represents the reaction current density when the mass transport rate of Ox is extremely fast such that c_{ox} equals to c_{ox}^*. Being neither a function of k_f nor k_b (see

equation 3.14), the limiting current density $j_{w,lim}(=\frac{I_{w,lim}}{x_e w})$ is determined not by electrode materials but by a given set of $c_{ox}{}^{*}, D_{ox}, V_f$, and the geometry of the flow cell. Therefore, in this study, $j_{w,lim}$ measured on the Au electrodes is used to correct mass transport effect on the ZnO electrodes. The maximum error that can be potentially introduced by this correction method is less than 2%, because the $k_f = k_{et}^{-} n_s$ observed in our ZnO experiments is smaller than 6.3×10^{-7} cm/s (see Section 2.4 for detail).

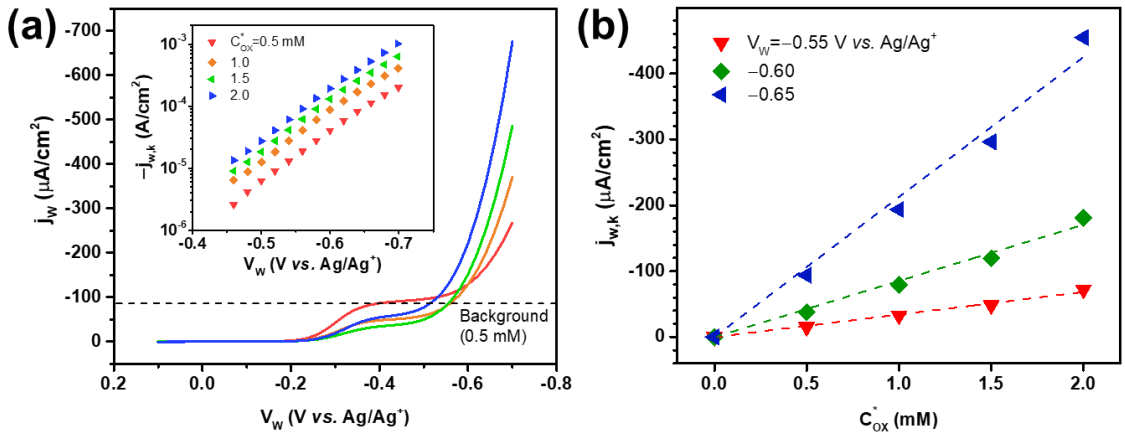

Figure 6.9. (a) Steady state voltammograms (j_w vs V_w) of TBBQ solution on gate-tunable ZnO electrode (where back gate bias V_{BG}=0 V) with different concentrations $c_{ox}{}^{*}$ and flow rate fixed at 10 μL/min. The inset of (a) shows the mass transport corrected reaction current density $j_{w,k}$ (in a log scale) at different $c_{ox}{}^{*}$ and V_w. (b) $j_{w,k}$ (in a linear scale) at different $c_{ox}{}^{*}$ and V_w.

To identify the relationship between $j_{w,k}$ and c^*_{ox}, we first obtained the j_w vs. V_w curves on ZnO electrodes at four different c^*_{ox} of TBBQ while applying constant $V_{BG} = 0$ V and $V_f = 10\ \mu$L/min. Figure 6.9a shows apparently two-step reduction of TBBQ with onset potential $V_{w,on}$ at -0.2 V and -0.45 V. Considering $V_{w,on}$ on Au electrode is -0.2 V (Figure 6.7), the apparent first reduction at -0.2 V is believed to come from the Au/Ti

metal contacts (most likely from their edges), which are not fully passivated with the SiO_2 film, to the ZnO electrode. The reduction current on the exposed Au should reach a constant value when V_w<-0.4 V because mass transport limiting condition is met at such a negative V_w range (Figure 6.7). Therefore, the reaction current on ZnO electrode should be obtained by subtracting the constant background current (indicated as the dashed base line in Figure 6.9a for c_{ox}^* =0.5 mM case) from the total current for each c_{ox}^*. It is noteworthy that the background current may not be merely proportional to c_{ox}^*, as is in Figure 6.9a, because the area of exposed Au in each device can be very different from one another. The inset of Figure 6.9a and Figure 6.9b show the good linear relationship between $j_{w,k}$ and c_{ox}^* in the V_w range from -0.45 V to -0.7 V, which is consistent with the rate law proposed in equation 6.9.

To investigate how charge transfer kinetics between TBBQ and a ZnO electrode is affected by the transverse *field effect*, j_w vs. V_w curves (Figure 6.10a) were obtained at different V_{BG} while maintaining constant c_{ox}^* and V_f at $0.5\,\text{mM}$ and $10\,\mu\text{L/min}$, respectively. We observed that the charge transfer rate between TBBQ and ZnO (i.e., j_w) at a given V_w gets faster at a positive V_{BG} and slower at a negative V_{BG}. In other words, the electrode polarization $\eta = V_w - U^{0'}$ to generate a given j_w systematically decreases with V_{BG}. The basic idea of applying V_{BG} is injecting extra charge carriers to the ZnO electrode surface; in the previous chapters, it is demonstrated that those extra charge carriers are fully accessible at the front face of the 2D electrode (i.e., the electrode/electrolyte interface). Potential origin of the reduced electrode polarization at a positive V_{BG} is two-fold: (1) reduced *out-of-plane* polarization due to improved charge transfer kinetics at the ZnO

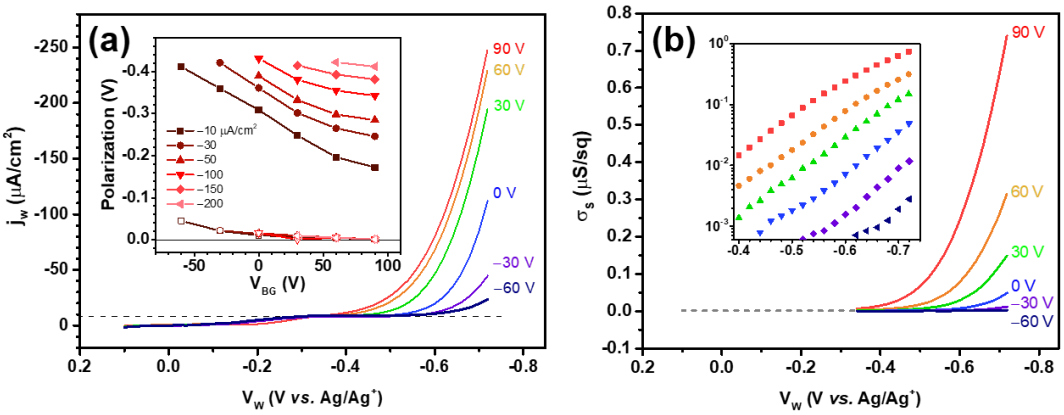

Figure 6.10. (a) Steady state voltammograms (j_{w} vs V_w) of 0.5 mM TBBQ solution on gate-tunable ZnO electrode at different back gate biases V_{BG} with flow rate V_f fixed at 10 μL/min. The inset in (a) shows how overall polarization (solid) and in-plane polarization (blank) of the ZnO electrode at given current densities j_{w} change with V_{BG}. (b) Sheet conductance of ZnO electrode (inset in a log scale) simultaneously obtained with the data in (a).

surface and (2) reduced *in-plane* polarization due to reduced ohmic resistance (i.e., increased n_{s}) within the ZnO electrode. In our gate-tunable electrodes, since the WE is prepared on the insulating SiO_2 rather than on a metallic current collector, the effect of in-plane polarization to overall reaction rate can be significant and thus should also be taken into account. To separate the contributions of those two polarizations, *in-situ* monitoring of the sheet conductance of the ZnO film was conducted by applying a small and constant V_{SD} during electrochemical measurements (Figure 6.10b, see Section 3.3 for experimental detail). The inset of Figure 6.10a reveals that the V_{BG}-induced change in the electrode polarization is mostly attributed to the out-of-plane polarization (e.g., up to 0.2 V change for $j_{\mathrm{w}} = -10\,\mu\mathrm{A/cm^2}$ when V_{BG} changes from −60 to 90 V) rather than in-plane polarization (e.g., up to 0.04 V change for the same j_{w} and V_{BG} range). Therefore, the systematic changes of j_{w} vs. V_{w} curves at different V_{BG} are not merely because of the V_{BG}-

induced change in ohmic resistance of the electrode but because of the V_{BG}-induced change in charge transfer kinetics at the electrode/electrolyte interface.

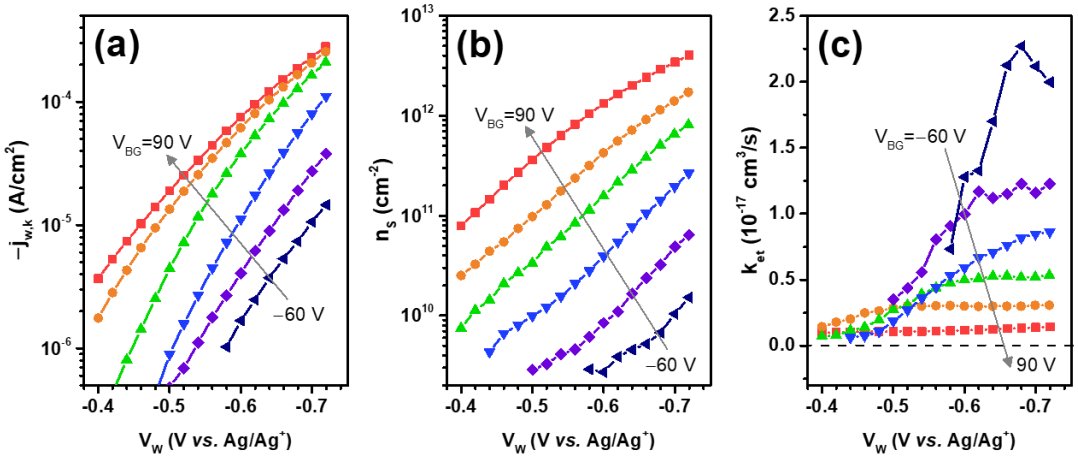

Figure 6.11. (a) Mass transport corrected reaction current density $j_{w,k}$ plotted vs. V_w for different V_{BG}. (b) Surface electron density n_s plotted vs V_w for different V_{BG}. (c) Rate constant k_{et}^- for TBBQ reduction on ZnO plotted vs V_w for different V_{BG}. V_{BG} values in (a-c) are adjusted from −60 to 90 V with 30 V intervals. Note that all data in this figure are calculated from the data shown in Figure 6.10.

The j_w in V_w<−0.4 V in Figure 6.10 is converted into $j_{w,k}$ using equation 6.9 and plotted vs. V_w in Figure 6.11a. Note that $j_{w,k}$ could not be calculated for V_w>−0.4 V because the background current from the non-passivated Au is not constant and thus hard to be corrected in the V_w regime. The sheet conductance (Figure 6.10b) obtained in the above analysis can be exploited to estimate the electron density n_s on the ZnO electrode, because the sheet conductance σ_s of the 2D electrode is given by:

$$\sigma_s = e\,\mu_e\,n_s + e\,\mu_h\,p_s \qquad (6.10)$$

where μ_e and μ_h are the mobilities of electrons and holes, respectively. Since the hole density p_s is essentially zero for the ZnO electrode, the hole conduction is negligible. Therefore, assuming the electron mobility μ_e has a constant value (~1.1 $cm^2\ V^{-1}\ s^{-1}$, estimated from the σ_s vs. V_{BG} curve in Figure 6.2) regardless of applied V_w and V_{BG}, n_s can be estimated from σ_s divided by $e\mu_e$ (Figure 6.11b). Then, k_{et}^- can also be obtained from $j_{w,k}$ divided by $-en_s c_{ox}^*$ at each data point (Figure 6.11c). Our result shows that n_s and k_{et}^- at a fixed V_{BG} generally increase with $-V_w$. The apparent exponential dependence of n_s with $-V_w$ is an expected behavior of an n-type semiconductor electrode, consistent with equation 6.9. On the other hand, at a fixed V_w, n_s increases by ~2 orders of magnitude with V_{BG} changing from -60 V to 90 V, while k_{et}^- generally decreases (down to 5% of initial value) at $V_w = -0.68$ V in the meantime. Overall, because n_s is more susceptible to V_{BG} than k_{et}^-, the reaction current density $j_{w,k}$ at a fixed V_w increases with V_{BG} (Figure 6.11a).

The observed trends of n_s and k_{et}^- at different V_w and V_{BG} can be better understood with the schematic energy diagrams shown in Figure 6.12, which show a specific case where V_w is fixed (more general diagrams can be found in Figure 5.8). Figure 6.12a depicts the initial state with V_{BG}=0 V, where δ_0 represents the initial offset of the CB edge from E_F. Figure 6.12b corresponds to the application of $V_{BG} > 0$ V while V_w is fixed. In this case, the CB edge has shifted via the field effect closer to E_F; the offset is now δ, and electron accumulation in the thin ZnO layer has occurred. Note that the V_{BG} induces charges not only in the ZnO electrode but also in the electric double layer. The vacuum level shift in the EDL due to V_{BG}-induced charge eventually leads to the band alignment shift at the electrode/electrolyte interface. In Chapter 5, we showed that the combination of the charge

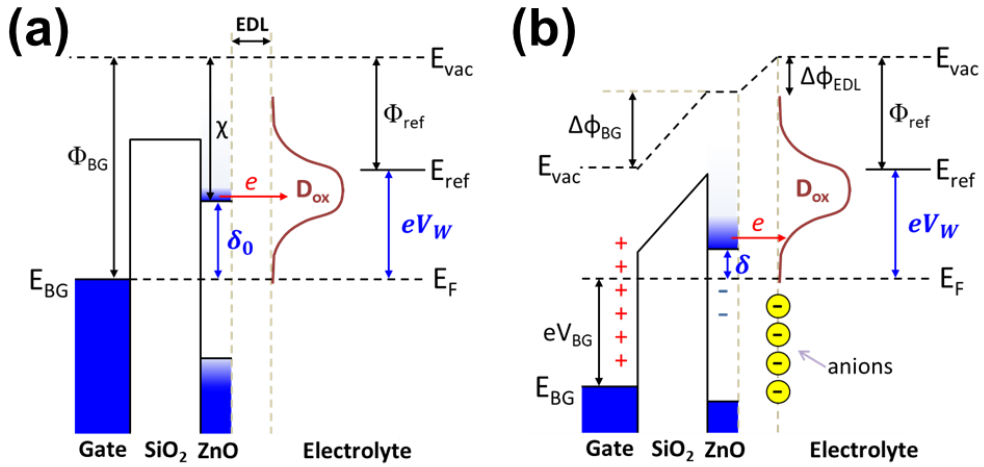

Figure 6.12. Energy diagrams of a back-gated 2D ZnO electrode in electrolyte (a) before and (b) after a positive V_{BG} is applied to the back gate while V_W is fixed. The red arrows indicate electron transfer processes. The additional symbols used in the diagram, which are not shown in Figure 6.8, are as follows: local vacuum level (E_{vac}); Fermi level of back gate (E_{BG}); work functions of back gate (Φ_{BG}) and RE (Φ_{ref}); electron affinity of ZnO (χ); vacuum level shifts in SiO_2 ($\Delta\phi_{BG}$) and EDL ($\Delta\phi_{EDL}$); energy distribution function of the oxidized species (D_{ox}).

balance and the energy balances gives the variation in the CB edge offset with respect to V_{BG} at a fixed V_w, namely:

$$\left(\frac{\partial\delta}{\partial V_{BG}}\right)_{V_w} = \frac{-e}{1+\frac{C_{EDL}}{C_{BG}}+\frac{C_W(\delta)}{C_{BG}}} \tag{6.11}$$

where C_{BG} and C_{EDL} are the back-gate and double-layer capacitances, respectively, and $C_W(\delta)$ is the quantum capacitance of the electrode given by:

$$C_W(\delta) = e\frac{dQ_W(\delta)}{d\delta} \tag{6.12}$$

Note that $C_W(\delta)$ essentially represents the DOS of the WE in capacitance units, which is a function of $\delta = E_c - E_F$. When E_F lies within the bandgap, $C_W(\delta)$ essentially becomes

zero if there are no surface trap states near the energy level. Considering the estimated C_{BG} (~20 nF/cm^2) is much smaller than the estimated C_{EDL} (~10 μF/cm^2), equation 6.12 is reduced to

$$\left(\frac{\partial \delta}{\partial V_{\mathrm{BG}}}\right)_{V_{\mathrm{w}}} \approx -e\frac{C_{\mathrm{BG}}}{C_{\mathrm{EDL}}} \approx -0.002\ e \tag{6.13}$$

Therefore, the band alignment shift that can be achieved with V_{BG} between -60 V to 90 V is estimated to be $\Delta\delta \approx -0.3$ eV. $\Delta\delta$ can be increased by preparing a gate dielectric layer with a higher dielectric constant or a reduced thickness.

Figure 6.12 also schematically shows how this V_{BG}-induced band alignment shift influences the charge transfer kinetics at the ZnO/electrolyte interface. In creating these diagrams, it is assumed the maximum of the energy distribution function of TBBQ ($D_{\mathrm{ox}}(E)$), which occurs at $E^{0'} + \lambda$ (Equation 2.14), is above the CB edge in most cases, based on the fact that $\lambda = \sim 0.76$ eV for TBBQ.[193] Note that only $D_{\mathrm{ox}}(E)$ is illustrated in the diagrams because practically anodic reaction does not occur in our system. Contrary to the DOS of the electrode $D(E)$, which can be freely shifted by V_{BG}, $D_{\mathrm{ox}}(E)$ is not subject to the field effect because the electric field from the back gate is completely screened outside the OHP by the abundant mobile ions in the electrolyte. As a result, V_{BG} can lead to a significant change in n_{s} and k_{et}^{-} at a given V_{w}. In Figure 6.12b, the CB edge shift to a lower energy level gives rise to an increased n_{s} (by equation 6.8) and a reduced energy states overlap (i.e., smaller k_{et}^{-}) between the $D(E)$ and $D_{\mathrm{ox}}(E)$ near the CB edge. This is consistent with the general trends observed in Figure 6.11b and 6.11c.

Lastly, it is noteworthy that the proposed model assuming an ideal n-type semiconductor electrode catches the essence of our observations but does not fully explain several behaviors including the response of k_{et}^{-} to V_{w}. Since the CB edge of an ideal n-type semiconductor is essentially *pinned* with respect to the reference energy E_{ref} (when V_{BG} is fixed), k_{et}^{-} in equation 6.5 should not be a function of V_{w}, which is contrary to our observation in Figure 6.11c. This abnormality is most likely attributed to the surface trap states of the ZnO electrodes prepared in this study. According to the physical model proposed in Chapter 5, the variation in the CB edge position with respect to V_{w} at a fixed V_{BG} is given by:

$$\left(\frac{\partial E_c}{\partial E_F}\right)_{V_{\mathrm{BG}}} = \frac{C_{\mathrm{BG}} + C_w(\delta)}{C_{\mathrm{EDL}} + C_{\mathrm{BG}} + C_w(\delta)} \tag{6.14}$$

If E_F lies within the bandgap and there are no surface trap states at the energy range, equation 6.14 becomes zero because $C_W(\delta)$ is zero and C_{BG} is much smaller than C_{EDL}. In other words, in an ideal n-type semiconductor having no surface trap states in the bandgap, E_c is essentially pinned with respect to the reference potential E_{ref} when V_W (i.e., E_F) is swept at a fixed V_{BG}. In reality, ZnO film grown by ALD is generally amorphous or polycrystalline, and has intrinsic surface states due to dangling bonds at Zn or O atoms at the surface or grain boundaries.[64] If the ZnO electrode has significant surface states so $C_w(\delta)$ is comparable to C_{EDL}, equation 6.14 would have a positive value and thus a positive sweep of E_F (i.e., a negative sweep of V_{w}) pushes up the CB edge to a higher energy level. This explains the trend observed in Figure 6.11c; k_{et}^{-} increases with $-V_{\mathrm{w}}$ as long as E_c is below the maximum of $D_{\mathrm{ox}}(E)$ at $E^{0\prime} + \lambda = 1.05$ eV vs. E_{ref}. The presence of the surface

states is also supported by the trend how n_s responds to V_w. According to equation 6.8, if E_c is pinned, $-V_w$ should increase by ~60 mV per decade increase of n_s. Therefore, ~150 mV increase in $-V_w$ per decade observed in Figure 6.11b suggests that a significant number of surface states on ZnO surface, which pushes up E_c during a positive sweep of E_F, comes in play at the ZnO/electrolyte interface.

6.5. Conclusion

In summary, we investigated continuous and reversible modulation of outer-sphere charge transfer kinetics on *gate-tunable* ZnO electrodes, in which the charge densities on the ultrathin ZnO surface and the EDL are controlled by a voltage bias applied to the *back gate*, as well as by its electrochemical potential set independently. A microfluidic channel integrated on this gate-tunable electrode allows one to conduct electrochemical measurements at a steady-state condition while mass transport effect, which introduces difficulties in analysis of reaction kinetics, is minimized. We observed that, at a given working electrode potential, the surface electron density n_s increases with the back gate bias (up to ~2 orders of magnitude), while the kinetic constant k_{et}^- generally decreases (down to 5% of initial value depending on the electrode potential) at the same time. Overall, the charge transfer rate at a given electrode potential increases at a positive back gate bias. Along with the Gerischer model, the observed trends of the kinetic parameters at different gate biases are consistent with our predictions; the transverse *field effect* induces band alignment shift at the electrode/electrolyte interface, which leads to the modulation of (1) charge carrier density at the electrode surface and (2) the energy overlap of empty and occupied states in the two phases at a given electrochemical potential. Although a simple

outer-sphere electrochemistry has been studied in the current investigation, the same concept can be potentially applied to control other interfacial phenomena, including inner-sphere charge transfer and surface binding of reaction species to the electrode. We believe that the system introduced here would be a useful research platform to investigate and optimize solid/liquid interfaces in various electrochemical systems including liquid junction solar cells, and (photo)electrocatalysts.

7. Outlook: Field Effect Modulation of Electrocatalytic Activity on 2D Electrodes

Based upon the results and the insight gained from this dissertation project, this chapter discusses the opportunities and the challenges expected in application of gate-tunable 2D electrodes for electrocatalysis, and proposes the strategies to overcome the hurdles. For the initial investigation to prove the concept, hydrogen evolution reaction (HER) on back-gated MoS_2 electrode is proposed as a model system. Other electrocatalytic systems that are potentially applicable to our devices are also briefly explored in the last section.

7.1. Electronic Structure: A Key Factor Determining Electrocatalytic Activities

As briefly discussed earlier in Section 2.4, activity of an electrocatalyst is ultimately determined by its surface electronic structure. Researchers have long investigated various types of electrocatalysts for different electrochemical reactions, and have found that the (electro)catalytic activities can be generally described by the several key *descriptors* (in terms of surface binding energies) of important reactants and reaction intermediates. This means that, on such electrocatalysts, the overall reaction rate is essentially limited by the sluggish surface binding and/or release steps, rather than the facile electron transfer steps. Taking hydrogen evolution reaction (HER) on a transition metal as an example, which is one of simplest electrocatalytic reactions where protons and electrons recombine to form molecular H_2 (i.e., $2H^+ + 2e \rightarrow H_2$), the activity is simply a function of the adsorption free energy of hydrogen ΔG_{H^*} as shown in the "volcano plot" in Figure 7.1a.[195–197] This makes sense considering the reaction pathway of HER, which is either the Volmer-

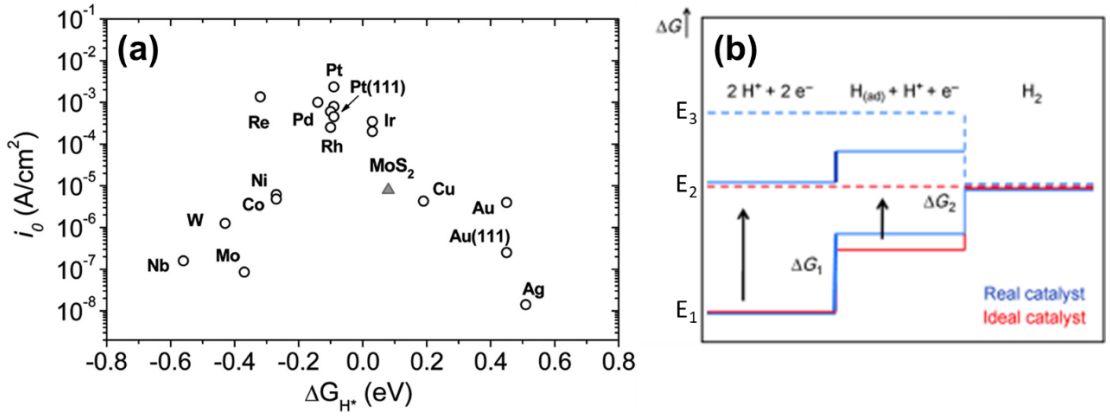

Figure 7.1. (a) Volcano plot of the exchange current density as a function of adsorption free energy of atomic hydrogen (b) Plot of Gibbs free energies of reaction species versus the reaction coordinate of the hydrogen evolution reaction (HER) via Volmer-Heyrovsky pathway. Dashed lines indicate energetics at the electrode potential where all thermochemical barriers disappear. [(a) is adapted from ref. 198 with permission; Copyright 2007 by the American Association for the Advancement of Science. (b) is reproduced from ref. 199 with permission; Copyright 2010 by Wiley-VCH]

Heyrovsky or the Volmer-Tafel mechanism described as follows, has H^* as the key reaction intermediate:[200]

$$\text{Volmer setp:} \quad H^+ + e + * \rightarrow H^*$$

$$\text{Heyrovsky step:} \quad H^* + H^+ + e \rightarrow H_2 + *$$

$$\text{Tafel step:} \quad 2H^* \rightarrow H_2 + *$$

where * denotes a binding site on the electrode surface. For an electrocatalyst to be an optimal electrode material for HER, the surface binding of H^* should not be too weak or too strong but be "just right" (Sabatier principle); if H^* is too weakly bound to the surface, the overall reaction rate is limited due to the slow Volmer step, and if H is too strongly bound, the rate is limited by desorption steps (i.e., Heyrovsky and Tafel steps).

Figure 7.1b. schematically shows the Gibbs free energy changes during Volmer-Heyrovsky reaction pathway on an ideal and a real electrocatalyst. Note that the Gibbs free

energies at the initial ($2H^+ + 2e$) and the intermediate ($H^* + H^+ + e$) states are functions of the electrode potential E, because the energy of electrons is determined by the electrode potential (i.e,, $\overline{\mu_e} = \mu_e - nFE$ where $\overline{\mu_e}$ and μ_e are the electrochemical potential and the chemical potential of the electrons, respectively; n is the number of electrons associated with the state; and F is the Faradaic constant). For HER to occur, each elementary step should be thermodynamically downhill process (i.e., both ΔG_1 and ΔG_2 should be ≤ 0 eV). As can be seen in the diagram, an ideal HER electrocatalyst should have ΔG_{H^*} of 0 eV at the equilibrium potential E_2 because it makes the whole reaction pathway a downhill process even at equilibrium. On the contrary, a real catalyst, which has $\Delta G_{H^*} > 0$ eV at E_2 in this example, the non-zero activation barrier in Volmer or Heyrovsky step prohibits HER to proceed at equilibrium; the overall reaction pathway becomes downhill at a more negative potential E_3. This explains why platinum, which has nearly zero adsorption free energy of hydrogen, is the best electrocatalyst for HER (Figure 7.1a).

The *d-band model*, which is developed by Hammer and Nørskov[50,201] and successfully applied to explain the trend of the adsorption free energy on different transition metal surfaces, gives an important insight to see the link between the electronic structures and the electrocatalytic activities of solids. Figure 7.2a schematically shows the formation of chemical bond due to electronic coupling between an adsorbate valence level and the *s* and *d* bands of a transition metal surface. The adsorbate state is first coupled with *s* band of the metal, giving rise to a shifted and broaden valence states. To a first approximation, this coupling effect is the same in all transition metals because they all have half-filled, very broad *s* bands. The 'renormalized' valence states are again coupled with

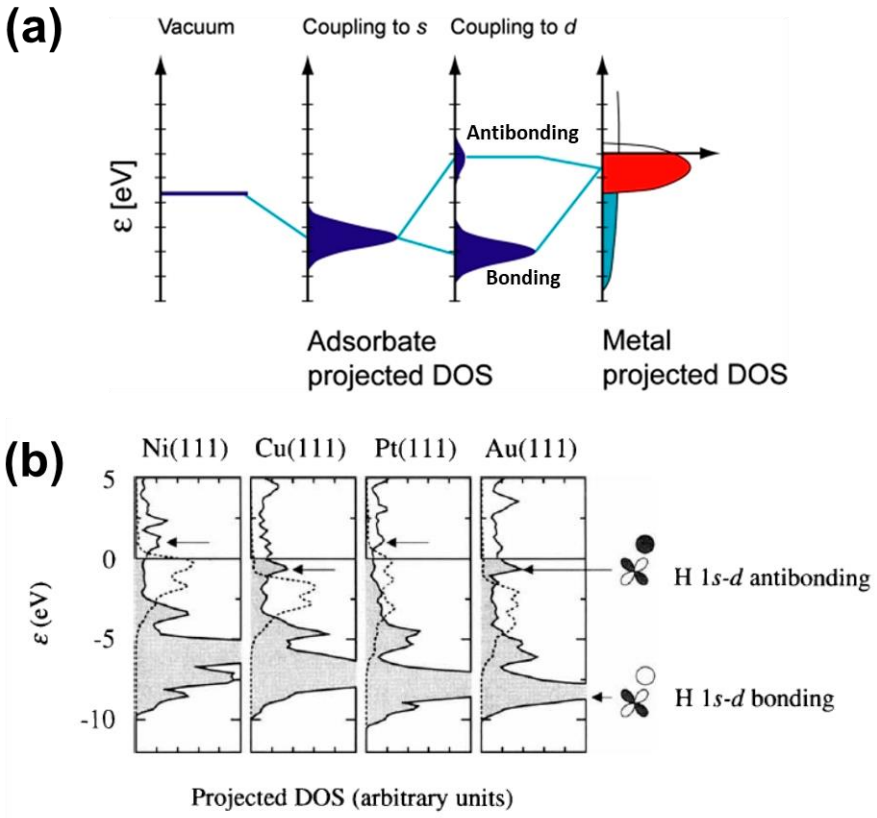

Figure 7.2. (a) Schematic illustration of the formation of a chemical bond between an adsorbate valence level and the *s* and *d* states of a transition metal surface (b) Density of states (DOS) for H atom adsorbed on (111) surface of transition metals. The solid lines indicate DOS projected on atomic H 1s state, and the dashed lines indicate DOS of *d* bands on clean metal surfaces. [(a) is reprinted from ref. 49 with permission; Copyright 2005 by Springer. (b) is reproduced from ref. 201 with permission; Copyright 1995 by the Nature Publishing Group]

d-band of the metal, generating bonding and antibonding states. The strength of the chemical bonding is determined by the Fermi level in the electrocatalyst because it is essentially the maximum energy level that the bonding and the antibonding states are filled up to. Considering the antibonding states are always formed above the d states, the energy of the *d*-band center with respect to the Fermi level is a good first *indicator* of the bond strength; the higher the *d*-band center is in energy relative to the Fermi level, the less the antibonding states are filled and thus the stronger the bond. Figure 7.2b shows the *d*-band

center is indeed a good indicator for transition metals; the H 1*s*-metal *d* antibonding peak on density of states (DOS) is right above the metal *d*-band, and the trend in H binding energies in Figure 7.1a is consistent with what *d*-band theory predicts. The metals (Ni and Pt) on which the antibonding states of H atoms are formed above the Fermi level exhibit strong H binding energies, while the metals (Cu and Au) with the antibonding states below the Fermi level exhibit relatively weak H binding energies.

In this section, we have seen that the surface electronic structure ultimately determines the activity of an electrocatalyst. Although only HER on transition metals is discussed as an example, the general principle applies to the other types of heterogeneous electrocatalysts for different reactions, while they often require, rather than a few simple indicators, more complicated *ab initio* calculation based on density function theory (DFT) to predict the correlation between surface binding energies and electrocatalytic activities.

7.2. Opportunities, Challenges, and Strategies

Opportunities. In light of the strong correlation between the surface electronic structure and the electrocatalytic activities on a solid, we reach a natural conclusion that electrocatalytic activities, as well as double layer structure and outer-sphere charge transfer kinetics, should be *gate-tunable*. If an electrode is an active electrocatalyst, there would be bonding and antibonding states associated with the surface-bound reaction species around the Fermi level. From Chapter 4 to 6, we have demonstrated that the energy bands of 2D semiconductors can be shifted with respect to the Fermi level, which is fixed at a given electrode potential, by a voltage bias applied to the back gate. If the same principle applies to the surface of a 2D electrocatalyst prepared on a back gate, it would be possible

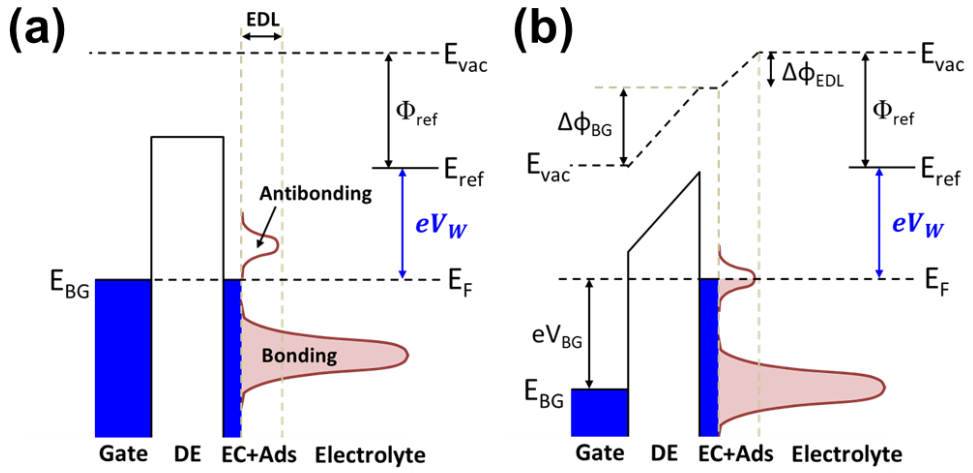

Figure 7.3. Energy diagrams of a back-gated 2D electrocatalyst (EC) in electrolyte (a) before and (b) after a positive back gate bias V_{BG} is applied while the working electrode potential V_W is fixed. Note that bonding and antibonding states are generated by electronic coupling between the electrocatalyst surface and adsorbates (Ads). The symbols used in the diagrams are as follows: gate dielectric (DE); local vacuum level (E_{vac}); Fermi level of back gate (E_{BG}); work function of reference electrode (Φ_{ref}); vacuum level shifts in SiO_2 ($\Delta\phi_{BG}$) and EDL ($\Delta\phi_{EDL}$).

to modulate the surface binding energies of reaction species by adding or removing electrons in the bonding or the antibonding states at a fixed electrode potential; this, in turn, will change the activities on the 2D electrocatalysts as discussed in the previous section. Figure 7.3 shows the energy diagrams in such a situation; in the given example, a positive gate bias V_{BG} at a fixed electrode potential shifts down the whole energy bands and fills more electrons in the antibonding states between the adsorbate and the electrocatalyst, leading to a weaker surface binding. A negative bias acts in the opposite way, resulting in a stronger surface binding.

Although it is not represented in the energy diagrams in Figure 7.3, it would be noteworthy that not only the band alignment shift with respect to the Fermi level but the bonding and the antibonding states themselves can be altered by the field effect. In contrast

to the outer-sphere redox species discussed in earlier chapters, reaction species on electrocatalysts are specifically adsorbed to the electrode surface and thus located at the inner Helmholtz plane (IHP), where the electric field is not completely cancelled out. Since the double layer structure is altered by the back-gate bias (Figure 7.3), the changes in electric field and ion-solvent interactions, as well as the energy alignment shift, would come in play in the field-effect modulation of surface binding energies. In this regard, a gate-tunable 2D electrode can serve a potentially useful "physical simulation" tool to investigate electrochemical interfaces, in which the double layer structure can be modified without changing the electrode potential or chemistry of the system.

In the theoretical investigations based on DFT, this *electric double layer effect* has been often ignored because (1) its contribution to free energy change is relatively small (~0.1-0.2 eV V^{-1})[200,202,203] compared to other terms, and (2) modeling a solid/electrolyte interface including charged surface, solvents, and ions is a very demanding task even with the modern computing power.[204] Nevertheless, for better description of electrocatalytic systems, theorists have tried to include solid/electrolyte interfaces in their models in several different approaches. Filhol and Neurock[205,206] developed the first methodology to deal with charged interfaces, so-called *double reference* method, in which charges are first placed in the system then balanced with a constant background charge. Nørskov et al.[207–209] modeled the electric double layer with a water bilayer, in which extra charges introduced by hydrogen atoms are balanced with the charge on the metal surface. In the models suggested by Jinnouchi and Anderson[210] as well as Otani et al.,[211] the double layer is described by Poisson-Boltzmann distribution of countercharge, which is combined by

DFT. Despite their great success in explaining some interfacial phenomena, a satisfactory method that can be generally applied to all electrochemical interfaces is yet to come. In this regard, a gate-tunable electrode may serve a complementary tool to develop and verify the *ab initio* methods dealing with charged interfaces.

Challenges. The greatest challenge expected in application of electrocatalytic systems to our devices is that most electrocatalysts have metallic electronic structures. This is because metallic conductivity is obviously one of most desired properties for good electrocatalysts. A solid with poor electronic conductivity is hardly a good electrocatalyst—even if it exhibits an optimal surface binding energy for a certain type of reaction—because the overall reaction rate in such a poor electronic conductor would be largely limited by the sluggish charge transport within the electrode. In the previous chapters, it has been shown that the band alignment shift that can be achieved by back gate bias V_{BG} at a fixed electrode potential V_w is given by:

$$\left(\frac{\partial \delta}{\partial V_{BG}}\right)_{V_w} = \frac{-e}{1 + \frac{C_{\mathrm{EDL}}}{C_{\mathrm{BG}}} + \frac{C_w(\delta)}{C_{\mathrm{BG}}}} \tag{7.1}$$

where δ is the conduction band edge offset from the Fermi level, and C_{BG}, C_{EDL}, and $C_W(\delta)$ are the back-gate, the double-layer, and electrode's quantum capacitances, respectively. This means, to induce a significant band alignment shift at a metallic surface that has a large DOS (i.e., $C_W(\delta)$) near the Fermi level, we need a huge C_{BG} (preferably) comparable to $C_W(\delta)$. Considering the result of the control experiment conducted with the redox species $Ru(bpy)_3^{2+}$ on ZnO electrode in Chapter 5, it is clear that our current SiO_2

back gate does not provide a sufficiently large capacitance to control the band alignment at metallic surfaces. Therefore, for a gate-tunable 2D electrode to be a truly versatile platform to modulate electrocatalytic activities on it, preparing new back gates with much higher capacitances is essential.

Strategies. First of all, to make electrocatalytic activities at a metallic surface *gate-tunable*, it is very important to prepare an atomically thin electrode. Thickness control is more critical issue in metallic electrodes than in semiconductor electrodes because metals intrinsically have higher numbers of energy states and mobile charge carriers near the Fermi level. Although the procedures to prepare such atomically thin films are highly material-specific, basic strategies would the same as those described in Section 2.2: either using intrinsic 2D materials or depositing ultrathin 3D material with precise thickness control.

Second, as discussed above, another important prerequisite for follow-up research is preparing back gates with higher capacitances. Simply speaking, this can be achieved by using high-k dielectric materials and reducing the thickness of the dielectric layer; the back gate capacitance C_{BG} is given by $C_{\mathrm{BG}} = \varepsilon\varepsilon_0/d$ where ε is the dielectric constant, ε_0 is the permittivity of free space, and d is the thickness of the gate dielectric. As can be seen from Table 7.1, the capacitance of the current 300 nm thick SiO_2 back gate can be greatly improved in this way. With a given dielectric material, the optimal thickness of the dielectric layer should be tuned such that the product of the capacitance and the breakdown voltage, i.e., maximum charge density that can be stored in the capacitor, is maximized. Among the candidate dielectric materials in Table 7.1, Na-β-Al_2O_3 looks particularly

promising material for the new gate dielectric because of its huge dielectric constant and large bandgap. The reason why Na-β-Al_2O_3 exhibits such a large dielectric constant is that it is actually a solid-state ionic conductor rather than a regular dielectric material. Like those in a liquid electrolyte, the mobile Na^+ ions in Na-β-Al_2O_3 generate an electric double layer at the electrode/Na-β-Al_2O_3 interface, exhibiting a huge capacitance.

Table 7.1. Static dielectric constant, experimental band gap of gate dielectrics[212–214]

Oxide	Dielectric Constant	Bandgap (eV)
SiO_2	3.9	9
Si_3N_4	7	5.3
Al_2O_3	9	8.8
Ta_2O_5	22	4.4
TiO_2	80	3.5
ZrO_2	25	5.8
HfO_2	25	5.8
$HfSiO_4$	11	6.5
La_2O_3	30	6
Y_2O_3	15	6
a-$LaAlO_3$	30	5.6
$SrTiO_3$	~300	3.2
Na β-Al_2O_3	~170	~8.8

It is believed that a uniform film of Na-β-Al_2O_3 can be prepared on a doped Si wafer (which serves a metallic gate) following the procedure reported in the previous work. Pal et al.[213] prepared crystalline (SBA1) and amorphous (SBA2) Na-β-Al_2O_3 films on indium-tin-oxide (ITO) glasses in two different methods: (1) a sol-gel route proposed by Yoldas,[215] in which sodium acetate and [$Al(OC_4H_9)_3$] are used as precursors, followed by spin-coating and 750^{o}C annealing, and (2) a spin-coating or dip coating process, in which

$Al(NO_3)_3$ and $NaHSO_3$ are used as precursors, followed by 200 ^oC annealing. 75 nm SBA1 film and 72 nm SBA2 film (with average roughness of ~1.15 nm from ref. 216) prepared by these methods showed low frequency (~50-500 Hz) capacitances of ~2.3 $\mu F/cm^2$ and ~3.6 $\mu F/cm^2$ with breakdown voltage of ~40 V and ~22 V, respectively. Therefore, the maximum charge densities that can be potentially induced with these films are $\sim 5.8 \times 10^{14}$ cm^{-2} and $\sim 5.0 \times 10^{14}$ cm^{-2}, respectively, which is ~2 orders higher charge density than that can be achieved with current SiO_2 back gate. To induce such a high charge density with a SiO_2 dielectric layer, electric field of ~230–270 MV/cm, which corresponds to ~7000-8000V for the current 300 nm thick SiO_2 back gate, would be necessary. This greatly exceeds the breakdown field of SiO_2 (~23–40 MV/cm).[217] Assuming monolayer Pt(111) film (atomic packing density: $\sim 1.5 \times 10^{15}$ cm^{-2} from ref. 218) is used as 2D electrocatalyst, the maximum charge density that can be induced by the proposed Na-β-Al_2O_3 back gate corresponds to ~0.4 electrons per Pt atom.

7.3. Field Effect Modulation of HER and HOR on 2D Electrodes

As discussed in Section 7.1, HER and HOR are the simplest types of electrocatalytic reactions that have been extensively studied for various electrocatalysts and thus are relatively well understood in general. Since only one surface species (i.e., surface adsorbed hydrogen atoms, H^*) would come in play in the overall HER or HOR pathways, it is relatively easy to analyze the reaction mechanisms and kinetics compared to other more complex electrocatalytic reactions. Accordingly, investigation of HER and HOR on gate-tunable 2D electrodes would be a reasonable starting point for follow-up research. Particularly, HER is of immediate interest because HER, in context of

experimental setup, is easier to investigate than HOR; the reactant of HER is simply an acid solution while that of HOR is H_2 dissolved in solution (e.g., by gas bubbling).

In principle, any currently available HER electrocatalysts are applicable to gate-tunable electrode structure as long as atomically thin smooth films for active electrodes can be prepared. Nevertheless, such film preparation is often challenging for 3D materials (MBE, mentioned in Section 3.2.1, is likely the only option). On the other hand, some of intrinsic 2D materials including graphene and MoS_2 can be relatively easily obtained with well-established film growth and transfer techniques. In this regard, such intrinsic 2D materials offer a great advantage over 3D materials in device fabrication. Several transition metal dichalcogenides (TMDs) including MoS_2 and WS_2, and N-, P-codoped graphene.[219] are 2D materials known to have HER activities. Among them, MoS_2 has been most vigorously studied during the last decade, because it exhibits a nearly optimal hydrogen binding energy (Figure 7.1a). On the other hand, MoS_2 has also attracted great attention as a 2D semiconductor for transistor devices due to its sizable bandgap (E_g=1.8 eV). Naturally, fundamental theories, electronic structures, materials properties, and experimental techniques for MoS_2 are quite well established. All things considered, we propose HER on back-gated MoS_2 electrodes as the first experimental system for follow-up research. Essentially the same device structure (i.e., gate-tunable electrochemical flow cell) and experimental techniques described in Section 3.5 and 6.3 can be applied for MoS_2-based devices, though device fabrication procedure should be slightly modified due to the new components: the MoS_2 film and the Na-β-Al_2O_3 back gate.

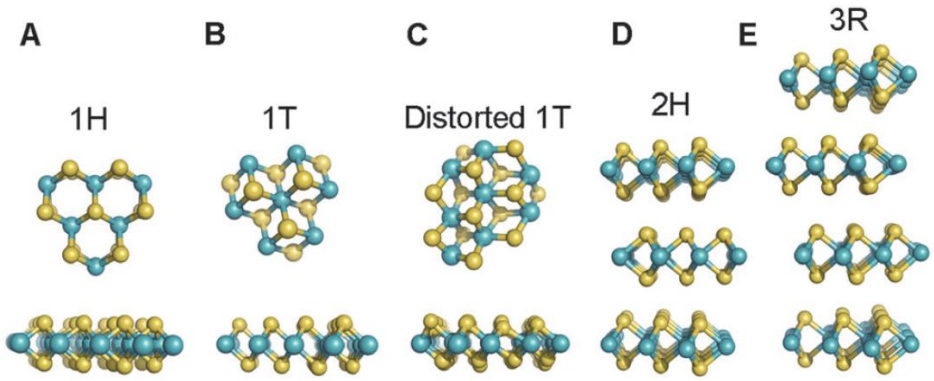

Figure 7.4. Different polymorphs or phases of single-layer and stacked single-layer transition metal dichalcogenides (TMDs): (A) 1H phase, (B) ideal (a × a) 1T phase, (C) distorted (2a × a) 1T phase, (D) 2H phase, and (E) 3R phase. [Adapted from ref. 220 with permission; Copyright 2015 by the Royal Society of Chemistry]

MoS_2 as Candidate Electrode Material. DFT calculation predicts the monolayer 1H-MoS_2 as an active electrocatalyst for HER as its ΔG_{H^*} is 0.08 eV, close to the optimal value 0 eV, for the Mo-terminated zigzag edges.[221] Hydrogen atoms are bound to every second S atoms at the edge (i.e., 50% coverage) while the basal plane is catalytically inactive (ΔG_{H^*}=1.92 eV). Jaramillo et al.[198] experimentally verified that the active sites for HER by establishing the direct correlation between the HER activities and the density of 1H-MoS_2 prepared on Au substrate; the linear dependence between exchange current density and the MoS_2 edge length (rather than the MoS_2 area coverage) confirms the active sites are at the edges, not on basal plane. As a strategy to increase the activity of the basal plane, phase engineering has been proposed; lithium intercalation into bulk 2H-MoS_2 leads to chemical exfoliation accompanied by phase transformation into 1T-MoS_2.[25,26,222,223] The resulting 1T-MoS_2 exhibits metallic properties[224] and greatly improved HER activities with Tafel slope of ~40 mV/decade.[225,226] While Lukowski et al.[225] attributed the enhanced HER activity to the increase in number of active edge sites and the decrease in charge transfer resistance, Voiry et al.[226] claims that the basal plane of 1T-MoS_2 are catalytically active

while the edges are not. A recent DFT calculation[227] proposes that the S atoms on basal plane of 1T-MoS_2 are active H binding sites. It has been reported that phase transformation from 2H- to 1T-WS_2 also greatly enhances HER activities.[228,229]

Doping transition metal atoms including Fe, Co and Ni into MoS_2 can be another effective strategy to increase HER activity.[230,231] A scanning tunneling microscopy (STM) study has revealed that the dopants are located predominantly at the S-terminated edges (S-edges), modifying the hydrogen binding energy.[232] DFT calculation shows that incorporation of Co dopants modifies ΔG_{H^*} at S-edges from 0.18 eV (undoped MoS_2) to 0.10 eV, while ΔG_{H^*} at Mo-edges (0.08 eV) is unaffected.[233]

An interesting prediction from DFT calculations is that H binding at the edge sites and the basal plane of 1H-MoS_2 can be modified by substrate interaction.[234–236] The change in H binding is attributed to the van der Waals interaction with the substrate, and a strong interaction can result in several orders of magnitude difference in HER turnover frequency (TOF). The authors proposed the physisorption strength between MoS_2 and the substrate should be approximately −0.30 eV for optimal HER activity.[235] Since MoS_2 on graphene is expected to have ΔG_{H^*} of approximately −0.25 eV, it is expected to have ~2-3 orders lower exchange current of HER compared MoS_2 prepared on the optimal substrate. As discussed in Chapter 4, graphene is transparent, though not completely, to the electric field from the back gate; the EDL beyond graphene can be altered by the back gate bias at a fixed electrode potential. Therefore, MoS_2 on graphene is also expected to be *gate-tunable*, though the increased quantum capacitance would somewhat limit the extent of band alignment shift. In this regard, HER on a back-gated MoS_2/graphene electrode would be

also an interesting experimental system to investigate in follow-up research. The devices could be prepared by transferring an epitaxial MoS_2/graphene film[237,238] to the back gate. Since graphene has a superior electronic conductivity even at the Dirac point, we expect the in-plane polarization issue in the experiments can be effectively avoided in this system.

Preliminary Results from Other Group. Recently, Wang et al.[60] reported that HER activities on MoS_2 nanosheets can be greatly enhanced by the field effect. The authors used mechanically exfoliated MoS_2 films and employed essentially the same device structure to ours for CV analysis. They observed the overpotential at current density of 100 mA cm^{-2}, which was initially 240 mV at back gate bias of 0 V, is reduced to 38 mV at back gate bias of 5 V. Despite the inspiring results, we have found that the devices were not properly designed in that the MoS_2 channel between the two metal contacts is not fully exposed to the solution, and this led the authors to a potentially wrong conclusion. With their device design, overall reaction rate can be limited by the resistance of the 'unexposed' channel area where carrier transport can be 'tuned off' by the back gate bias—note that MoS_2 is an n-type semiconductor with a bandgap of 1.8 eV. The channel conductivity in their report, which only responds to the back gating but not to electrolyte gating, indicates that the reaction current is simply regulated by the 'switch' at the unexposed channel area. For the HER activity on MoS_2 to be truly gate-tunable, the entire channel area should contact the electrolyte as illustrated in Section 3.2.2. While the previous report simply attributed the enhanced HER activity to the increased electronic conductance of MoS_2, it still needs more investigations to figure out how the hydrogen binding energy and HER activity on MoS_2 are influenced by the field effect.

7.4. More Electrocatalytic Reactions Beyond HER and HOR

Although HER/HOR on 2D electrocatalysts are proposed as model systems for initial investigation, application of the back-gated 2D electrode structure is not limited to HER and HOR. In this section, other electrocatalytic systems that can be potentially applied to our devices are briefly explored.

Oxygen Reduction/Evolution Reactions. Although oxygen reduction reaction (ORR) and oxygen evolution reaction (OER) occur in similar ways to HER and HOR in that they are also essentially governed by surface binding energies of reaction species, their reaction mechanisms are much more complicated than HER and HOR. ORR generally involves either four-electron transfer, which is desirable pathway for fuel cells, or two-electron transfer, which might be attractive for industrial H_2O_2 production, as shown in Table 7.2.

Table 7.2. ORR reaction pathways in acidic and alkaline solutions.

Electrolyte	Reactions
Acidic	$O_2 + 4H^+ + 4e \rightarrow H_2O$
	$O_2 + 2H^+ + 2e \rightarrow H_2O_2$
	$H_2O_2 + 2H^+ + 2e \rightarrow 2H_2O$
Alkaline	$O_2 + H_2O + 4e \rightarrow 4OH^-$
	$O_2 + H_2O + 2e \rightarrow OOH^- + OH^-$
	$OOH^- + H_2O + 2e \rightarrow 3OH^-$

The four-electron pathway can proceed via several different mechanisms. For example, in acidic solution, a direct four-electron pathway can be either dissociative or associative, depending on the oxygen dissociation barrier on the electrocatalyst surface:[239]

Dissociative: $O_2 + 2* + 4e \rightarrow 2O^*$

$2O^* + 2H^+ + 2e \rightarrow 2OH^*$

$2OH^* + 2H^+ + 2e \rightarrow 2H_2O + 2*$

Associative: $O_2 + * \rightarrow {O_2}^*$

${O_2}^* + H^+ + e \rightarrow OOH^*$

$OOH^* + H^+ + e \rightarrow O^* + H_2O$

$O^* + H^+ + e \rightarrow OH^*$

$OH^* + H^+ + e \rightarrow H_2O + *$

In an indirect four-electron pathway, H_2O_2 is first generated via two-electron pathway, and then further reduced to water via another two-electron transfer (detailed reaction steps are not shown here). In contrast to HER, more than one surface species (i.e., O^*, OH^*, ${O_2}^*$, OOH^*) can be involved in the overall reaction pathway. On close-packed metal surfaces, ORR activity and adsorption free energy of O^* (ΔG_{O^*}) shows 'volcano' type relationship as in HER (Figure 7.5a). It should be noted, however, that this simple relationship arises not because O^* is the only important surface species, but because surface binding energies of the surface species are strongly correlated and cannot be easily decoupled, following *scaling relations* (Figure 7.5b).[240,241] Since independent tuning of the surface binding energies is largely prohibited due to the scaling relations, even an electrocatalyst having an optimal ΔG_{O^*} in the volcano plot has a nonzero theoretical overpotential of 0.3 to 0.4 V.[63,240,241]

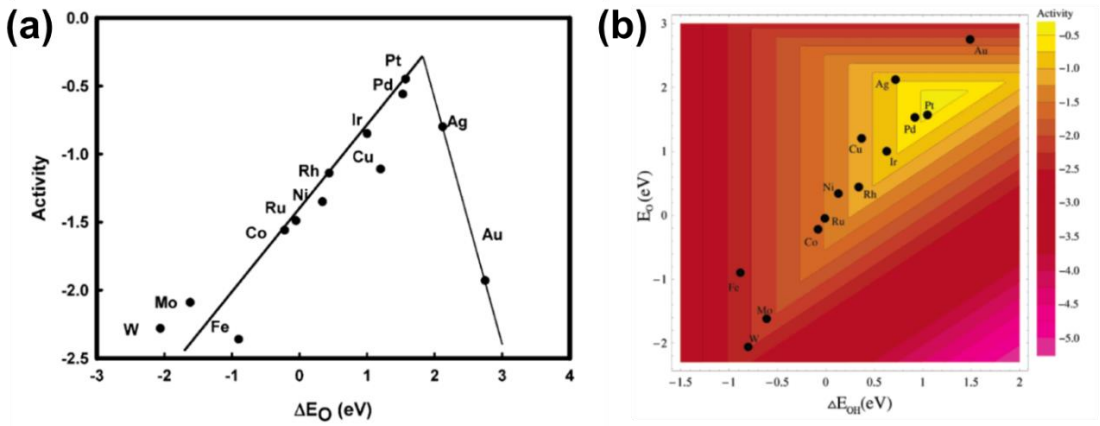

Figure 7.5. (a) Volcano plot of ORR activity versus oxygen binding energy. (b) ORR activities plotted as a function of both the O^* and the OH^* binding energies. Note that a strongly linear correlation between the O^* and the OH^* binding energies is found in (b). [Reproduced with permission from ref. 203; Copyright 2004 by the American Chemical Society]

Although currently available ORR catalysts are largely limited to precious metals (Pt and Pd) and their alloys (with Ni, Fe, Co, Cu, etc), non-precious metal compounds including (i) metal-N_4 organometallic complexes (M-N_4, M=Co, Fe) with or without carbon support; and (ii) metals coupled with nitrogen-containing carbon materials (M-N_x/C, M=Co, Fe, Ni, Mn) are also known to exhibit ORR activities.[200] Graphene derivatives[242,243] (doped with heteroatoms, especially N-doped graphene) are also promising non-precious metal ORR electrocatalysts. Heteroatom doping of graphene can be achieved by various synthesis or modification methods including CVD, thermal annealing, plasma, photochemistry, arc-discharge, etc.[243] In general, the enhanced ORR activities are attributed to electronegativity of the heteroatoms, which creates charged active sites favorable for oxygen adsorption while the rich π electrons in graphene are utilized for oxygen reduction.[244] Despite its relatively low TOF compared to Pt-based catalysts, N-doped graphene has been received great attention as ORR electrocatalyst because it is made

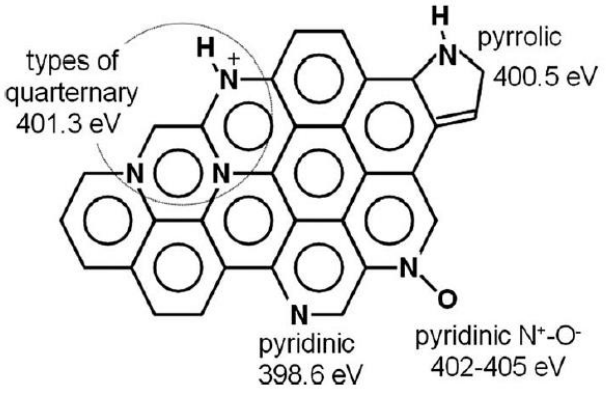

Figure 7.6. Nitrogen species commonly found in nitrogen-containing carbons. The energies indicate the peak positions in XPS spectra. [Adapted from ref. 245 with permission; Copyright 2006 by Elsevier Inc.]

from abundant elements (C and N) and it has an excellent tolerance to CO poisoning which is a notorious drawback of Pt-based catalysts. While N-doped graphene has three main types of N sites (graphitic N, pyridinic N and pyrrolic N structures shown in Figure 7.6)[246] that can potentially generate the active sites, it is still controversial which N-sites produce the improved ORR activity.[242] Recently, Song and coworkers reported that oxygen incorporated and P-doped MoS_2 nanosheets are also active electrocatalysts for ORR.[247,248] Given that heteroatom-doped graphene and MoS_2 can be prepared as 2D film appropriate for device fabrication, investigating their ORR kinetics on back-gated structure would be another interesting topic for follow-up research.

Most common OER electrocatalysts are transition metal oxides. While rutile-type RuO_2 shows the highest OER activity among metal oxides, it suffers from weak stability under acidic condition; at a high potential (> 1.4 V), RuO_2 at the surface is oxidized into dissolvable RuO_4 and loses OER activity.[249,250] Accordingly, IrO_2, which shows a slightly higher overpotential than RuO_2 but is stable under operating potential up to ~2.0 V, has

been employed as an alternative OER electrode.[200] Among non-precious metal oxides, Ni-, Co-, and Mn-based oxides have been widely studied for OER catalysts.[200,239] The DFT study conducted by Man *et al.*[66] shows the universal relationship between the adsorption energies of key intermediate species (*O and *OH) and the OER activities on various oxide surfaces, which excellently agrees with the experimental results (Figure 7.7).

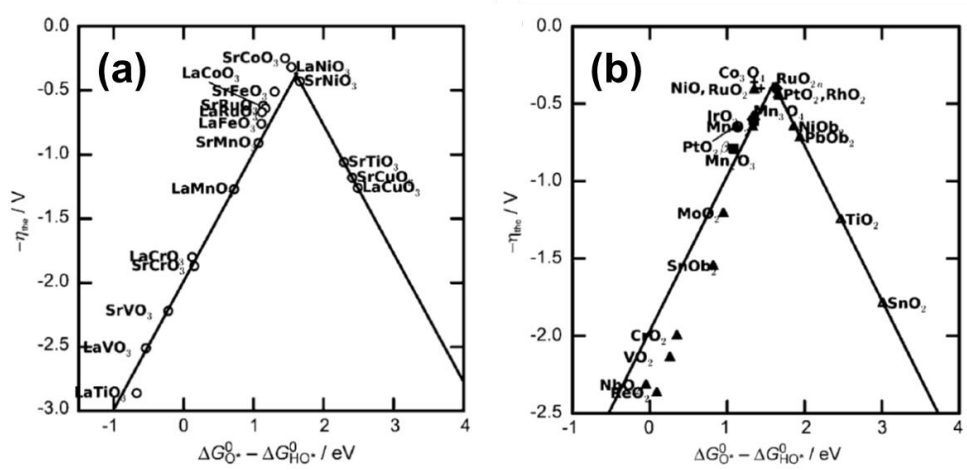

Figure 7.7. (a) Trends of ORR activity for (a) perovskites and (b) rutile, anatase, Co_3O_4, $Mn_x\ O_y$ oxides plotted against the standard free energy of the $\Delta G_{O^*} - \Delta G_{HO^*}$ [Adapted from ref. 66 with permission; Copyright 2011 by Wiley-VCH.]

On the other hand, possibilities of 2D materials as OER catalysts have been actively explored these days. Layered double hydroxides (LDHs),[251,252] which consist of positively charged layers and weakly bounded charge-balancing anions or solvation molecules and interlayer water molecules, is gaining popularity as promising alternatives of conventional OER catalysts for alkaline media. Song et al. reported Co-Mn LDH nanosheets exhibit ~9 times higher TOF than IrO_2 catalyst.[252] By exchanging the interlayer anions in a liquid phase, LDH can be exfoliated into nanosheets of single to several atomic layers.[251] Zn-Co LDH grown on reduced graphene oxide (rGO) has also been reported.[253] Some TMDs

including ZrS_3, Co_3S_4, and $CoSe_2$ nanosheets showed good OER activities,[254–257] though they tend to be easily oxidized during operations.[219]

Other Electrocatalytic Reactions on 2D Materials. Recently, anisotropic sysnthesis of ultrathin 2D metal nanosheets has been achieved,[258–261] and their possibilities as electrocatalysts have been explored. Among them, Pd nanosheet (~10 atomic layers) exhibited ~2.5 times higher electrocatalytic activity for the oxidation of formic acid compared to commercial Pd black catalyst.[259] Partially oxidized Co nanosheets (~4 atomic layers) were found to be an active electrocatalyst for CO_2 reduction which produces formate ($HCOO^-$) with 90% selectivity in aqueous solution at a lower overpotential than bulk metal or oxide electrodes.[262] The edge sites of MoS_2 have been found to serve a robust CO_2 reduction catalyst outperforming noble metal electrode.[263]

8. Bibliography

(1) Neamen, D. A. *Semiconductor Physics and Devices: Basic Principles*; 4th ed.; McGraw-Hill, 2012.
(2) Mikheeva, E. P. *Russ. Chem. Rev.* **1989**, *58*, 517.
(3) Zhang, Y.; Kolmakov, A.; Chretien, S.; Metiu, H.; Moskovits, M. *Nano Lett.* **2004**, *4*, 403.
(4) Baker, L. R.; Hervier, A.; Kennedy, G.; Somorjai, G. A. *Nano Lett.* **2012**, *12*, 2554.
(5) Zaumseil, J.; Sirringhaus, H. *Chem. Rev.* **2007**, *107*, 1296.
(6) Galiński, M.; Lewandowski, A.; Stępniak, I. *Electrochim. Acta* **2006**, *51*, 5567.
(7) Shimotani, H.; Asanuma, H.; Tsukazaki, A.; Ohtomo, A.; Kawasaki, M.; Iwasa, Y. *Appl. Phys. Lett.* **2007**, *91*, 82106.
(8) Yuan, H.; Shimotani, H.; Tsukazaki, A.; Ohtomo, A.; Kawasaki, M.; Iwasa, Y. *Adv. Funct. Mater.* **2009**, *19*, 1046.
(9) Lee, M.; Williams, J. R.; Zhang, S.; Frisbie, C. D.; Goldhaber-Gordon, D. *Phys. Rev. Lett.* **2011**, *107*, 256601.
(10) Xie, W.; Frisbie, C. D. *J. Phys. Chem. C* **2011**, *115*, 14360.
(11) Kim, S. H.; Hong, K.; Xie, W.; Lee, K. H.; Zhang, S.; Lodge, T. P.; Frisbie, C. D. *Adv. Mater.* **2013**, *25*, 1822.
(12) Lee, K. H.; Kang, M. S.; Zhang, S.; Gu, Y.; Lodge, T. P.; Frisbie, C. D. *Adv. Mater.* **2012**, *24*, 4457.
(13) Lee, K. H.; Zhang, S.; Gu, Y.; Lodge, T. P.; Frisbie, C. D. *ACS Appl. Mater. Interfaces* **2013**, *5*, 9522.
(14) Moon, H. C.; Lodge, T. P.; Frisbie, C. D. *J. Am. Chem. Soc.* **2014**, *2014*.
(15) Moon, H. C.; Lodge, T. P.; Frisbie, C. D. *Chem. Mater.* **2015**, *27*, 1420.
(16) Moon, H. C.; Kim, C. H.; Lodge, T. P.; Frisbie, C. D. *ACS Appl. Mater. Interfaces* **2016**, *8*, 6252.
(17) Munje, R. D.; Muthukumar, S.; Jagannath, B.; Prasad, S. *Sci. Rep.* **2017**, *7*, 1950.
(18) Wang, X.; Hao, J. *Sci. Bull.* **2016**, *61*, 1281.
(19) Colinge, J. P. *Solid. State. Electron.* **2004**, *48*, 897.
(20) Ferain, I.; Colinge, C. A.; Colinge, J.-P. *Nature* **2011**, *479*, 310.
(21) Chhowalla, M.; Jena, D.; Zhang, H. *Nat. Rev. Mater.* **2016**, *1*, 16052.
(22) Huang, Y.; Sutter, E.; Shi, N. N.; Zheng, J.; Yang, T.; Englund, D.; Gao, H. J.; Sutter, P. *ACS Nano* **2015**, *9*, 10612.
(23) Li, H.; Wu, J.; Yin, Z.; Zhang, H. *Acc. Chem. Res.* **2014**, *47*, 1067.
(24) Yuan, L.; Ge, J.; Peng, X.; Zhang, Q.; Wu, Z.; Jian, Y.; Xiong, X.; Yin, H.; Han, J. *AIP Adv.* **2016**, *6*.
(25) Kim, J.; Kwon, S.; Cho, D.-H.; Kang, B.; Kwon, H.; Kim, Y.; Park, S. O.; Jung, G. Y.; Shin, E.; Kim, W.-G.; Lee, H.; Ryu, G. H.; Choi, M.; Kim, T. H.; Oh, J.; Park, S.; Kwak, S. K.; Yoon, S. W.; Byun, D.; Lee, Z.; Lee, C. *Nat. Commun.* **2015**, *6*, 8294.
(26) Tao, H.; Zhang, Y.; Gao, Y.; Sun, Z.; Yan, C.; Texter, J. *Phys. Chem. Chem. Phys.* **2017**, *19*, 921.

(27) Yu, J.; Li, J.; Zhang, W.; Chang, H. *Chem. Sci.* **2015**, *6*, 6705.
(28) Bhimanapati, G. R.; Lin, Z.; Meunier, V.; Jung, Y.; Cha, J.; Das, S.; Xiao, D.; Son, Y.; Strano, M. S.; Cooper, V. R.; Liang, L.; Louie, S. G.; Ringe, E.; Zhou, W.; Kim, S. S.; Naik, R. R.; Sumpter, B. G.; Terrones, H.; Xia, F.; Wang, Y.; Zhu, J.; Akinwande, D.; Alem, N.; Schuller, J. A.; Schaak, R. E.; Terrones, M.; Robinson, J. A. *ACS Nano* **2015**, *9*, 11509.
(29) Bolotin, K. I.; Sikes, K. J.; Jiang, Z.; Klima, M.; Fudenberg, G.; Hone, J.; Kim, P.; Stormer, H. L. *Solid State Commun.* **2008**, *146*, 351.
(30) Castro Neto, A. H.; Peres, N. M. R.; Novoselov, K. S.; Geim, A. K. *Rev. Mod. Phys.* **2009**, *81*, 109.
(31) Schwierz, F. *Nat. Nanotechnol.* **2010**, *5*, 487.
(32) Hwang, W. S.; Zhao, P.; Tahy, K.; Nyakiti, L. O.; Wheeler, V. D.; Myers-Ward, R. L.; Eddy, C. R.; Gaskill, D. K.; Robinson, J. A.; Haensch, W.; Xing, H.; Seabaugh, A.; Jena, D. *APL Mater.* **2015**, *3*.
(33) Fang, T.; Konar, A.; Xing, H.; Jena, D. *Phys. Rev. B - Condens. Matter Mater. Phys.* **2008**, *78*, 1.
(34) Xu, M.; Liang, T.; Shi, M.; Chen, H. *Chem. Rev.* **2013**, *113*, 3766.
(35) Chhowalla, M.; Shin, H. S.; Eda, G.; Li, L.-J.; Loh, K. P.; Zhang, H. *Nat. Chem.* **2013**, *5*, 263.
(36) Fiori, G.; Bonaccorso, F.; Iannaccone, G.; Palacios, T.; Neumaier, D.; Seabaugh, A.; Banerjee, S. K.; Colombo, L. *Nat. Nanotechnol.* **2014**, *9*, 768.
(37) Schwierz, F.; Pezoldt, J.; Granzner, R. *Nanoscale* **2015**, *7*, 8261.
(38) Radisavljevic, B.; Radenovic, A.; Brivio, J.; Giacometti, V.; Kis, A. *Nat. Nanotechnol.* **2011**, *6*, 147.
(39) Manfra, M. J. *Annu. Rev. Condens. Matter Phys.* **2014**, *5*, 347.
(40) Ko, H.; Takei, K.; Kapadia, R.; Chuang, S.; Fang, H.; Leu, P. W.; Ganapathi, K.; Plis, E.; Kim, H. S.; Chen, S.-Y.; Madsen, M.; Ford, A. C.; Chueh, Y.-L.; Krishna, S.; Salahuddin, S.; Javey, A. *Nature* **2010**, *468*, 286.
(41) Cheng, K. Y. *J. Vac. Sci. Technol. A Vacuum, Surfaces, Film.* **2013**, *31*, 50814.
(42) George, S. M. *Chem. Rev.* **2010**, *110*, 111.
(43) Niinistö, L.; Päiväsaari, J.; Niinistö, J.; Putkonen, M.; Nieminen, M. *Phys. Status Solidi Appl. Res.* **2004**, *201*, 1443.
(44) Langereis, E.; Heil, S. B. S.; Knoops, H. C. M.; Keuning, W.; van de Sanden, M. C. M.; Kessels, W. M. M. *J. Phys. D. Appl. Phys.* **2009**, *42*, 73001.
(45) Park, S.-H. K.; Hwang, C.-S.; Jeong, H. Y.; Chu, H. Y.; Cho, K. I. *Electrochem. Solid-State Lett.* **2008**, *11*, H10.
(46) Johnson, R. W.; Hultqvist, A.; Bent, S. F. *Mater. Today* **2014**, *17*, 236.
(47) Ahn, C. H.; Kong, B. H.; Kim, H.; Cho, H. K. *J. Electrochem. Soc.* **2011**, *158*, H170.
(48) Imbihl, R. *Prog. Surf. Sci.* **2010**, *85*, 241.
(49) Nilsson, A.; Pettersson, L. G. M.; Hammer, B.; Bligaard, T.; Christensen, C. H.; Nørskov, J. K. *Catal. Letters* **2005**, *100*, 111.
(50) Nørskov, J. K.; Abild-Pedersen, F.; Studt, F.; Bligaard, T. *Proc. Natl. Acad. Sci. U. S. A.* **2011**, *108*, 937.

(51) Nørskov, J. K.; Bligaard, T.; Rossmeisl, J.; Christensen, C. H. *Nat. Chem.* **2009**, *1*, 37.
(52) Neophytides, S. G.; Vayenas, C. G. *J. Phys. Chem.* **1995**, *99*, 17063.
(53) Ladas, S.; Kennou, S.; Bebelis, S.; Vayenas, C. G. *J. Phys. Chem.* **1993**, *97*, 8845.
(54) Basini, L.; Cavalca, C. A.; Haller, G. L. *J. Phys. Chem.* **1994**, *98*, 10853.
(55) Ladas, S.; Bebelis, S.; Vayenas, C. G. *Surf. Sci.* **1991**, *251–252*, 1062.
(56) Neophytides, S. G.; Tsiplakides, D.; Stonehart, P.; Jaksic, M.; Vayenas, C. G. *J. Phys. Chem.* **1996**, *100*, 14803.
(57) Neophytides, S.; Tsiplakides, D.; Stonehart, P.; Jaksic, M. M.; Vayenas, C. G. *Nature* **1994**, *370*, 45.
(58) Maximoff, S. N.; Head-Gordon, M. P. *Proc. Natl. Acad. Sci. U. S. A.* **2009**, *106*, 11460.
(59) Kim, C.; Frisbie, C. D. *J. Am. Chem. Soc.* **2016**, *138*, 7220.
(60) Wang, J.; Yan, M.; Zhao, K.; Liao, X.; Wang, P.; Pan, X.; Yang, W.; Mai, L. *Adv. Mater.* **2017**, *29*, 1.
(61) Bard, A. J.; Faulkner, L. R. *Electrochemical Methods: Fundamentals and Applications*; 2nd ed.; Wiley: New York, 2006.
(62) Zheng, Y.; Jiao, Y.; Jaroniec, M.; Qiao, S. Z. *Angew. Chemie - Int. Ed.* **2015**, *54*, 52.
(63) Sheng, W.; Gasteiger, H. A.; Shao-Horn, Y. *J. Electrochem. Soc.* **2010**, *157*, B1529.
(64) Morrison, S. R. *Electrochemistry at Semiconductor and Oxidized Metal Electrodes*; Plenum Press: New York, 1980.
(65) Sato, N. *Electrochemistry at Metal and Semiconductor Electrodes*; Elsevier B.V., 1998.
(66) Man, I. C.; Su, H.-Y.; Calle-Vallejo, F.; Hansen, H. A.; Martínez, J. I.; Inoglu, N. G.; Kitchin, J.; Jaramillo, T. F.; Nørskov, J. K.; Rossmeisl, J. *ChemCatChem* **2011**, *3*, 1159.
(67) Conway, B.; Jerkiewicz, G. *Electrochim. Acta* **2000**, *45*, 4075.
(68) Oelßner, W.; Berthold, F.; Guth, U. *Mater. Corros.* **2006**, *57*, 455.
(69) Britz, D. *J. Electroanal. Chem.* **1978**, *88*, 309.
(70) Gerischer, H. In *Physical Chemistry: An Advanced Treatise Vol. 9A*; Eyring, H.; Henderson, D.; Yost, W., Eds.; Academic: New York, 1970; pp. 463–542.
(71) Nozik, A. J.; Memming, R. *J. Phys. Chem.* **1996**, *100*, 13061.
(72) Memming, R. *Comprehensive Treatise of Electrochemistry*; Conway, B. E.; Bockris, J. O.; Yeager, E.; Khan, S. U. M.; White, R. E., Eds.; Springer US: Boston, MA, 1983.
(73) Memming, R. *Semiconductor Electrochemistry*; Wiley-VCH: Weinheim, 2001.
(74) Lee, C.-W.; Hwu, J.-G. *AIP Adv.* **2013**, *3*, 102123.
(75) Suné, J.; Olivo, P.; Riccó, B. *IEEE Trans. Electron Devices* **1992**, *39*.
(76) Suk, J. W.; Kitt, A.; Magnuson, C. W.; Hao, Y.; Ahmed, S.; An, J.; Swan, A. K.; Goldberg, B. B.; Ruoff, R. S. *ACS Nano* **2011**, *5*, 6916.
(77) Tuinstra, F. *J. Chem. Phys.* **1970**, *53*, 1126.
(78) Ferrari, A. C.; Robertson, J. *Phys. Rev. B* **2000**, *61*, 14095.

(79) Thomsen, C.; Reich, S. *Phys. Rev. Lett.* **2000**, *85*, 5214.
(80) Malard, L. M.; Pimenta, M. A.; Dresselhaus, G.; Dresselhaus, M. S. *Phys. Rep.* **2009**, *473*, 51.
(81) Ferrari, A. C.; Meyer, J. C.; Scardaci, V.; Casiraghi, C.; Lazzeri, M.; Mauri, F.; Piscanec, S.; Jiang, D.; Novoselov, K. S.; Roth, S.; Geim, A. K. *Phys. Rev. Lett.* **2006**, *97*, 1.
(82) Kim, K.; Coh, S.; Tan, L. Z.; Regan, W.; Yuk, J. M.; Chatterjee, E.; Crommie, M. F.; Cohen, M. L.; Louie, S. G.; Zettl, a. *Phys. Rev. Lett.* **2012**, *108*, 246103.
(83) Tynell, T.; Karppinen, M. *Semicond. Sci. Technol.* **2014**, *29*, 43001.
(84) Tompkins, H. G.; McGahan, W. A. *Spectroscopic Ellipsometry and Reflectometry: A User's Guide*; John Wiley & Sons, Inc.: New York, 1999.
(85) Kohl, P. A.; Bard, A. J. *J. Am. Chem. Soc.* **1977**, *99*, 7531.
(86) Nicholson, R. S. *Anal. Chem.* **1965**, *37*, 1351.
(87) Blaedel, W. J.; Klatt, L. N. *Anal. Chem.* **1966**, *38*, 879.
(88) Rees, N. V.; Klymenko, O. V.; Coles, B. A.; Compton, R. G. *J. Electroanal. Chem.* **2002**, *534*, 151.
(89) Novoselov, K. S.; Geim, A. K.; Morozov, S. V; Jiang, D.; Zhang, Y.; Dubonos, S. V; Grigorieva, I. V; Firsov, A. A. *Science* **2004**, *306*, 666.
(90) Novoselov, K. S.; Geim, A. K.; Morozov, S. V; Jiang, D.; Katsnelson, M. I.; Grigorieva, I. V; Dubonos, S. V; Firsov, A. A. *Nature* **2005**, *438*, 197.
(91) Peres, N. *Rev. Mod. Phys.* **2010**, *82*, 2673.
(92) Avouris, P. *Nano Lett.* **2010**, 4285.
(93) Choi, C. H.; Park, S. H.; Woo, S. I. *ACS Nano* **2012**, *6*, 7084.
(94) Zhang, Y.; Ge, J.; Wang, L.; Wang, D.; Ding, F.; Tao, X.; Chen, W. *Sci. Rep.* **2013**, *3*, 2771.
(95) Qu, L.; Liu, Y.; Baek, J.-B.; Dai, L. *ACS Nano* **2010**, *4*, 1321.
(96) Gómez-Navarro, C.; Burghard, M.; Kern, K. *Nano Lett.* **2008**, *8*, 2045.
(97) Wang, H.-X.; Wang, Q.; Zhou, K.-G.; Zhang, H.-L. *Small* **2013**, *9*, 1266.
(98) Moon, J.-S.; Gaskill, D. K. *IEEE Trans. Microw. Theory Tech.* **2011**, *59*, 2702.
(99) Avouris, P.; Lin, Y.-. M.; Xia, F.; Mueller, T.; Farmer, D. B.; Dimitrakopoulos, C.; Grill, A. In *68th Device Research Conference*; IEEE, 2010; Vol. 839, pp. 205–206.
(100) Reddy, D.; Register, L. F.; Carpenter, G. D.; Banerjee, S. K. *J. Phys. D. Appl. Phys.* **2012**, *45*, 19501.
(101) Lin, Y.-M.; Valdes-Garcia, A.; Han, S.-J.; Farmer, D. B.; Meric, I.; Sun, Y.; Wu, Y.; Dimitrakopoulos, C.; Grill, A.; Avouris, P.; Jenkins, K. A. *Science* **2011**, *332*, 1294.
(102) Bolotin, K. I.; Sikes, K. J.; Hone, J.; Stormer, H. L.; Kim, P. *Phys. Rev. Lett.* **2008**, *101*, 96802.
(103) Ohno, Y.; Maehashi, K.; Yamashiro, Y.; Matsumoto, K. *Nano Lett.* **2009**, *9*, 3318.
(104) Sohn, I.-Y.; Kim, D.-J.; Jung, J.-H.; Yoon, O. J.; Thanh, T. N.; Quang, T. T.; Lee, N.-E. *Biosens. Bioelectron.* **2013**, *45*, 70.
(105) Tan, X.; Chuang, H.; Lin, M.; Zhou, Z.; Cheng, M. M. *J. Phys. Chem. C* **2013**, *117*, 27155.
(106) Ang, P. K.; Chen, W.; Wee, A. T. S.; Loh, K. P. *J. Am. Chem. Soc.* **2008**, *130*,

14392.
(107) Sofue, Y.; Ohno, Y.; Maehashi, K.; Inoue, K.; Matsumoto, K. *Jpn. J. Appl. Phys.* **2011**, *50*, 06GE07.
(108) Maehashi, K.; Sofue, Y.; Okamoto, S.; Ohno, Y.; Inoue, K.; Matsumoto, K. *Sensors Actuators B Chem.* **2013**, *187*, 45.
(109) Fu, W.; Nef, C.; Tarasov, a; Wipf, M.; Stoop, R.; Knopfmacher, O.; Weiss, M.; Calame, M.; Schönenberger, C. *Nanoscale* **2013**, *5*, 12104.
(110) Fowler, J. D.; Allen, M. J.; Tung, V. C.; Yang, Y.; Kaner, R. B.; Weiller, B. H. *ACS Nano* **2009**, *3*, 301.
(111) Inaba, A.; Yoo, K.; Takei, Y.; Matsumoto, K.; Shimoyama, I. *Sensors Actuators B Chem.* **2014**, *195*, 15.
(112) Dan, Y.; Lu, Y.; Kybert, N. J.; Luo, Z.; Johnson, A. T. C. *Nano Lett.* **2009**, *9*, 1472.
(113) Schedin, F.; Geim, A. K.; Morozov, S. V; Hill, E. W.; Blake, P.; Katsnelson, M. I.; Novoselov, K. S. *Nat. Mater.* **2007**, *6*, 652.
(114) He, R. X.; Lin, P.; Liu, Z. K.; Zhu, H. W.; Zhao, X. Z.; Chan, H. L. W.; Yan, F. *Nano Lett.* **2012**, *12*, 1404.
(115) Newaz, A. K. M.; Markov, D. A.; Prasai, D.; Bolotin, K. I. *Nano Lett.* **2012**, *12*, 2931.
(116) He, Q.; Wu, S.; Gao, S.; Cao, X.; Yin, Z.; Li, H.; Chen, P.; Zhang, H. *ACS Nano* **2011**, *5*, 5038.
(117) Huang, Y.; Dong, X.; Shi, Y.; Li, C. M.; Li, L.-J.; Chen, P. *Nanoscale* **2010**, *2*, 1485.
(118) Stine, R.; Robinson, J. T.; Sheehan, P. E.; Tamanaha, C. R. *Adv. Mater.* **2010**, *22*, 5297.
(119) Dong, X.; Shi, Y.; Huang, W.; Chen, P.; Li, L.-J. *Adv. Mater.* **2010**, *22*, 1649.
(120) Ang, P. K.; Jaiswal, M.; Lim, C. H. Y. X.; Wang, Y.; Sankaran, J.; Li, A.; Lim, C. T.; Wohland, T.; Barbaros, O.; Loh, K. P. *ACS Nano* **2010**, *4*, 7387.
(121) Dankerl, M.; Hauf, M. V; Lippert, A.; Hess, L. H.; Birner, S.; Sharp, I. D.; Mahmood, A.; Mallet, P.; Veuillen, J.-Y.; Stutzmann, M.; Garrido, J. A. *Adv. Funct. Mater.* **2010**, *20*, 3117.
(122) Heller, I.; Chatoor, S.; Männik, J.; Zevenbergen, M. A. G.; Dekker, C.; Lemay, S. G. *J. Am. Chem. Soc.* **2010**, *132*, 17149.
(123) Kötz, R.; Carlen, M. *Electrochim. Acta* **2000**, *45*, 2483.
(124) Hess, L. H.; Hauf, M. V; Seifert, M.; Speck, F.; Seyller, T.; Stutzmann, M.; Sharp, I. D.; Garrido, J. A. *Appl. Phys. Lett.* **2011**, *99*, 33503.
(125) Ye, J.; Craciun, M. F.; Koshino, M.; Russo, S.; Inoue, S.; Yuan, H.; Shimotani, H.; Morpurgo, A. F.; Iwasa, Y. *Proc. Natl. Acad. Sci. U. S. A.* **2011**, *108*, 13002.
(126) Oostinga, J. B.; Heersche, H. B.; Liu, X.; Morpurgo, A. F.; Vandersypen, L. M. K. *Nat. Mater.* **2008**, *7*, 151.
(127) Zhang, Y.; Tang, T.-T.; Girit, C.; Hao, Z.; Martin, M. C.; Zettl, A.; Crommie, M. F.; Shen, Y. R.; Wang, F. *Nature* **2009**, *459*, 820.
(128) Yamashiro, Y.; Ohno, Y.; Maehashi, K.; Inoue, K.; Matsumoto, K. *J. Vac. Sci. Technol. B Microelectron. Nanom. Struct.* **2012**, *30*, 03D111.

(129) Chakraborty, B.; Das, A.; Sood, A. K. *Nanotechnology* **2009**, *20*, 365203.
(130) Xia, F.; Farmer, D. B.; Lin, Y.-M.; Avouris, P. *Nano Lett.* **2010**, *10*, 715.
(131) Özyilmaz, B.; Jarillo-Herrero, P.; Efetov, D.; Abanin, D.; Levitov, L.; Kim, P. *Phys. Rev. Lett.* **2007**, *99*, 166804.
(132) Abanin, D. A.; Levitov, L. S. *Science* **2007**, *317*, 641.
(133) Williams, J. R.; Dicarlo, L.; Marcus, C. M. *Science* **2007**, *317*, 638.
(134) Velasco, J.; Lee, Y.; Jing, L.; Liu, G.; Bao, W.; Lau, C. N. *Solid State Commun.* **2012**, *152*, 1301.
(135) Xia, J.; Chen, F.; Li, J.; Tao, N. *Nat. Nanotechnol.* **2009**, *4*, 505.
(136) Zhong, J.-H.; Liu, J.-Y.; Li, Q.; Li, M.-G.; Zeng, Z.-C.; Hu, S.; Wu, D.-Y.; Cai, W.; Ren, B. *Electrochim. Acta* **2013**, *110*, 754.
(137) Stoller, M. D.; Magnuson, C. W.; Zhu, Y.; Murali, S.; Suk, J. W.; Piner, R.; Ruoff, R. S. *Energy Environ. Sci.* **2011**, *4*, 4685.
(138) Zhang, S.; Lee, K. H.; Frisbie, C. D.; Lodge, T. P. *Macromolecules* **2011**, *44*, 940.
(139) Adam, S.; Hwang, E. H.; Galitski, V. M.; Das Sarma, S. *Proc. Natl. Acad. Sci. U. S. A.* **2007**, *104*, 18392.
(140) Chen, J.-H.; Jang, C.; Adam, S.; Fuhrer, M. S.; Williams, E. D.; Ishigami, M. *Nat. Phys.* **2008**, *4*, 377.
(141) Xia, J. L.; Chen, F.; Wiktor, P.; Ferry, D. K.; Tao, N. J. *Nano Lett.* **2010**, *10*, 5060.
(142) Liu, W.; Wei, J.; Sun, X.; Yu, H. *Crystals* **2013**, *3*, 257.
(143) Chen, S.; Cai, W.; Chen, D.; Ren, Y.; Li, X.; Zhu, Y.; Kang, J.; Ruoff, R. S. *New J. Phys.* **2010**, *12*, 125011.
(144) Levesque, P. L.; Sabri, S. S.; Aguirre, C. M.; Guillemette, J.; Siaj, M.; Desjardins, P.; Szkopek, T.; Martel, R. *Nano Lett.* **2011**, *11*, 132.
(145) Nistor, R. A.; Kuroda, M. A.; Maarouf, A. A.; Martyna, G. J. *Phys. Rev. B* **2012**, *86*, 41409.
(146) Han, D.; West, D.; Li, X.-B.; Xie, S.-Y.; Sun, H.-B.; Zhang, S. B. *Phys. Rev. B* **2010**, *82*, 155132.
(147) Kang, Y.-J.; Kang, J.; Chang, K. *Phys. Rev. B* **2008**, *78*, 115404.
(148) Suk, J. W.; Lee, W. H.; Lee, J.; Chou, H.; Piner, R. D.; Hao, Y.; Akinwande, D.; Ruoff, R. S. *Nano Lett.* **2013**, *13*, 1462.
(149) Chen, F.; Xia, J.; Ferry, D. K.; Tao, N. *Nano Lett.* **2009**, *9*, 2571.
(150) Chen, F.; Xia, J.; Tao, N. *Nano Lett.* **2009**, *9*, 1621.
(151) Mišković, Z. L.; Sharma, P.; Goodman, F. O. *Phys. Rev. B* **2012**, *86*, 115437.
(152) Kim, S.; Nah, J.; Jo, I.; Shahrjerdi, D.; Colombo, L.; Yao, Z.; Tutuc, E.; Banerjee, S. K. *Appl. Phys. Lett.* **2009**, *94*, 62107.
(153) Andrei, E. Y.; Li, G.; Du, X. *Rep. Prog. Phys.* **2012**, *75*, 56501.
(154) Novikov, D. *Phys. Rev. B* **2007**, *76*, 245435.
(155) Novikov, D. S. *Appl. Phys. Lett.* **2007**, *91*, 102102.
(156) Huard, B.; Stander, N.; Sulpizio, J.; Goldhaber-Gordon, D. *Phys. Rev. B* **2008**, *78*, 121402.
(157) Liu, W. J.; Yu, H. Y.; Xu, S. H.; Zhang, Q.; Zou, X.; Wang, J. L.; Pey, K. L.; Wei, J.; Zhu, H. L.; Li, M. F. *IEEE Electron Device Lett.* **2011**, *32*, 128.
(158) Hannes, W.-R.; Jonson, M.; Titov, M. *Phys. Rev. B* **2011**, *84*, 45414.

(159) Barraza-Lopez, S.; Vanević, M.; Kindermann, M.; Chou, M. Y. *Phys. Rev. Lett.* **2010**, *104*, 76807.
(160) Chen, F.; Xia, J.; Tao, N. *Nano Lett.* **2009**, *9*, 1621.
(161) Jena, D.; Konar, A. *Phys. Rev. Lett.* **2007**, *98*, 136805.
(162) Newaz, a K. M.; Puzyrev, Y. S.; Wang, B.; Pantelides, S. T.; Bolotin, K. I. *Nat. Commun.* **2012**, *3*, 734.
(163) Wrighton, M. S. *Acc. Chem. Res.* **1979**, *12*, 303.
(164) Bard, A. J. *Science* **1980**, *207*, 139.
(165) Walter, M. G.; Warren, E. L.; McKone, J. R.; Boettcher, S. W.; Mi, Q.; Santori, E. A.; Lewis, N. S. *Chem. Rev.* **2010**, *110*, 6446.
(166) Hagfeldt, A.; Boschloo, G.; Sun, L.; Kloo, L.; Pettersson, H. *Chem. Rev.* **2010**, *110*, 6595.
(167) Tu, W.; Zhou, Y.; Zou, Z. *Adv. Mater.* **2014**, *26*, 4607.
(168) Eggleston, C. M.; Stern, J. R.; Strellis, T. M.; Parkinson, B. A. *Am. Mineral.* **2012**, *97*, 1804.
(169) Novoselov, K. S.; Jiang, D.; Schedin, F.; Booth, T. J.; Khotkevich, V. V; Morozov, S. V; Geim, A. K. *Proc. Natl. Acad. Sci. U. S. A.* **2005**, *102*, 10451.
(170) Lee, Y. H.; Zhang, X. Q.; Zhang, W.; Chang, M. T.; Lin, C. Te; Chang, K. Di; Yu, Y. C.; Wang, J. T. W.; Chang, C. S.; Li, L. J.; Lin, T. W. *Adv. Mater.* **2012**, *24*, 2320.
(171) Tan, C.; Rodríguez-López, J.; Parks, J. J.; Ritzert, N. L.; Ralph, D. C.; Abruña, H. D. *ACS Nano* **2012**, *6*, 3070.
(172) Ambrosi, A.; Chua, C. K.; Bonanni, A.; Pumera, M. *Chem. Rev.* **2014**, *114*, 7150.
(173) Eady, S. C.; Peczonczyk, S. L.; Maldonado, S.; Lehnert, N. *Chem. Commun.* **2014**, *50*, 8065.
(174) Voiry, D.; Yang, J.; Chhowalla, M. *Adv. Mater.* **2016**, n/a.
(175) Hou, Y.; Laursen, A. B.; Zhang, J.; Zhang, G.; Zhu, Y.; Wang, X.; Dahl, S.; Chorkendorff, I. *Angew. Chemie Int. Ed.* **2013**, *52*, 3621.
(176) Li, Y.; Wang, H.; Xie, L.; Liang, Y.; Hong, G.; Dai, H. *J. Am. Chem. Soc.* **2011**, *133*, 7296.
(177) Jaramillo, T. F.; Jorgensen, K. P.; Bonde, J.; Nielsen, J. H.; Horch, S.; Chorkendorff, I. *Science* **2007**, *317*, 100.
(178) Eisenberg, D. *ChemElectroChem* **2015**, *2*, 1259.
(179) Kim, C.; Frisbie, C. D. *J. Phys. Chem. C* **2014**, *118*, 21160.
(180) Neamen, D. A. In *Semiconductor Physics and Devices: Basic Principles*; McGraw-Hill, 2012; pp. 371–490.
(181) Hamann, T. W.; Gstrein, F.; Brunschwig, B. S.; Lewis, N. S. *J. Am. Chem. Soc.* **2005**, *127*, 7815.
(182) Hamann, T. W.; Gstrein, F.; Brunschwig, B. S.; Lewis, N. S. *J. Am. Chem. Soc.* **2005**, *127*, 13949.
(183) Lewis, N. S. *J. Phys. Chem. B* **1998**, *102*, 4843.
(184) Bard, A. J. *J. Am. Chem. Soc.* **2010**, *132*, 7559.
(185) Simpson, B. H.; Rodríguez-López, J. *J. Am. Chem. Soc.* **2015**, *137*, 14865.
(186) Hoarfrost, M. L.; He, Y.; Lodge, T. P. *Macromolecules* **2013**, *46*, 9464.

(187) Neamen, D. A. In *Semiconductor Physics and Devices: Basic Principles*; McGraw-Hill, 2012; pp. 58–105.
(188) Young, D. L.; Coutts, T. J.; Kaydanov, V. I.; Gilmore, A. S.; Mulligan, W. P. *J. Vac. Sci. Technol. A Vacuum, Surfaces, Film.* **2000**, *18*, 2978.
(189) Radisavljevic, B.; Whitwick, M. B.; Kis, A. *ACS Nano* **2011**, *5*, 9934.
(190) Chuang, H.; Tan, X.; Ghimire, N. J.; Perera, M. M.; Chamlagain, B.; Cheng, M. M.; Yan, J.; Mandrus, D.; Tománek, D.; Zhou, Z. *Nano Lett.* **2014**, *14*, 3594.
(191) Tang, K. C.; Liao, E.; Ong, W. L.; Wong, J. D. S.; Agarwal, A.; Nagarajan, R.; Yobas, L. *J. Phys. Conf. Ser.* **2006**, *34*, 155.
(192) Moia, D.; Vaissier, V.; López-Duarte, I.; Torres, T.; Nazeeruddin, M. K.; O'Regan, B. C.; Nelson, J.; Barnes, P. R. F. *Chem. Sci.* **2014**, *5*, 281.
(193) Rees, N. V.; Clegg, A. D.; Klymenko, O. V.; Coles, B. A.; Compton, R. G. *J. Phys. Chem. B* **2004**, *108*, 13047.
(194) Rüssel, C.; Janicke, W. *J. Electroanal. Chem.* **1986**, *199*, 139.
(195) Trasatti, S. *J. Electroanal. Chem. Interfacial Electrochem.* **1972**, *39*, 163.
(196) Parsons, R. *Trans. Faraday Soc.* **1958**, *54*, 1053.
(197) Conway, B. E.; Bockris, J. O. *J. Chem. Phys.* **1957**, *26*, 532.
(198) Jaramillo, T. F.; Jorgensen, K. P.; Bonde, J.; Nielsen, J. H.; Horch, S.; Chorkendorff, I. *Science* **2007**, *317*, 100.
(199) Dau, H.; Limberg, C.; Reier, T.; Risch, M.; Roggan, S.; Strasser, P. *ChemCatChem* **2010**, *2*, 724.
(200) Jiao, Y.; Zheng, Y.; Jaroniec, M.; Qiao, S. Z. *Chem. Soc. Rev.* **2015**, *44*, 2060.
(201) Hammer, B.; Norskov, J. K. Why gold is the noblest of all the metals. *Nature*, 1995, *376*, 238–240.
(202) Anderson, A. B. *Phys. Chem. Chem. Phys.* **2012**, *14*, 1330.
(203) Nørskov, J. K.; Rossmeisl, J.; Logadottir, A.; Lindqvist, L.; Kitchin, J. R.; Bligaard, T.; Jónsson, H. *J. Phys. Chem. B* **2004**, *108*, 17886.
(204) Santos, E.; Quaino, P.; Schmickler, W. *Phys. Chem. Chem. Phys.* **2012**, *14*, 11224.
(205) Filhol, J. S.; Neurock, M. *Angew. Chemie - Int. Ed.* **2006**, *45*, 403.
(206) Taylor, C. D.; Wasileski, S. A.; Filhol, J. S.; Neurock, M. *Phys. Rev. B - Condens. Matter Mater. Phys.* **2006**, *73*, 1.
(207) Rossmeisl, J.; Skúlason, E.; Björketun, M. E.; Tripkovic, V.; Nørskov, J. K. *Chem. Phys. Lett.* **2008**, *466*, 68.
(208) Skulason, E.; Tripkovic, V.; Bjorketun, M. E.; Gudmundsdottir, S.; Karlberg, G.; Rossmeisl, J.; Bligaard, T.; Jonsson, H.; Norskov, J. K. *J. Phys. Chem. C* **2010**, *114*, 18182.
(209) Skúlason, E.; Karlberg, G. S.; Rossmeisl, J.; Bligaard, T.; Greeley, J.; Jónsson, H.; Nørskov, J. K. *Phys. Chem. Chem. Phys.* **2007**, *9*, 3241.
(210) Jinnouchi, R.; Anderson, A. B. *J. Phys. Chem. C* **2008**, *112*, 8747.
(211) Otani, M.; Hamada, I.; Sugino, O.; Morikawa, Y.; Okamoto, Y.; Ikeshoji, T. *J. Phys. Soc. Japan* **2008**, *77*, 1.
(212) Robertson, J. *Eur. Phys. J. Appl. Phys.* **2004**, *28*, 265.
(213) Pal, B. N.; Dhar, B. M.; See, K. C.; Katz, H. E. *Nat. Mater.* **2009**, *8*, 898.
(214) Cai, X.; Frisbie, C. D.; Leighton, C. *Appl. Phys. Lett.* **2006**, *89*, 242915.

(215) Yoldas, B. E. *J. Mater. Sci.* **1975**, *10*, 1856.
(216) Zhang, B.; Liu, Y.; Agarwal, S.; Yeh, M.-L.; Katz, H. E. *ACS Appl. Mater. Interfaces* **2011**, *3*, 4254.
(217) Sire, C.; Blonkowski, S.; Gordon, M. J.; Baron, T. *Appl. Phys. Lett.* **2007**, *91*, 242905.
(218) Krupski, K.; Moors, M.; Jóźwik, P.; Kobiela, T.; Krupski, A. *Materials (Basel).* **2015**, *8*, 2935.
(219) Tan, C.; Cao, X.; Wu, X.-J.; He, Q.; Yang, J.; Zhang, X.; Chen, J.; Zhao, W.; Han, S.; Nam, G.-H.; Sindoro, M.; Zhang, H. *Chem. Rev.* **2017**, *117*, 6225.
(220) Voiry, D.; Mohite, A.; Chhowalla, M. *Chem. Soc. Rev.* **2015**, *44*, 2702.
(221) Hinnemann, B.; Moses, P. G.; Bonde, J.; Jørgensen, K. P.; Nielsen, J. H.; Horch, S.; Chorkendorff, I.; Nørskov, J. K. *J. Am. Chem. Soc.* **2005**, *127*, 5308.
(222) M, C. *Nano Lett.* **2012**, *12*, 526.
(223) Wang, H.; Lu, Z.; Xu, S.; Kong, D.; Cha, J. J.; Zheng, G.; Hsu, P.-C.; Yan, K.; Bradshaw, D.; Prinz, F. B.; Cui, Y. *Proc. Natl. Acad. Sci.* **2013**, *110*, 19701.
(224) Voiry, D.; Goswami, A.; Kappera, R.; Silva, C. de C. C. e; Kaplan, D.; Fujita, T.; Chen, M.; Asefa, T.; Chhowalla, M. *Nat. Chem.* **2014**, *7*, 45.
(225) Lukowski, M. A.; Daniel, A. S.; Meng, F.; Forticaux, A.; Li, L.; Jin, S. *J. Am. Chem. Soc.* **2013**, *135*, 10274.
(226) Voiry, D.; Salehi, M.; Silva, R.; Fujita, T.; Chen, M.; Asefa, T.; Shenoy, V. B.; Eda, G.; Chhowalla, M. *Nano Lett.* **2013**, *13*, 6222.
(227) Tang, Q.; Jiang, D. *ACS Catal.* **2016**, *6*, 4953.
(228) Lukowski, M. A.; Daniel, A. S.; English, C. R.; Meng, F.; Forticaux, A.; Hamers, R. J.; Jin, S. *Energy Environ. Sci.* **2014**, *7*, 2608.
(229) Voiry, D.; Yamaguchi, H.; Li, J.; Silva, R.; Alves, D. C. B.; Fujita, T.; Chen, M.; Asefa, T.; Shenoy, V. B.; Eda, G.; Chhowalla, M. *Nat. Mater.* **2013**, *12*, 850.
(230) Blanford, C. F.; Foster, C. E.; Heath, R. S.; Armstrong, F. A. *Faraday Discuss.* **2009**, *140*, 319.
(231) Merki, D.; Vrubel, H.; Rovelli, L.; Fierro, S.; Hu, X. *Chem. Sci.* **2012**, *3*, 2515.
(232) Kibsgaard, J.; Tuxen, A.; Knudsen, K. G.; Brorson, M.; Topsøe, H.; Lægsgaard, E.; Lauritsen, J. V.; Besenbacher, F. *J. Catal.* **2010**, *272*, 195.
(233) Benck, J. D.; Hellstern, T. R.; Kibsgaard, J.; Chakthranont, P.; Jaramillo, T. F. *ACS Catal.* **2014**, *4*, 3957.
(234) Chen, W.; Santos, E. J. G.; Zhu, W.; Kaxiras, E.; Zhang, Z. *Nano Lett.* **2013**, *13*, 509.
(235) Tsai, C.; Abild-Pedersen, F.; Nørskov, J. K. *Nano Lett.* **2014**, *14*, 1381.
(236) Liao, T.; Sun, Z.; Sun, C.; Dou, S. X.; Searles, D. J. *Sci. Rep.* **2015**, *4*, 6256.
(237) Shi, Y.; Zhou, W.; Lu, A.-Y.; Fang, W.; Lee, Y.-H.; Hsu, A. L.; Kim, S. M.; Kim, K. K.; Yang, H. Y.; Li, L.-J.; Idrobo, J.-C.; Kong, J. *Nano Lett.* **2012**, *12*, 2784.
(238) Ago, H.; Endo, H.; Solís-Fernández, P.; Takizawa, R.; Ohta, Y.; Fujita, Y.; Yamamoto, K.; Tsuji, M. *ACS Appl. Mater. Interfaces* **2015**, *7*, 5265.
(239) Seh, Z. W.; Kibsgaard, J.; Dickens, C. F.; Chorkendorff, I.; Nørskov, J. K.; Jaramillo, T. F. *Science* **2017**, *355*, eaad4998.
(240) Viswanathan, V.; Hansen, H. A.; Rossmeisl, J.; Nørskov, J. K. *ACS Catal.* **2012**, *2*,

1654.
(241) Vojvodic, A.; Nørskov, J. K. *Natl. Sci. Rev.* **2015**, *2*, 140.
(242) Kong, X.-K.; Chen, C.-L.; Chen, Q.-W. *Chem. Soc. Rev.* **2014**, *43*, 2841.
(243) Wang, X.; Sun, G.; Routh, P.; Kim, D.-H.; Huang, W.; Chen, P. *Chem. Soc. Rev.* **2014**, *43*, 7067.
(244) Wang, D.-W.; Su, D. *Energy Environ. Sci.* **2014**, *7*, 576.
(245) MATTER, P.; ZHANG, L.; OZKAN, U. *J. Catal.* **2006**, *239*, 83.
(246) Dorjgotov, A.; Ok, J.; Jeon, Y.; Yoon, S.-H.; Shul, Y. G. *J. Appl. Electrochem.* **2013**, *43*, 387.
(247) Huang, H.; Feng, X.; Du, C.; Song, W. *Chem. Commun.* **2015**, *51*, 7903.
(248) Huang, H.; Feng, X.; Du, C.; Wu, S.; Song, W. *J. Mater. Chem. A* **2015**, *3*, 16050.
(249) Danilovic, N.; Subbaraman, R.; Chang, K.-C.; Chang, S. H.; Kang, Y. J.; Snyder, J.; Paulikas, A. P.; Strmcnik, D.; Kim, Y.-T.; Myers, D.; Stamenkovic, V. R.; Markovic, N. M. *J. Phys. Chem. Lett.* **2014**, *5*, 2474.
(250) Kötz, R.; Stucki, S.; Scherson, D.; Kolb, D. M. *J. Electroanal. Chem. Interfacial Electrochem.* **1984**, *172*, 211.
(251) Song, F.; Hu, X. *Nat. Commun.* **2014**, *5*, 1.
(252) Song, F.; Hu, X. *J. Am. Chem. Soc.* **2014**, *136*, 16481.
(253) Tang, D.; Han, Y.; Ji, W.; Qiao, S.; Zhou, X.; Liu, R.; Han, X.; Huang, H.; Liu, Y.; Kang, Z. *Dalt. Trans.* **2014**, *43*, 15119.
(254) Liang, L.; Cheng, H.; Lei, F.; Han, J.; Gao, S.; Wang, C.; Sun, Y.; Qamar, S.; Wei, S.; Xie, Y. *Angew. Chemie Int. Ed.* **2015**, *54*, 12004.
(255) Liu, Y.; Cheng, H.; Lyu, M.; Fan, S.; Liu, Q.; Zhang, W.; Zhi, Y.; Wang, C.; Xiao, C.; Wei, S.; Ye, B.; Xie, Y. *J. Am. Chem. Soc.* **2014**, *136*, 15670.
(256) Liu, Y.; Xiao, C.; Lyu, M.; Lin, Y.; Cai, W.; Huang, P.; Tong, W.; Zou, Y.; Xie, Y. *Angew. Chemie Int. Ed.* **2015**, *54*, 11231.
(257) Xie, J.; Wang, R.; Bao, J.; Zhang, X.; Zhang, H.; Li, S.; Xie, Y. *Inorg. Chem. Front.* **2014**, *1*, 751.
(258) Duan, H.; Yan, N.; Yu, R.; Chang, C.-R.; Zhou, G.; Hu, H.-S.; Rong, H.; Niu, Z.; Mao, J.; Asakura, H.; Tanaka, T.; Dyson, P. J.; Li, J.; Li, Y. *Nat. Commun.* **2014**, *5*, 1.
(259) Huang, X.; Tang, S.; Mu, X.; Dai, Y.; Chen, G.; Zhou, Z.; Ruan, F.; Yang, Z.; Zheng, N. *Nat. Nanotechnol.* **2011**, *6*, 28.
(260) Jang, K.; Kim, H. J.; Son, S. U. *Chem. Mater.* **2010**, *22*, 1273.
(261) Zhao, L.; Xu, C.; Su, H.; Liang, J.; Lin, S.; Gu, L.; Wang, X.; Chen, M.; Zheng, N. *Adv. Sci.* **2015**, *2*, 1500100.
(262) Gao, S.; Lin, Y.; Jiao, X.; Sun, Y.; Luo, Q.; Zhang, W.; Li, D.; Yang, J.; Xie, Y. *Nature* **2016**, *529*, 68.
(263) Asadi, M.; Kumar, B.; Behranginia, A.; Rosen, B. A.; Baskin, A.; Repnin, N.; Pisasale, D.; Phillips, P.; Zhu, W.; Haasch, R.; Klie, R. F.; Král, P.; Abiade, J.; Salehi-Khojin, A. *Nat. Commun.* **2014**, *5*, 1.